DTU

Detection and characterisation of localised structural nonlinearity

Master Thesis

$$(EIv'')'' = q - \rho A\ddot{v}$$

Δ $\int_a^b$ ε θ $\sqrt{17}$ Ω $\int$ ∞ $+$ $\{2.718$ χ^2 $\sum$

Paw Møller
November 2017

Preface

Paw Møller, s082705
Masters Thesis 28.5 ECTS
October, 2017
Supervisors:
Jon Juel Thomsen; Associate professor, dr.tech.
Marie Brøns; Ph.d Student.
DTU MEK, section for Solid Mechanics(FAM)

Tak til Jon og Marie for jeres tålmodighed. Især Marie har haft flere problemer med mig, end man normalt kan forlange af en vejleder.

Contents

Notation

x, X	Scalar variable or function (italics)
$\mathbf{x}$	Vector (lowercase, bold)
x_i	Vector element
$\mathbf{X}$	Matrix (uppercase, bold)
$X_{i,j}$	Matrix element
$\mathbf{x}^T, \mathbf{X}^T$	Vector or matrix transpose
$\mathbf{x}^*$	Complex conjugate
$\mathbf{X}_\odot = \mathbf{X} \odot I$	Bialternate product of matrix
$\mathbf{X}^\perp$	Orthogonal complement of the subspace of $\mathbf{X}$
$\hat{\mathbf{X}}$	Estimate of $\mathbf{X}$
$\mathbf{X}_\omega$	Partial derivative, $\frac{\partial \mathbf{x}}{\partial \omega}$
$\lvert x \rvert$	Absolute value
$\det \mathbf{x}$	Determinant of $\mathbf{x}$
$\lVert \mathbf{x} \rVert_2$	Euclidean norm of x (ie. the length)
$\mathbf{X}^+$	Moore-Penrose pseudoinverse of $\mathbf{X}$
$\dot{x}, \ddot{x}$	Time derivatives
$x^{[i]}_{[i]}$	i'th iterate
$\mathcal{O}$	Order of magnitude
∇, ∇^2	Gradient/Laplacian operator
$\equiv$	Assigning equality
$\operatorname{sgn}(x)$	Sign of x (sign function)
$j = 1, n$	$j = 1, 2, ..., n$

Abbreviation

EOM	Equation of motion
DOF	Degree of freedom
MDOF	Multiple degree of freedom
SDOF	Single degree of freedom
FEM	Finite element method
FEP	Frequency-energy plot
FNSI	Frequency-domain nonlinear subspace identification
LNM	Linear normal mode
MIMO	multi-input, multi output
NNM	Nonlinear normal mode
NFRC	nonlinear frequency response curve
PSD	Power spectral densities
RFS	Restoring Force Surface. Same as Acceleration Surface Method.
FRF	Frequency response function
SNR	signal-to-noise ratio
FT	Fourier transform.
STFT	Short Time Fourier transform.
MW	Morlet wavelet. (a special case of STFT with varying window)
HB	Harmonic balance
NR	Newton-Raphson (iterations)
AFT	alternating frequency-time domain
BP	Bifurcation point
NS	Neimark-Sacker bifurcation
PD	Period doubling bifurcation
QP	Quasiperiodic oscillations

Chapter 1

Introduction

This project demonstrates methods for estimating linear parameters obtained from nonlinear vibration signals. The project also demonstrates methods predicting the behaviour of identified nonlinear systems. The methods are implemented in a vibration library.

1.1 Why nonlinear modeling

For nonlinear systems, the superposition and thus invariance of modes and uniqueness of solutions (e.g. the forced steady state response is dependent on the initial transient behavior) does no longer hold, and many of the techniques from linear analysis cannot be used.

Linear system is an exception. If excited hard enough, all system displays some nonlinear behavior. But often the nonlinearity stems from joints (damping), contact (stiffness) or geometrical nonlinearities, which is why most of the literature today treats localized nonlinearity, assuming the location of the nonlinearity is known. Another reason for dealing with localized nonlinearities, is that no robust method for localization exists. In his thesis Kragh [21] test different methods for localizing nonlinearity and concludes that *it was not possible to obtain consistent localization of the nonlinearities* even for simple structures.

With the introduction of ever lighter structures, exotic materials, high speed machinery, etc., nonlinear tools are needed to fully understand the dynamics. Also to determine if nonlinear analysis is indeed needed, since this kind of analysis requires substantial more effort than linear analysis would do.

For a general introduction to nonlinear dynamics, the textbook by Juel Thomsen [17] can be used.

1.2 Nonlinear system identification?

Kerschen et al. [18] proposed to regard the identification of nonlinear structural models as a progression through three steps: *detection*, *characterization* and *estimation*, as outlined in figure 1.2.1

The first book on the topic was [42], and even though many new methods has been introduced since then, it still gives a good introduction to the subject as well as a overview of the common types of nonlinearities.

A comprehensive review of the development in nonlinear system identification was given by [18] and just recently by [32]. For comparison of the many techniques in use, the reader is refereed to these reviews. In this thesis, alternative techniques will not be mentioned.

---

1. Detection: *I*s there?
   Ascertain if nonlinearity exist in the structural behavior, e.g. yes or no.

2. Characterisation: *W*here, what and how?

   - Localize the nonlinearity, e.g. at the joint

   - Determine the type of nonlinearity e.g. Coulomb friction
     More general: is it stiffness or damping nonlinearity or both. In the case of stiffness: is it hardening or softening

   - Select the functional form of the nonlinearity, e.g. $f(x, \dot{x}) = c\,\mathrm{sgn}(\dot{y})$

3. Parameter estimation: *H*ow much?
   Calculate the coefficients of the nonlinearity model, e.g. $c = 5.47$.
   (Ideally the uncertainty should be quantified, e.g. in a probabilistic sense, $c \sim N(5.47, 1)$. But that is a very difficult task and not within the scope of this thesis)

Figure 1.2.1: Identification process for nonlinear structural models

1.2.1   Detection

Of the three steps, detection is the easiest. During test, the structure should be excited by a sine-sweep and a mere visual inspection of the time series will show if nonlinearity is present. Signs includes skewness of the envelope, discontinuity, jumps and lack of invariance with increasing force level. The excitation level needs to be at an amplitude where the nonlinearity is activated.

Random excitation is in general not useful, as the randomness of the amplitude and phase of the excitation creates *linearized* frequency response functions (FRFs). At least multiple test with different rms levels are required, and still then it might be difficult to excite the nonlinearities, since the total power of the input spectrum is spread over the band-limited frequency range used.

The use of impact excitation, as often used in linear analysis, suffers from the same problems as random excitation. That is, the input is a broad spectrum and the energy associated with each frequency is low.

Formal methods for detection includes

- Homogeneity check
  Comparing the response of two sweeps with different forcing and calculating

the cross correlation. It is a test of superposition, by testing if the two FRFs normalized with forcing overlay as they will for linear systems.

- (ordinary) Coherence function
  The coherence function compares power spectral densities (PSDs) and are required to be unity for all accessible frequencies for the system to be linear *and* free of noise. The advantage is that only one test is needed, but the method does not distinguish between cases of noise and nonlinearity. Instead it is recommend do use:

- Hilbert transforms
  This method detects nonlinearity by doing a Hilbert transform of the FRF, which is invariant for a linear FRF. A Hilbert transform also only requires one data set and is more sensitive to nonlinearity than the coherence function, but still reasonable easy to implement. Kragh [21] shows that the homogeneity check is superior to the Hilbert transforms, having higher sensitivity to nonlinearity.

For all of these methods it is a requirement that the nonlinearities are activated, e.g. the forcing level end frequency interval should be chosen adequately. Also, the methods are better at detecting nonlinear stiffness than nonlinear damping. This is due to the fact that the resonance peak is not shifted as with the stiffness nonlinearity case. Since the FRF is not shifted but only lowered, the cross correlation coefficient will not decrease as much as in the stiffness nonlinearity case. In general damping nonlinearity is difficult to identify and will only be touched briefly in this thesis.

1.2.2 Characterisation

The second step is the most important and also the most difficult, when localization is not considered. This step seeks to identify the aspects of the motion that drives the nonlinearity, e.g. displacement or velocity and a representative functional form to represent the nonlinearity.

The most used technique is the restoring force surface(RFS). The RFS provides information of restoring force in the excited range. To visualize the functional of the restoring force and the dissipative force, two slices in the RFS is made: at zero displacement and zero velocity. The functional form is then found by simple inspection of the slices or fitting polynomials and perform goodness of fit.

Another characterisation method, the Morlet wavelet transform, is used to visualise how the frequency content changes with amplitude, a consequence of the energy-frequency dependency for nonlinear vibrations. The visualised instantaneous spectrum can both be used for detection of nonlinearity and help estimating the type of nonlinearity,

1.2.3 Estimation

The RFS method can be used for estimation as well, fitting the functional form to the surface. But in order to scale the RFS correct, an estimate of the mass (or inertia) is needed or the full EOM has to be assembled. This is often difficult for MDOF systems.

A newer method, introduced by [29], is the frequency-domain nonlinear subspace identification(FNSI). This method works on time series exclusive and is able to estimate nonlinear parameters and the underlying frequency response function(FRF).

1.3 Beyond nonlinear system identification

When the identification steps is completed, a structural model can be build from a FEM of the underlying linear structure with the identified nonlinearities incorporated. It shall be thought of as (larger) chunks of linear sections connected through nonlinear elements. To reduce the computational time, the linear model is often reduced using the Craig-Bampton reduction technique [7].

If the predictions from the nonlinear FEM can be verified by the experimental results, the numerical model can be used to *get further understanding of the nonlinear dynamics*. The latter is the whole goal of the identification, as it allows for uncovering new nonlinear regimes of motion and to make design modifications. The concept of using numerical experiments to assist with the design is referred to as *virtual prototyping*.

1.3.1 Internal resonance

Nonlinear resonances are investigated using an extension of linear normal modes (LNMs) to nonlinear theory, the nonlinear normal modes (NNMs) described in section 3.1. Where a LNM is interpreted as the deformation along the axis of the vibrating structure or the rotation, a NNM does not have such a clear interpretation. An NNM is said to be a periodic oscillation of the underlaying undamped and unforced nonlinear system and depends on the frequency and energy of the system. NNMs are described in depth in [19, 35].

1.3.2 Bifurcation

Using the HB method, nonlinear forced response curves(NFRCs) for a periodic excitation are calculated. The transition from a stable periodic solution to an unstable solution occurs through bifurcations. The type of bifurcation is used to qualify the type of unstable solution emerging. The HB method followed here were introduced in [8].

1.4 Thesis outline

To summarise, chapter 2 introduces the wavelet transform and RFS for characterisation and FNSI for estimation; the methods used for identification as depicted in fig. 1.2.1. All methods are working exclusively on time series.

Chapter 3 introduces numerical methods working on a finite element discretization of the identified system. These methods are used to get qualitative information on the nonlinear behavior.

Chapter 4 introduce the python library implementing the methods and gives a brief example on how to use it. All examples from this thesis can be found online together with the library.

In chapter 5 the methods from chapter 2 and 3 are demonstrated on two nonlinear systems.

All methods are exemplified on the nonlinear two degree of freedom system(2DOF) (1.5.1) presented next.

1.5 Numerical example

To illustrate the methods presented, the 2-DOF system shown in figure 1.5.1 is used throughout the thesis. It will be referred to as the coupled duffing system, with parameters listed in table 1.5.1 and natural frequencies and damping ratio for the two modes listed in table 1.5.2. The equations of motion are

$$
\begin{aligned}
m_1\ddot{x}_1 + c\dot{x}_1 + kx_1 + \mu x_1^3 + d(x_1 - x_2) &= p \\
m_2\ddot{x}_2 + c\dot{x}_2 + kx_2 + \mu x_2^3 + d(x_2 - x_1) &= 0
\end{aligned}
\tag{1.5.1}
$$

where x_1, x_2, p all depends on time.

An example on how a real continous beam with different nonlinear boundary conditions is transformed into a coupled MDOF nonlinear duffing oscillator is given in Hermansen [16]

m_1 (kg)	m_2 (kg)	k (N/m)	d (N/m)	c (N/ms)	μ (N/m^3)
1	1	1	5	0.1	1

Table 1.5.1: Linear and nonlinear parameters for the coupled Duffing system

Mode	Frequency (rad/s)	Damping ratio (%)
1	1.00	5.00
2	3.32	1.51

Table 1.5.2: Linear natural frequencies and damping ratios for the coupled Duffing system
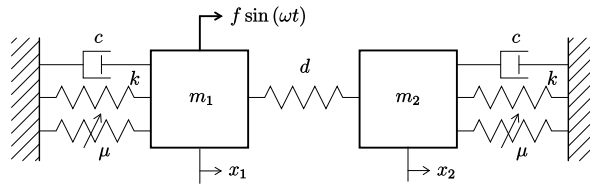
Figure 1.5.1: Schematic representation of the coupled duffing system

For generating data for characterisation with WT and RFS, the system is simulated using a logarithmic sine sweep with a sweep rate of 1 oct/min.

For identification, a single band-limited (0-15 rad/s) normally distributed random signal with 5000 points repeated 9 times and a root mean square(rms) value of 3N is used. This signal is called a multisine. The frequencies are chosen to include third harmonics of the highest natural frequency.

Formally a multisine is defined as a *sum of sine waves with related frequencies*[34]:

$$u(t) = N^{1/2} \sum_{-N/2+1}^{N/2-1} U_k e^{j\left(2\pi k \frac{f_s}{N} t + \phi_k\right)} \tag{1.5.2}$$

where N is the number of time sample and f_s the sampling frequency. The phases ϕ_k are drawn from a uniform distribution on $[0, 2\pi[$ and the amplitudes U_k are controlled to create the desired spectrum(normally flat in the desired frequency spectrum). The signal u is asymptotically normally distributed as N tends to infinity.

Chapter 2

Methods for dection, characterization and estimation

This chapter deals with the identification process as depicted in figure 1.2.1, and repeated below, treating localised nonlinearities.

---

1. Detection: *I*s there?
   Ascertain if nonlinearity exist in the structural behavior, e.g. yes or no.

2. Characterisation: *W*here, what and how?

   - Localize the nonlinearity, e.g. at the joint

   - Determine the type of nonlinearity e.g. Coulomb friction
     More general: is it stiffness or damping nonlinearity or both. In the case of stiffness: is it hardening or softening

   - Select the functional form of the nonlinearity, e.g. $f(x, \dot{x}) = c\,\text{sgn}(\dot{y})$

3. Parameter estimation: *H*ow much?
   Calculate the coefficients of the nonlinearity model, e.g. $c = 5.47$.
   (Ideally the uncertainty should be quantified, e.g. in a probabilistic sense, $c \sim N(5.47, 1)$. But that is a very difficult task and not within the scope of this thesis)

Figure 2.0.1: Identification process for nonlinear structural models

Methods for detection are only referred, as detection is usual deemed easy within the framework of localised nonlinearities [32]. Characterisation is done by wavelet transform and restoring force surface, while estimation is done by FNSI.

2.1 Detection

This section is only included for completeness, as the signs are well established. More information can be found in [42].

During test, the structure should be excited by a sine-sweep and a mere visual inspection of the time series will show if nonlinearity is present. Signs includes skewness of the envelope, discontinuity, jumps and lack of invariance with increasing force level. The excitation level needs to be at an amplitude where the nonlinearity is activated.

Random excitation is in general not useful, as the randomness of the amplitude and phase of the excitation creates "linearised" FRFs. At least multiple test with different forcing levels are required, and still then it might be difficult to excite the nonlinearities, since the total power of the input spectrum is spread over the band-limited frequency range used.

The use of impact excitation, as often used in linear analysis, suffers from the same problems as random excitation. That is, the input is a broad spectrum and the energy associated with each frequency is low.

Formal methods for detection includes

- *Homogeneity check*
  Comparing the response of two sweeps with different forcing and calculating the cross correlation. It is a test of superposition, by testing if the two FRFs normalized with forcing overlay as they will for linear systems.

- *(ordinary) Coherence function*
  The coherence function compares power spectral densities (PSDs) and are required to be unity for all accessible frequencies for the system to be linear *and* free of noise. The advantage is that only one test is needed, but the method does not distinguish between cases of noise and nonlinearity. Instead it is recommend do use:

- *Hilbert transforms*
  This method detects nonlinearity by doing a Hilbert transform of the FRF, which is invariant for a linear FRF. A Hilbert transform also only requires one data set and is more sensitive to nonlinearity than the coherence function, but still reasonable easy to implement. Kragh [21] shows that the homogeneity check is superior to the Hilbert transforms, having higher sensitivity to nonlinearity.

- *Wavelet transforms*
  Maps a time-history to a time-frequency representation. Fourier transform cannot be used, since it is a one-to-one transformation from time to frequency domain. This method, as it is also used for characterisation, is included in the report and described in section 2.2.

For all of these methods it is a requirement that the nonlinearities are activated, eg. the forcing level end frequency interval should be chosen adequately. Also, the methods are better at detecting nonlinear stiffness than nonlinear damping. This is due to the fact that the resonance peak is not shifted as with the stiffness nonlinearity case. Since the FRF is not shifted but only lowered, the cross correlation coefficient

will not decrease as much as in the stiffness nonlinearity case. In general damping nonlinearity is difficult to identify.

2.2 Wavelet transform

Due to the frequency-energy dependence of nonlinear vibrations, giving time varying frequencies for sine sweeps, the Fourier transform(FT) does not give useful results.

$$X(\omega) = \int_{-\infty}^{\infty} x(t)e^{-i\omega t}\,\mathrm{d}t \tag{2.2.1}$$

To allow for a varying frequency the Short Time Fourier transform(STFT) can be used

$$X(\omega, \tau) = \int_{-\infty}^{\infty} x(t)w(t-\tau)e^{-i\omega t}\,\mathrm{d}t \tag{2.2.2}$$

Here the function to be transformed is multiplied by a window function $w(t-\tau)$ which is nonzero only for a short period of time. Practically this correspond to dividing the original signal into shorter segments of equal length and then calculate the FT of each segments, giving a 2D representation of the time-varying spectrum.

Often one want a window observation window that changes with frequency. A short window gives good time resolution, allowing for identification of when frequency content changes but poor frequency resolution. On the other hand a long window allows the frequencies to be identified but gives poor time resolution. One such window that gives a varying length is the Gaussian window function. Used with STFT, the transfer is called a Morlet wavelet(WT)

$$X(a, b) = \frac{1}{\sqrt{a}} \int_{-\infty}^{\infty} x(t)\psi\left(\frac{t-b}{a}\right)\,\mathrm{d}t \tag{2.2.3}$$

For the Morlet wavelet the window function is a Gaussian windowed complex sinusoidal, $\psi(t) = e^{-t^2/2}e^{i\omega t}$. a defines the frequency resolution by expanding/contracting the window, see figure 2.2.1, and b is the location of the observation window in the time domain.
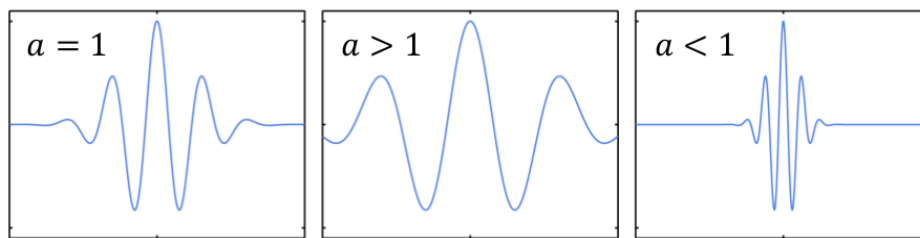

Figure 2.2.1: Influence of a on the window length. Copied from slides given at ULG in Liege, Belgium

2.2.1   Example

Figure 2.2.2(a) shows the wavelet transform of the coupled duffing system (1.5.1). Fig 2.2.2(b) shows the linear transform for comparison and fig 2.2.2(c) the sweep. For the linear system, the two fundamental frequencies ω_1 and ω_2 along with the excitation frequency is seen. Notice that the axis are chosen so the excitation frequency is seen "clearly linear".

For the nonlinear case, higher harmonics are seen as a multiple of the excitation frequency, are seen as well. These are the third, fifth and seventh harmonics, with decreasing intensity. This is expected for a uneven polynomial stiffness and since the third harmonic is present, it can be concluded that the nonlinear stiffness must be a cubic nonlinearity. Thus WT can, besides showing that nonlinearity is present, help characterising the type of nonlinearity (The participation factor of each of the higher harmonics is computed in section 3.2.2). Fig 2.2.2(d) shows the FT of the linear and nonlinear system. As stated, the FT fails to capture the changing frequency content of the nonlinear system.

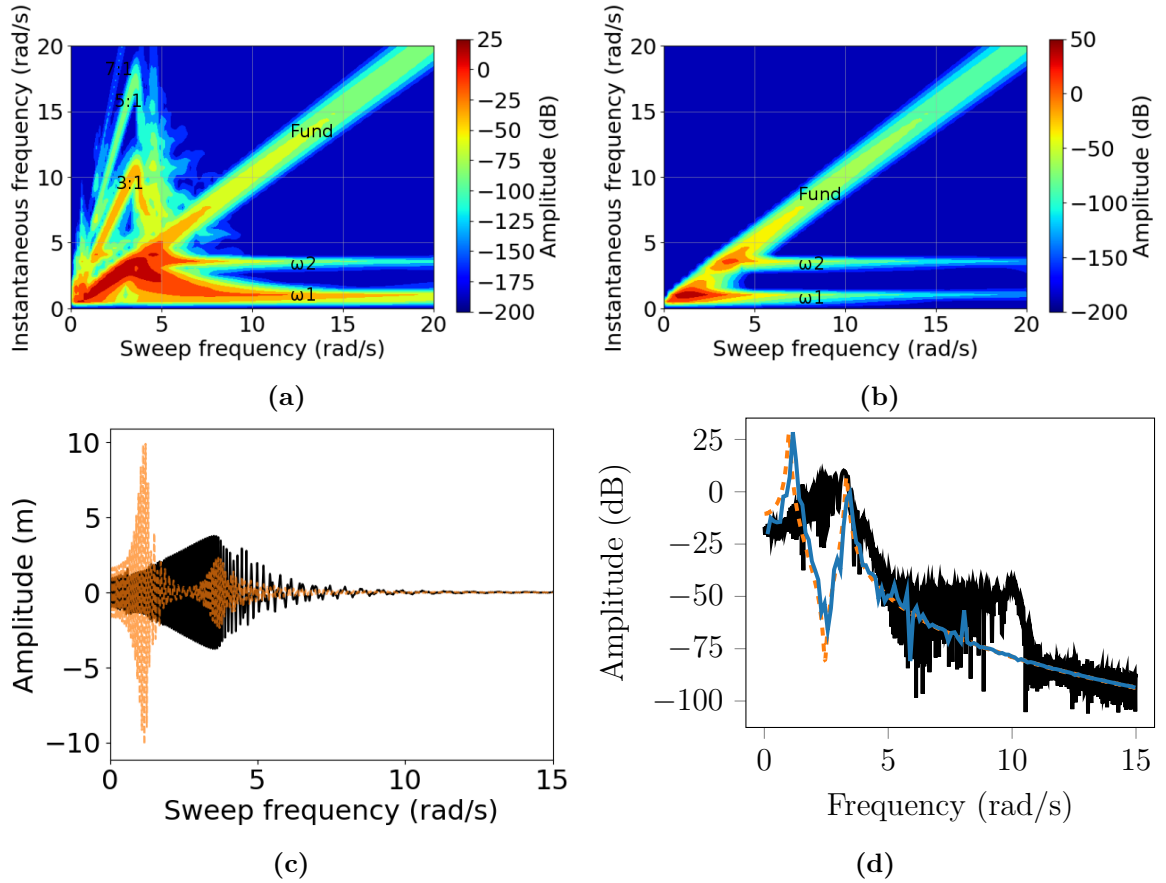**Figure 2.2.2:**   Morlet wavelet transform of a sine sweep of the coupled duffing system. Shown for x_1. **(a)**: WT of the nonlinear system; **(b)**: WT of the underlaying linear system; **(c)**: Sine sweep of ——(nonlinear) and - - - -(linear) system; **(d)**: Fourier transform of the ——(nonlinear) and - - - -(linear) system. ——(nonlinear multisine) is the FRF of a multisine excitation of the nonlinear system.

2.2.2 Summary

The WT shows the instantaneous frequency content of a time signal. Varying frequency content is a sign of nonlinear vibration and the way the spectra changes might give clues to the type of nonlinearity. The frequency spectra is changed in the following way by nonlinear components:

- *Dissipative NLs* does not affect the resonance frequencies much.

- *Hardening (softening) elastic NLs* increase (softens) the resonance frequencies with amplitude.

- *Assymmetric elastic NLs* generate even harmonic components.

- *Symmetric elastic NLs* generate uneven harmonic components.

- *Nonsmooth elastic NLs* generates wideband frequency components.

2.3 Restoring Force Surface

The restoring force surface (RFS) method, introduced by [26] and covered in details in [41], have previously been used as a parameter estimation technique, but is only used as a visual tool for characterization the functional form of the nonlinearity in this report.

   If RFS is used for parameter estimation, an estimation of the inertia for the system is needed. This either requires an FE model or, for more than a few DOFs, an complicated algebraic model.

   The starting point is Newton's second law of written for a specific DOF located next to a nonlinear structural component

$$\sum_{k=1}^{n} m_{i,k}\ddot{x}_k + f_i(\mathbf{x}, \dot{\mathbf{x}}) = p_i \qquad (2.3.1)$$

where i is the DOF of interest, n the number of DOFs in the system, m_{ik} the mass matrix elements, $\mathbf{x}$, $\dot{\mathbf{x}}$ and $\ddot{\mathbf{x}}$ the displacement, velocity and acceleration vectors, respectively, $\mathbf{f}$ the restoring force vector encompassing elastic and dissipative effects, and $\mathbf{p}$ the external force vector.

   Let j denote another measured DOF located across the nonlinear connection, see figure 2.3.1, a new formulation of (2.3.1), which accounts for the difference in displacement and velocity between the selected DOFs, is approximated with

$$m_{i,i}\ddot{x}_i + f_i(x_i - x_j, \dot{x}_i - \dot{x}_j) \approx p_i \qquad (2.3.2)$$

where all inertia and restoring force contributions not related to the nonlinear component are discarded.

   It is further assumed that no external force is applied directly at DOF i (eg. the external force is applied at a different location on the structure), a rearrangement leads to

$$f_i(x_i - x_j, \dot{x}_i - \dot{x}_j) \approx -m_{i,j}\ddot{x}_i \qquad (2.3.3)$$
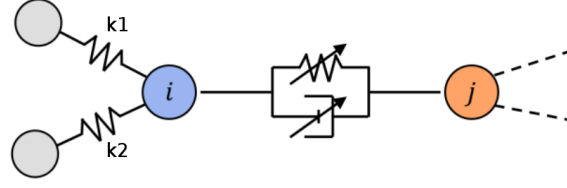
Figure 2.3.1: Nonlinear connection between node i and j. The linear connections $k_{1,2}$ are discarded.

Thus by dropping the constant mass, the nonlinearities can be visualized as the negative acceleration at one side of the connection, as a function of the relative displacement and velocity across this connection. From this an adequate mathematical model can be found.

The shape of f is visualized by plotting the triplet $(x_i - x_j, \dot{x}_i - \dot{x}_j, \ddot{x}_i)$ The form of elastic (dissipative) nonlinearities in the connection is visualized by making a slice along the axis of the zero velocity (displacement) of the restoring force surface plot. Either prior knowledge about the physics or a least square fit can be used to find the functional that best represent the nonlinearity.

The advantages of RFS as presented here, is that it relies exclusively on measured time series and have a visual understanding. It is not commonly used for parameter estimation for MDOF systems, due to the need for direct fitting of Newton's second law. RFS is also called Accelerated Surface Method (ASM) at times in literature.

The major limitations of the RFS method in general is

- Requires the nonlinear dynamics to be excited

- Shows the total restoring force:

  - with multiple nonlinearities it is not possible to distinguish them uniquely.
  - If the nonlinear force is of the same magnitude as the linear force, it might be necessary to remove a linear trend from the RFS to visualise the nonlinear force.

- Works best swept-sine excitation.

- Damping characterisation is difficult due to the low numerical magnitude.

2.3.1   Example

Using a sine sweep excitation on the coupled duffing system (1.5.1) and the RFS methodology,

$$f_i(x_i - x_j, \underbrace{\dot{x}_i - \dot{x}_j}_{<\text{tol}}) \approx -\ddot{x}_i \tag{2.3.4}$$

where *tol* determines the slice thickness, the restoring force is visualised in figs 2.3.2 and 2.3.3 for x_0 and x_1. A hardening stiffness is seen, without any offset, which correspond to a uneven nonlinear polynomial stiffness. In this case a third order polynomial for both DOFs.
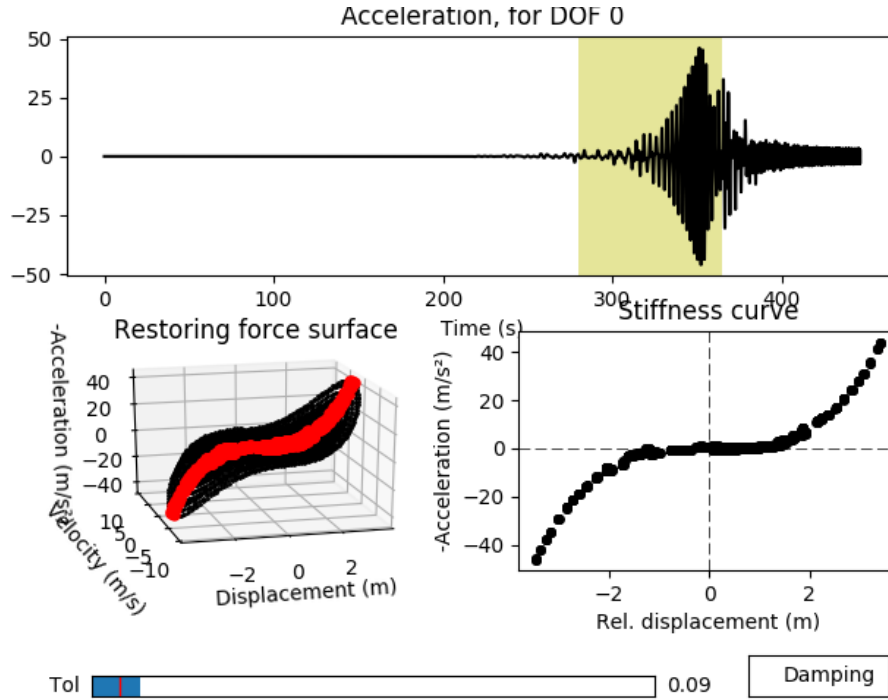
Figure 2.3.2: Interface for selecting the part of the signal used for visualising the restoring force of the coupled duffing system (1.5.1). Here shown for x_1. **upper**: The relevant part of the signal is selected by dragging or resizing the yellow rectangle; **left**: Restoring force surface for the selected part of the signal. The red line shows the slice; **right**: The visualised stiffness. The slice thickness can be changed by dragging the tolerance slider. Damping is visualised by clicking on `damping`.
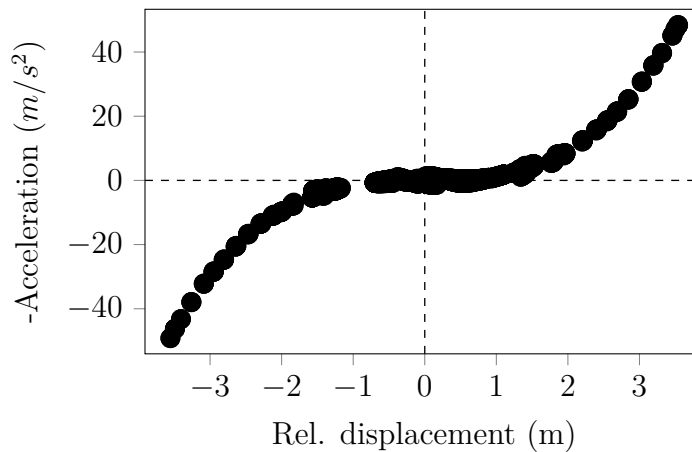
Figure 2.3.3: The visualised stiffness for x_2 from the coupled duffing system (1.5.1). The figure is extracted from the interface shown in fig. 2.3.2; just for x_2 instead

2.3.2 Summary

The RFS provides a direct visualization of the nonlinear stiffness and, to lesser extend, damping curve using a SDOF simplification of the EOMs. The steps are:

- Instrument the nonlinear connection with two accelerometers and use swept sine

excitation.

- Integrate and filter to obtain displacement and velocity.

- Calculate the 3D acceleration surface over a single connection.

- Make surface slides to obtain stiffness and damping curve.

The success of parameter estimation step is conditional upon an accurate characterization of all observed nonlinearities.

2.4 Frequency-domain subspace identification

This section describes a methods for estimation of the underlying linear frequency response function and nonlinear coefficients for nonlinear systems. The method is an (nonlinear) extension of linear subspace methods which are able to deal with multiple-input, multiple-output(MIMO) systems.

The nonlinear subspace methods interpret nonlinearities as unmeasured internal forces, ie. nonlinearities are seen as cause of distortion on the linear FRF matrix. Two main nonlinear methods exist one in time domain, time-domain subspace identification (TNSI)[25], and one in frequency domain, frequency-domain subspace identification (FNSI)[29]. N denotes nonlinear. Both performs equally well in identification and robustness, but the main benefit of FNSI is that the input time series, when converted to frequency domain, can be truncated to a frequency interval of interest and thus reduce the computational time. FNSI is the method used here.

Given the equation of motion for a dynamical system with nonlinearities:

$$\mathbf{M}\ddot{\mathbf{y}}(t) + \mathbf{C}\dot{\mathbf{y}}(t) + \mathbf{K}\mathbf{y}(t) + \mathbf{f}_{nl}\left(\mathbf{y}(t), \dot{\mathbf{y}}(t)\right) = \mathbf{p}(t) \qquad (2.4.1)$$

where $\mathbf{M}$, $\mathbf{C}$ and $\mathbf{K} \in \mathbb{R}^{n \times n}$ are the mass, linear viscous damping and linear stiffness matrices; $\mathbf{y}(t)$ and $\mathbf{p}(t) \in \mathbb{R}^n$ are the generalised displacement and external force vectors; $\mathbf{f}_{nl}(t) \in \mathbb{R}^n$ is the essentially nonlinear restoring force vector comprising elastic and dissipative contributions; n is the number of DOFs. Essentially nonlinear, or nonlinearisable, means that the function is zero and have zero slope at the origin, i.e. it cannot be linearised.

The notation of (2.4.1) assumes that all linear components of the restoring forces in the system are included in the matrices $\mathbf{K}$ and $\mathbf{C}$. The nonlinear restoring force is expressed by a linear combination of s lumped nonlinearities

$$\mathbf{f}_{nl}\left(\mathbf{y}(t), \dot{\mathbf{y}}(t)\right) = \sum_{i=1}^{s} \mu_i \mathbf{b}_i \mathbf{g}_i\left(\mathbf{y}(t), \dot{\mathbf{y}}(t)\right) \qquad (2.4.2)$$

where μ_i is the unknown nonlinear coefficient and $\mathbf{g}_i\left(\mathbf{y}(t), \dot{\mathbf{y}}(t)\right)$ is the the corresponding known (characterised by eg. WT or RFS) functional form (or basis function). The location of the nonlinearity is specified by the boolean vector, $\mathbf{b}_i$.

Moving the nonlinear terms of (2.4.1) to the right-hand side

$$\mathbf{M}\ddot{\mathbf{y}}(t) + \mathbf{C}\dot{\mathbf{y}}(t) + \mathbf{K}\mathbf{y}(t) = -\sum_{i=1}^{s} \mu_i \mathbf{b}_i \mathbf{g}_i(t) + \mathbf{p}(t) \qquad (2.4.3)$$

the system may be viewed as the underlying linear system subjected to the external force $\mathbf{p}(t)$ and the internal feedback force due to nonlinearities, as shown in figure 2.4.1.
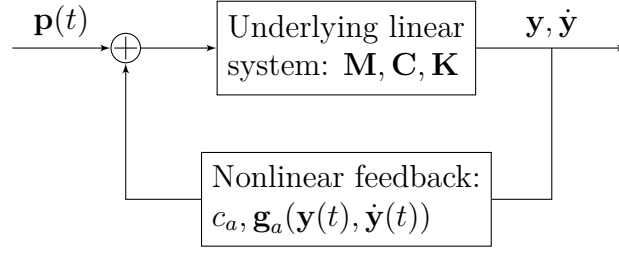

Figure 2.4.1: Feedback interpretation of nonlinear structural dynamics.

Using the state vector $\mathbf{x} = [\mathbf{y}, \dot{\mathbf{y}}]^T$, the system (2.4.3) is rewritten as the state space formulation

$$\dot{\mathbf{x}}(t) = \mathbf{A}_c \mathbf{x}(t) + \mathbf{B}_c \mathbf{e}(t)$$
$$\mathbf{y}(t) = \mathbf{C}\mathbf{x}(t) + \mathbf{D}\mathbf{e}(t) \tag{2.4.4}$$

where subscript c denotes *c*ontinuous time. $\mathbf{e}(t) = [\mathbf{p}(t)^T, g_1, \ldots, g_s]^T \in \mathbb{R}^{n+s}$ is the extended input vector which concatenates external and nonlinear terms.

State-space and physical matrices have the relations

$$\mathbf{A}_c = \begin{bmatrix} \mathbf{O} & \mathbf{I} \\ -\mathbf{M}^{-1}K & -\mathbf{M}^{-1}\mathbf{C} \end{bmatrix}$$

$$\mathbf{B}_c = \begin{bmatrix} \mathbf{0} & \mathbf{0} & \mathbf{0} & \ldots & \mathbf{0} \\ \mathbf{M}^{-1} & -\mu_1 \mathbf{M}^{-1}\mathbf{b}_1 & -\mu_2 \mathbf{M}^{-1}\mathbf{b}_2 & \ldots & -\mu_s \mathbf{M}^{-1}\mathbf{b}_S \end{bmatrix} \tag{2.4.5}$$

$$\mathbf{C} = \begin{bmatrix} \mathbf{I} & \mathbf{0} \end{bmatrix} \qquad \mathbf{D} = \mathbf{0}$$

The state matrices are: $\mathbf{A}$ and $\mathbf{B}$ the input and nonlinear coefficients matrix, the output matrix $\mathbf{C}$ and the direct feed through matrix $\mathbf{D}$.

Before Fourier transforming the system, a continuous to discrete-time conversion of the state matrices are used with the sampling frequency f_s. This is done in order to improve the numerical condition and given by

$$\mathbf{A}_d = \text{expm}(\mathbf{A}_d/f_s), \quad \mathbf{B}_d = (\mathbf{A}_d - \mathbf{I})\mathbf{A}_c^{-1}\mathbf{B}_c$$
$$\mathbf{C}_d = \mathbf{C}_c, \quad \mathbf{D}_d = \mathbf{D}_c \tag{2.4.6}$$

It is stressed[29] that the conversion is only strictly valid if the input signals in $\mathbf{e}$ are piece-wise constant between sampling instants, called a zero-order hold intersample assumption. This is generally not the case but if a sufficiently high sampling frequency is used, the continuous time model is not affected. It is not clear how high a *sufficiently high sampling frequency* is.

Using a discrete Fourier transform, the system is

$$z_k \mathbf{X} = \mathbf{A}_d \mathbf{X}(k) + \mathbf{B}_d \mathbf{E}(k)$$
$$\mathbf{Y}(k) = \mathbf{C}\mathbf{X}(k) + \mathbf{D}\mathbf{E}(k) \tag{2.4.7}$$

where $z_k = e^{(2i\pi k/N_s)}$ is the z-transform variable for discrete time models and N_s the number of recorded samples in the time series. $\mathbf{X}, \mathbf{Y}$ and $\mathbf{E}$ are the discrete Fourier transforms of $\mathbf{x}, \mathbf{y}$ and $\mathbf{e}$. The subscript d are dropped in the following, as all operations are on discrete time models.

2.4.1 The output-state-input equation

The extended input $\mathbf{E}$ and output $\mathbf{Y}$ are known. The system matrices $\mathbf{A}$ and $\mathbf{B}$ needs to be determined. As seen from eq. (2.4.5) $\mathbf{C}$ and $\mathbf{D}$ are known, but are still estimated as part of the subspace method. These estimates of course match the known values.

Frequency-domain subspace methods estimates these matrices based on a reformulation of the state-space eqs. (2.4.7) in matrix form, where the input and output is rearranged into Hankel-type block matrices.

The matrix of the measured output spectra is

$$
\mathbf{Y}_i =
\begin{bmatrix}
\mathbf{Y}(1) & \mathbf{Y}(2) & \dots & \mathbf{Y}(F) \\
z_1\mathbf{Y}(1) & z_2\mathbf{Y}(2) & \dots & z_F\mathbf{Y}(F) \\
z_1^2\mathbf{Y}(1) & z_2^2\mathbf{Y}(2) & \dots & z_F^2\mathbf{Y}(F) \\
\vdots & & & \\
z_1^{i-1}\mathbf{Y}(1) & z_2^{i-1}\mathbf{Y}(2) & \dots & z_F^{i-1}\mathbf{Y}(F)
\end{bmatrix}
\tag{2.4.8}
$$

which by defining $\xi = \mathrm{diag}(z_1, z_2, \dots, z_F)$ is recast to

$$
\mathbf{Y}_i = \begin{bmatrix} \mathbf{Y}^T & (\mathbf{Y}\xi)^T & \dots & (\mathbf{Y}\xi^{i-1})^T \end{bmatrix}^T
\tag{2.4.9}
$$

and similar the matrix of extended input spectra is formed as

$$
\mathbf{E}_i = \begin{bmatrix} \mathbf{E}^T & (\mathbf{E}\xi)^T & \dots & (\mathbf{E}\xi^{i-1})^T \end{bmatrix}^T
\tag{2.4.10}
$$

where i is a user-defined number of block rows in $\mathbf{Y}_i$ and F the number of frequency lines used for identification; more on how these are chosen later.

Introducing the extended observability matrix

$$
\mathbf{\Gamma}_i = \begin{bmatrix} \mathbf{C}^T & (\mathbf{CA})^T & \dots & (\mathbf{CA}^{i-1})^T \end{bmatrix}^T
\tag{2.4.11}
$$

and the lower-block triangular Toeplitz matrix

$$
\mathbf{H}_i =
\begin{bmatrix}
\mathbf{D} & \mathbf{0} & \mathbf{0} & \dots & \mathbf{0} \\
\mathbf{CB} & \mathbf{D} & \mathbf{0} & \dots & \mathbf{0} \\
\mathbf{CAB} & \mathbf{CB} & \mathbf{D} & \dots & \mathbf{0} \\
\vdots & & & & \\
\mathbf{CA}^{i-2}\mathbf{B} & \mathbf{CA}^{i-3}\mathbf{B} & \mathbf{CA}^{i-3}\mathbf{B} & \dots & \mathbf{D}
\end{bmatrix}^T
\tag{2.4.12}
$$

then by recursive use of eq. (2.4.7) and the above matrices [29], the output-state-input matrix equation, which is used for estimation in the subspace method, is obtained

$$
\mathbf{Y}_i = \mathbf{\Gamma}_i\mathbf{X} + \mathbf{H}_i\mathbf{E}_i
\tag{2.4.13}
$$

2.4.2 Estimation of state matrices

The subspace method is applied to eq. (2.4.13) in order to estimate $\mathbf{\Gamma}_i$. When $\mathbf{\Gamma}_i$ is estimated, the state matrices of eq. (2.4.7) are extracted and calculated.

The method have two main steps:

- Eliminate the term depending on nonlinearities and forces in eq. (2.4.13), ie $\mathbf{H}_i$ by its inclusion of $\mathbf{B}$. This is done by projecting the equation onto the orthogonal complement of $\mathbf{E}_i$,

$$\mathbf{Y}_i/\mathbf{E}_i^\perp = \mathbf{\Gamma}_i \mathbf{X}/\mathbf{E}_i^\perp + \underbrace{\mathbf{H}_i \mathbf{E}_i/\mathbf{E}_i^\perp}_{=0} = \mathcal{P} \tag{2.4.14}$$

The geometrical interpretation of this is shown in figure 2.4.2 for the 2d case.

$\mathbf{\Gamma}_i$ is then estimated from a singular value decomposition(SVD) of the projection $\mathcal{P}$

- When $\mathbf{\Gamma}_i$ is estimated, the four state space matrices $(\mathbf{A}, \mathbf{B}, \mathbf{C}, \mathbf{D})$ are calculated.

See figure 2.4.3 for a overview.

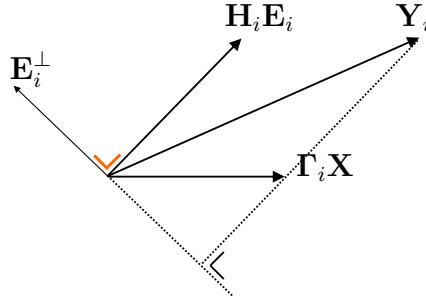
Figure 2.4.2: Geometric interpretation of eq. (2.4.13) in two dimensional space. The orthogonal complement of $\mathbf{E}_i$, $\mathbf{E}_i^\perp$, is the set of all vectors that are orthogonal to every vector of $\mathbf{E}_i$ (thus it is also the null space of $\mathbf{E}_i$). In the 2d case, $\mathbf{E}_i^\perp$ is simply the vector perpendicular to $\mathbf{E}_i$, and the projection of $\mathbf{Y}_i$ onto $\mathbf{E}_i^\perp$ cancels the extended input term $\mathbf{H}_i \mathbf{E}_i$.

Three assumptions are assumed to be fulfilled for the subspace methods,

1. All the linear modes of vibration in the frequency band of interest are excited or, alternatively, they are all observable in input-output data.

2. The row space of the states $\mathbf{X}$ and of the extended input spectra matrix $\mathbf{Y}_i$ does not share information,

$$\text{span}_{\text{row}}(\mathbf{X}) \cap \text{span}_{\text{row}}(\mathbf{E}_i) = 0$$

3. The extended inputs $\mathbf{E}_i$ are of full rank, i.e.,

$$\text{rank}(\mathbf{E}_i) = (s + n)i$$

eg. excitations and the nonlinearities have to be such that the inversion of the problem is well-posed.

To expand on the second assumption: The state term $\mathbf{AX}$ contains linear stiffness and damping information. If constant and/or linear terms are introduced in the nonlinear basis functions, the intersection between the states and the extended inputs $\mathbf{E}_i$ is no longer empty, which violate the assumption. This requires nonlinear basis functions to be nonlinearisable.

1. Choose the index i and the number of processed frequency lines F

2. Concatenate external forces and nonlinearities to form the extended input spectra $\mathbf{E}_i$

3. Compute the orthogonal projection

$$\mathcal{P} = \mathbf{Y}_i / \mathbf{E}_i^{\perp}$$

using QR-decomposition.

4. Compute the SVD of $\mathcal{P}$

$$\mathcal{P} = \mathbf{USV} \tag{2.4.15}$$

5. Determine model order n from singular values in $\mathbf{S}$ or from a stabilisation diagram. Truncate $\mathbf{U}$ and $\mathbf{S}$ accordingly to define $\mathbf{U}_1$ and $\mathbf{S}_1$.

6. Estimate the extended observability matrix $\mathbf{\Gamma}_i$

$$\hat{\mathbf{\Gamma}}_i = \mathbf{U}_1 \mathbf{S}_1^{1/2}$$

7. Estimate $\mathbf{A}$ using the shift property of $\mathbf{\Gamma}_i$,

$$\underline{\mathbf{\Gamma}_i}\hat{\mathbf{A}} = \overline{\mathbf{\Gamma}_i} \iff \hat{\mathbf{A}} = \underline{\mathbf{\Gamma}_i}^+ \overline{\mathbf{\Gamma}_i}$$

where $\underline{\mathbf{\Gamma}_i}$ and $\overline{\mathbf{\Gamma}_i}$ are the matrix $\mathbf{\Gamma}_i$ without its first and last l rows. $\mathbf{C}$ is extracted as the first block row of $\mathbf{\Gamma}_i$.

8. Estimate $\mathbf{B}$ and $\mathbf{D}$ by defining the extended FRF $\mathbf{H}^e(k)$ (or as this within the z-transform it might be termed *transfer function*).

$$\mathbf{H}^e(k) = \mathbf{C}(z_k\mathbf{I} - \mathbf{A})^{-1}\mathbf{B} + \mathbf{D}$$

and minimise the difference between the measured and modelled output spectra in a linear least square sense, i.e.

$$\hat{\mathbf{B}}, \hat{\mathbf{D}} = \arg\min_{\mathbf{B},\mathbf{D}} \sum_{k=1}^{F} |\mathbf{Y}(k) - \mathbf{H}^e(k)\mathbf{E}(k)|^2$$

9. Convert $\mathbf{A}, \mathbf{B}, \mathbf{C}$ and $\mathbf{D}$ into continuous-time matrices and form the extended FRF $\mathbf{H}^e(\omega)$.

$$\mathbf{H}^e(\omega) = \mathbf{C}_c\left(j\omega\mathbf{I}^{n\times n} - \mathbf{A}_c\right)^{-1}\mathbf{B}_c + \mathbf{D}_c \tag{2.4.16}$$

10. Estimate the nonlinear coefficients μ_j and the linear FRF matrix $\mathbf{H}(\omega)$. The FRF matrix of the underlying linear system $\mathbf{H}(\omega)$ and the nonlinear coefficients μ_s are found from (2.4.16) as

$$\mathbf{Y}(\omega) = \mathbf{H}(\omega)\left\{\mathbf{I} \quad -\mu_1\mathbf{b}_1 \quad ... \quad -\mu_s\mathbf{b}_s\right\}\mathbf{E}(\omega) = \mathbf{H}^e(\omega)\mathbf{E}(\omega) \tag{2.4.17}$$

Figure 2.4.3: Overview of the FNSI methodology

2.4.3 Types of nonlinear basis functions

As stated, the nonlinear basis functions should be zero and have zero slope at the origin. For continuous nonlinear restoring force, polynomial functions with order chosen from WT- and RFS plots can be used. For discontinuous systems, e.g. contact, polynomials might not be well suited; higher order polynomials might exhibit oscillations around the origin. An alternative is to use piecewise cubic spines instead. Even if they cannot realise a perfect fitting (they are continuous by nature), they are appropriate for representing sudden events, like sharp changes in stiffness(or damping) curves. Cubic splines and polynomials can be mixed. See section 5.2.2 for the formulation needed for using splines.

Using cubic splines might be termed *gray box* identification where using polynomials is *white box*. The difference is that with gray box, the nonlinearities are described by functions that may represent a vast variety of nonlinear behaviour and thus requiring less specific knowledge of the underlying physics.

2.4.4 Estimating model order

In order to do parameter estimation, the number of block rows i in the Hankel matrices, used frequency lines F and the model order n must be chosen by the user. There is no strict way to chose i, the only requirement is that it is chosen greater than the system order n. In theory the larger i, the more accurate estimation (which is true until a given limit, where the repeated inclusion of the system dynamics affects the conditioning). In practice the identification is not that sensitive to the value of i, but a too large value impact the computational time.

The frequency lines F, ie. the frequency content to include in the estimation, are often chosen as the same as the excitation frequency band. If the structure is excited with a $0 - 150$Hz band, F could be chosen as $5 - 150$Hz, neglecting low-level and *out-of-input-band* frequencies. Or chosen as the frequencies around resonances of the system, neglecting the frequencies with low throughput. The reason for truncating the frequencies are to save computational time.

The model order n is strictly the number of total linear modes of the system eq. (2.4.1), but in practice only a limited set modes are excited during measurement. Thus to determine n, is equal to determine the number of modes excited in the chosen frequency interval F. This means that stabilisation diagram can be used to determine n instead of inspecting the singular values of $\mathbf{S}$, eq. (2.4.15).

To calculate a stabilisation diagram, the linear modal parameters are estimated for a given model order, ie. natural frequency, damping and mode shape. These modal parameters are then compared to the modal parameters calculated using a *one higher* model order. Comparing modal parameters for each identified mode of the two model orders then gives the stability: *stabilisation in frequency*, *stabilisation in damping* and *stabilisation of the mode shape*. If all three parameters are stabilised the mode is full stabilised. The natural frequencies and damping are compared to some tolerance chosen by the user and stabilisation of the mode shape is calculated by the modal assurance criterion(MAC)[2],
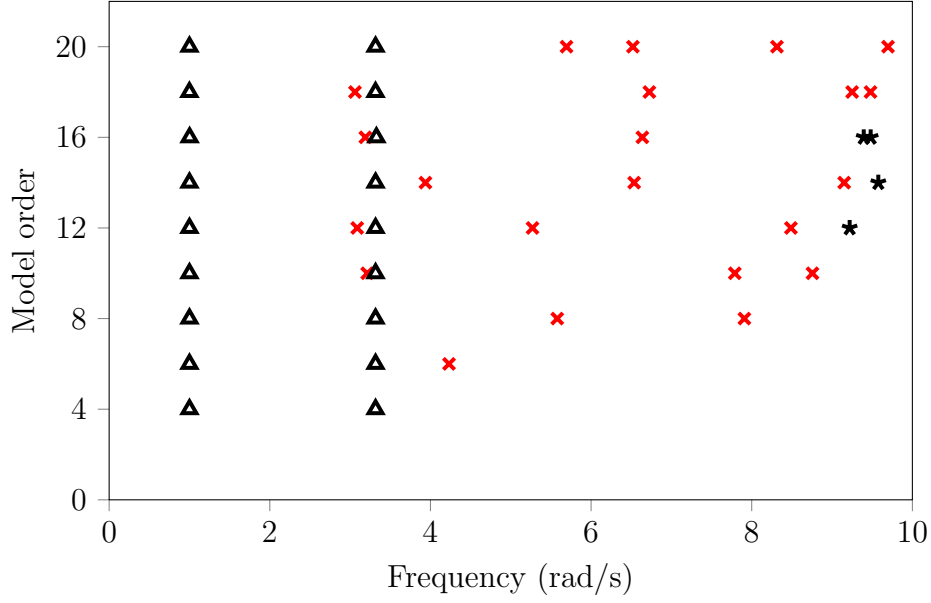
Figure 2.4.4: Estimation of model order. Stabilisation diagram with linear FRF overlayed. Two modes are identified. ×: new natural frequency(termed pole); ⋆: stabilisation in natural frequency; △: full stabilisation. Stabilisation thresholds in natural frequency, damping ratio and MACX value are $0.5\%, 2\%, 0.98$, respectively.

$$MACX(r,q) = \frac{|\boldsymbol{\psi}_r^T \boldsymbol{\psi}_q^*|^2}{\left(\boldsymbol{\psi}_r^T \boldsymbol{\psi}_r^*\right)\left(\boldsymbol{\psi}_q^T \boldsymbol{\psi}_q^*\right)} \tag{2.4.18}$$

If the model order is chosen too low, it will result in unmodelled dynamics, whereas too large order lead to overmodelling issues such as an increase of the noise sensitivity of the model. It should be noted that model selection requires that adequate basic functions are used.

Without anticipating the example, a stabilisation diagram for the coupled duffing system is shown in figure 2.4.4 along with singular values of **S** in figure 2.4.5. The two modes are clearly seen. From the stabilisation diagram a model order of four is chosen. This gives stabilisation in the linear parameters. The plot of the singular values shows a jump of six orders magnitude between model order four and five, verifying the chosen model order. In general only the stabilisation diagram is used as it gives more detailed information; the singular value plot is only used if a stabilisation diagram is not implemented.

The determination of the model order is very simple and clear here. For larger system this might not be the case, see [30] for an example.

2.4.5 Example

The coupled duffing system is excited with a periodic multisine a integer number times. Using a periodic signal a integer number of times should avoid leakage[12]. Figure 2.4.6 shows the periodicity of the recorded signal. The periodicity is calculated by using the signal of the last period as a reference and then subtracting this reference from each of
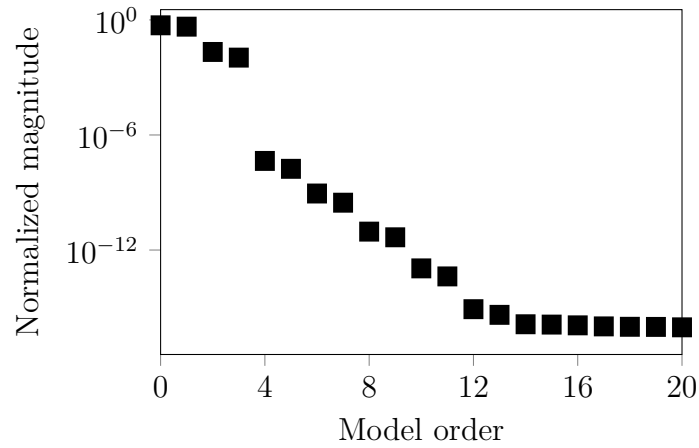
Figure 2.4.5: First twenty singular values. A jump of six orders magnitude is seen between model order four and five.

the previous periods. If the difference between the reference and a previous period is close to zero, often shown in a logarithmic scale, the periodicity between the reference and the compared period is low. Ie. the periodicity is a way to verify that transient effects are died out.

To summarise; for estimation multiple periods can be used, but transient effects should not be present; which is indicated by a low periodicity. In this case periods 4-9 could be used.
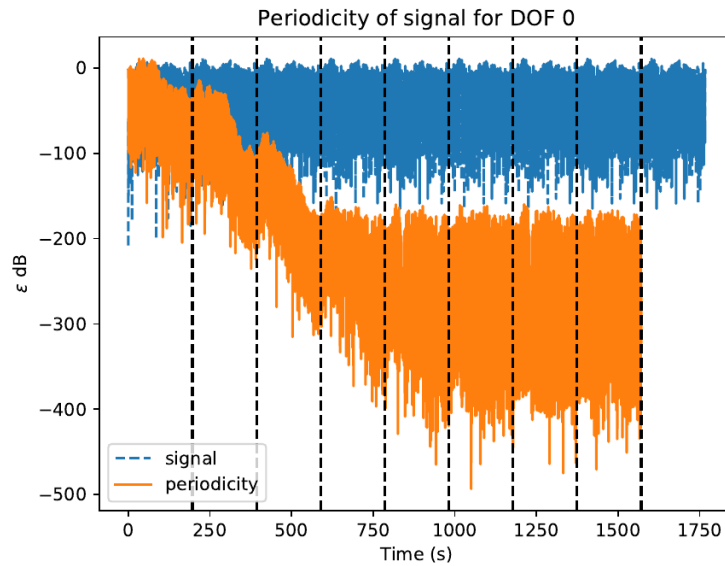
Figure 2.4.6: Periodicity (or difference between periods) of recorded signal at DOF 0. Vertical lines indicate periods. A low periodicity shows that transient effects have died out. Blue is the original signal and yellow the periodicity.

The estimation of the nonlinear parameters of the system is shown in figure 2.4.7 for model order four. The variation of the real part of μ is shown in a 1% interval, with very little frequency dependency in the frequency range of interest. The imaginary

part is about three orders of magnitude smaller. Both indicates a good quality of the estimation. The spectral averages are

$$\begin{aligned} \mathrm{Re}(\mu_1) &= 1.000, \quad \mathrm{Im}(\mu_1) = 1.09 \times 10^{-4} \\ \mathrm{Re}(\mu_2) &= 1.000, \quad \mathrm{Im}(\mu_1) = 7.73 \times 10^{-4} \end{aligned}$$

(2.4.19)

and matching the simulated values well.
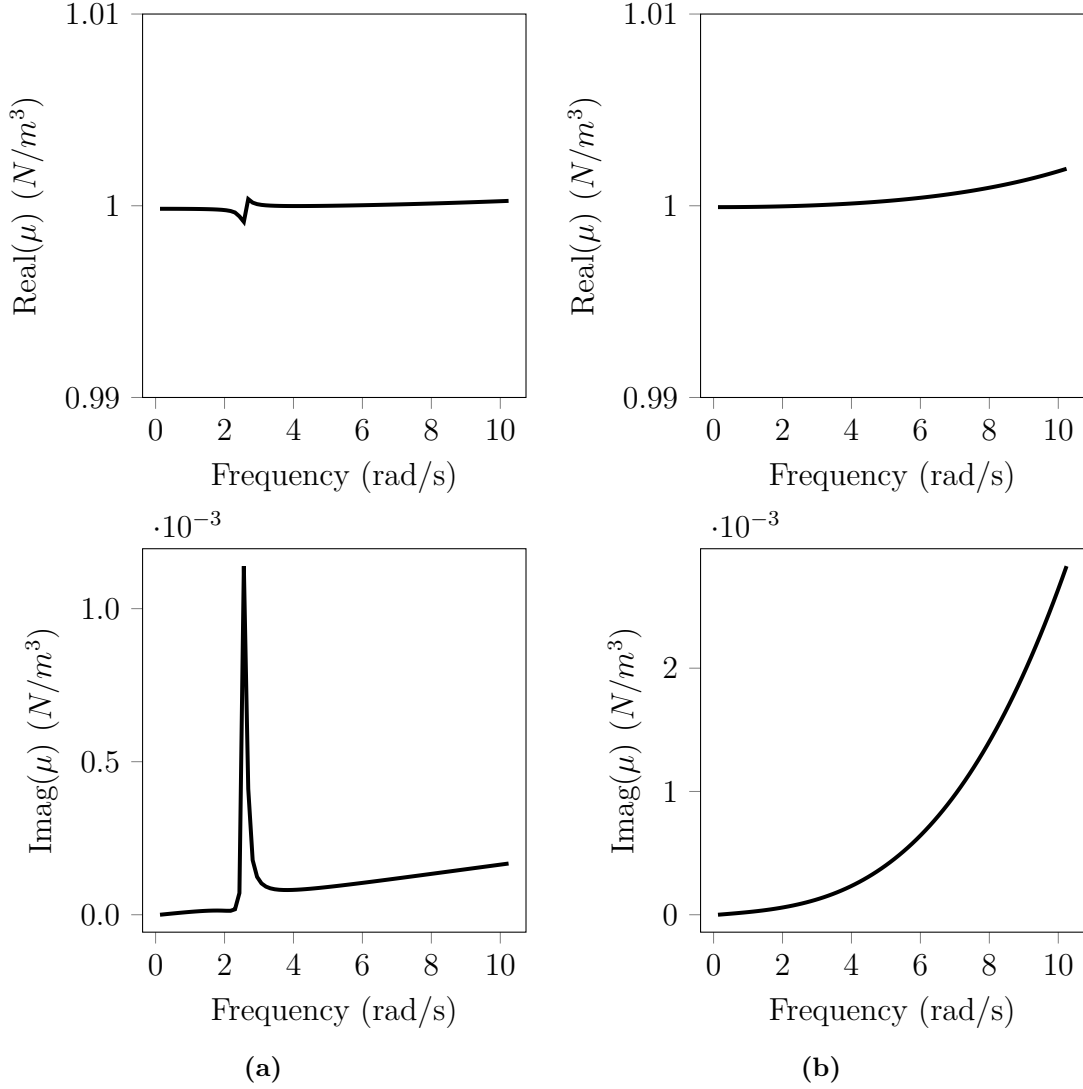
Figure 2.4.7: Real and imaginary part of estimated nonlinear coefficients μ_1 and μ_2. The variation of $\mathrm{Re}(\mu)$ is shown in a 1% interval, with very little frequency dependency in the frequency range of interest. The imaginary part is about three orders of magnitude smaller. Both indicates a good quality of the estimation. **(a)**: μ_1; **(b)**: μ_2.

The FNSI method also estimate the underlaying linear properties. As seen from table 2.4.1, the linear parameters are identified correctly. Ensuring that linear parameters are identified, also shows that nonlinear coefficients are identified correct.

Mode	Frequency (rad/s)	Damping ration (%)
1	1.00	5.00
2	3.32	1.51
1	1.19	3.96
2	3.40	1.41

Table 2.4.1: Estimated linear natural frequencies and damping ratios for the coupled Duffing system. **(upper)**: Nonlinear identification with FNSI; **(lower)**: Linear identification

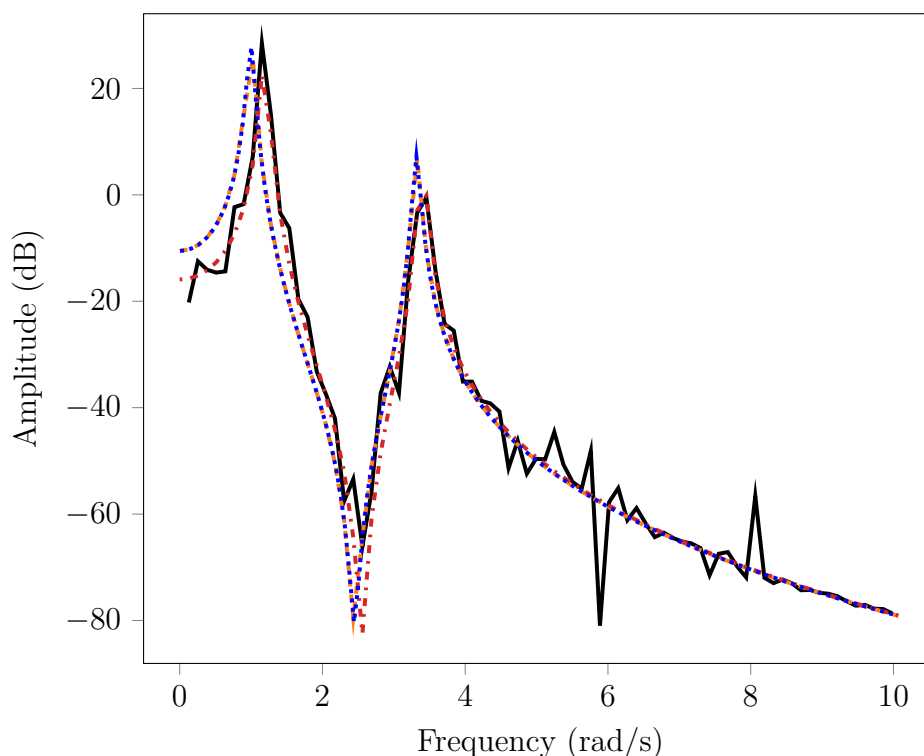Figure 2.4.8 shows the FRF. The linear FRF found by FNSI match the theoretical linear FRF.

Figure 2.4.8: FRF calculated as H_1 for the coupled duffing system. ——: H1 from signal; —·—: Linear identified; ----: Nonlinear identified from FNSI; ·······: Theoretical linear

2.4.6 Estimation error

It seems that the FNSI method works quite well - both nonlinear and linear parameters are estimated with high accuracy - as seen from the simple example and in a broader sense: [29–31, 33].

However as shown in [14] spurious terms appears in the estimated $\mathbf{B}_c$ matrix. These terms have only limited affect on the estimated parameters, but if the estimated state space matrices are used directly for simulation purposes, ie. coupling a numerical continuation method directly with the state space model to obtain a NFRC without building a FE model, the spurious terms does affect the location of resonance peaks as they are acting as damping.

The spurious terms in $\mathbf{B}_c$ arise from the conversion between discrete- and continuous time. As stated, the identification is done in discrete time, but the state space model is used in continuous time. To quote J.P Noel, who introduced FNSI, from a mail correspondence:

> The continuous-time models are well suited for mechanical applications. The reason for this is that continuous-time identification assumes that data are acquired in band-limited conditions, i.e. that the input and the output are only measured over a finite set of frequencies, which is always the case in a mechanical setup. However, from a numerical point of view, it is more stable to carry out the identification in discrete time which is done, knowing that this creates an error.

A final remark is that the state space matrices are not found within a basis for the physical coordinate system, ie. wrt. to the vector basis $\mathbf{x} = [\mathbf{y}^T, \dot{\mathbf{y}}^T]^T$. It was not mentioned in the overview fig. 2.4.3, but the estimation of the extended observability matrix $\mathbf{\Gamma}$ is done within a similarity transformation matrix $\mathbf{T}$, ie.

$$\mathbf{\Gamma} = \mathbf{U}_1 \mathbf{S}_1^{1/2} \mathbf{T} \tag{2.4.20}$$

where the similarity transform is chosen as $\mathbf{T} = \mathbf{I}$ and thus omitted in successive steps. But this fixes the state-space basis and as the nonlinear components of $\mathbf{B}$ changes with the basis, they cannot be extracted from $\mathbf{B}$ by using a similarity transform changing the basis to physical coordinates. This is the reason why the nonlinear coefficients have to be extracted from the invariant extended FRF $\mathbf{H}^e$ and not simply found by inspection of $\mathbf{B}$.

Without any explanation it is stated the similarity transform

$$\mathbf{T} = \begin{bmatrix} \hat{\mathbf{C}} \\ \hat{\mathbf{C}}\hat{\mathbf{A}} \end{bmatrix}, \quad \mathbf{A} = \mathbf{T}\hat{\mathbf{A}}\mathbf{T}^{-1}, \quad \mathbf{C} = \hat{\mathbf{C}}\mathbf{T}^{-1} \tag{2.4.21}$$

gives the state matrices $\mathbf{A}, \mathbf{C}$ in physical space, ie. matching the formulation eq. (2.4.5). ˆ denotes the estimated matrices.

2.4.7 Summary

The FNSI method is able to identifying multiple nonlinear parameters for system with many DOFs. It differs from time domain methods, with the ability to truncate measured signals to the frequency intervals of interest making computations faster for large systems.

Characterisation of the nonlinearity is important to get a good estimation. If there is limited knowledge about the nonlinearity, cubic splines can be used instead of polynomials. In general the following steps can be used to check the validity of the identification:

- Check the stabilisation of the first mode.

- Check the modal parameters compared to linear identification.

- Check the stability of the nonlinear coefficients versus frequency.

- Check the magnitude of the imaginary parts of the coefficients.

Chapter 3

From identification to design

This chapter deals with the prediction of behaviour of nonlinear system, after nonlinear components have been determined. Paraphrased it could be called *virtual prototyping*. Here methods to detect bifurcations, stability and internal resonance are presented. The long-term ambition is to use this knowledge to understand and improve design, taking nonlinear behaviour into account.

This chapter represent a change of methodology. Where the methods for identification in the previous chapter relied exclusively on time signals, the methods of this chapter relies exclusively on FE models. The information from identification is used to build an accurate computer model.

Two methods are treated: Harmonic balance(HB) continuation, used for computation of NFRC and detecting and identifying bifurcations, and nonlinear normal modes(NNM) continuation, used to detect internal resonance.

Before presenting the methods, the concept of NNMs is reviewed.

3.1   Nonlinear normal modes

This is brief introduction to nonlinear normal modes(NNMs). NNMs are considered an extension to linear normal modes(LNM), but without the mathematical properties of LNMs. Where LNMs decouple eoms, ie. a solution can be written as a linear combinations of LNMs, and are invariant, this is not the case for NNMs.

Instead NNMs are defined as *(non-necessarily) synchronous periodic motion of the system* [19] and computed for the undamped and unforced system, ie. the hamiltonian system. Synchronous means that all parts of a system reaches their extreme values and passes through zero at the same time, ie. vibration in unison. In the case of internal resonance, where one part vibrates at a integer number of another parts frequency, the vibration can still be periodic but it is no longer in unison. This which is why the original definition of NNMs as strict synchronous motion by Rosenberg in 1966 [36] was relaxed to the current formulation by Kerchen. Thus today, NNMs are simply periodic oscillations of a conservative system.

NNM have the following properties/features

- *Frequency-energy dependence*:
  Nonlinear systems shows a frequency-energy dependence of their oscillations, eg. through hardening or softening behaviour. NNMs plotted in a frequency-energy plot show this dependency.

- *Internal resonances*:
  NNMs at well-separated fundamental frequencies may interacts and exchange energy.

  To expand a bit: At low energies these modes may have incommensurate natural frequencies and do not satisfy internal resonance conditions. Due to the energy dependence of their frequencies, however, at higher energies the same NNMs may become internally resonant, as their energy-dependent frequencies may become commensurate, giving strong nonlinear modal interactions

- *Traces the lotus of NFRCs*:
  For structures with low damping, the NNM backbone traces the locus of the resonance peaks.

where the energy of the system is the sum of the potential and kinetic energy.

The periodic motion of different NNMs of the same system, might include a different number of harmonics, ie. there is a nonlinear relationship between the coordinates during the periodic motion. This can be seen from the configuration space (ie. a plot of x_1 vs. x_2 for a 2dof example) where the modal line will either be a straight line, as is the case for LNMs, or a curve when different harmonics are present where the shape of the curve depends on the energy of the system.

The latter is the generic case and termed *nonsimilar* NNMs. When special spatial symmetries exist, the NNMs may degenerate into (energy-invariant) straight modal line even if the system is nonlinear, termed *similar* NNMs. An example of the latter is given in section 3.1.1.

A more in-depth investigation and history of NNMs can be found in [19] and the monograph [40, chap 2.].

3.1.1 Example

To exemplify some of the fundamental properties of NNMs, the undamped and unforced 2dof system shown in fig. 3.3.1 is used.
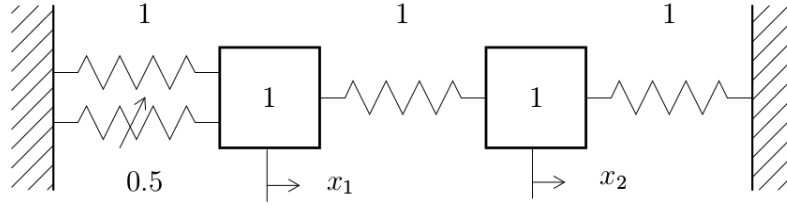

Figure 3.1.1: Schematic representation of the 2DOF system

where the equations of motion are

$$
\ddot{x}_1 + (2x_1 - x_2) + 0.5x_1^3 = 0
$$
$$
\ddot{x}_2 + (2x_2 - x_2) = 0 \tag{3.1.1}
$$

This system is said to have an in-phase and out-of-phase mode. The method for calculating NNMs is given later in section 3.2.1.

Frequency-energy dependence

As already stated, nonlinear systems have a frequency-energy dependence of their oscillations. As a consequence the FRF is not invariant. For NNMs, the modal curves and frequencies also depends on the energy. NNMs are often represented in a frequency-energy plot (FEP), where a NNM is represented by a family of points, drawn at the minimal period of the periodic motion and at an energy equal to the conserved total energy during the motion. A branch, represented by a solid line, is a family of NNM motions possessing the same qualitative features (eg. the in-phase NNM motions of a 2dof system).

The The FEP of the 2dof system (3.1.1) is shown in fig 3.1.2. The backbone of the plot is formed by two branches, which represent in-phase (bottom) and out-of-phase (top) synchronous NNMs. The FEP shows that nonlinear modal parameters depend on vibrational energy:

- The frequency(ie. the minimal period), of both the in-phase and out-of-phase NNMs increases with the energy level, due to the hardening characteristic of the system.

- The modal curves, ie. the curve drawn in the configuration space defined by the displacements x_1 and x_2, change for increasing energies. They are seen in the insets. As energy increases, the straight line becomes curved as a sign of the nonlinear relationship which exists between x_1 and x_2.

- Although the energy is shared between the two dofs at low-energy, the NNMs localise to either dof for increasing energies. The in-phase NNM localise to the second dof, whereas the out-of-phase NNM localizes to the first dof, as seen by the shape of the modal curve.
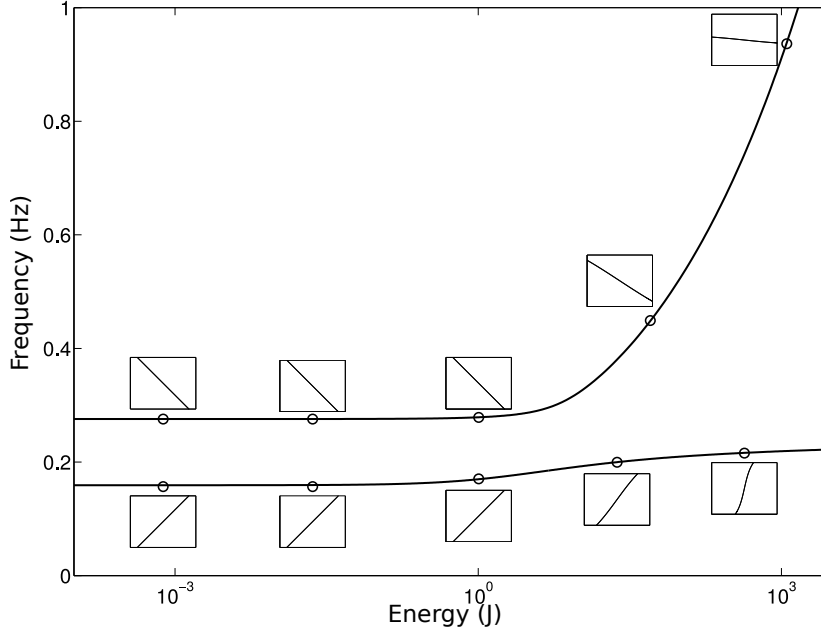
Figure 3.1.2: Frequency-energy plot of the 2dof system (3.1.1). NNM motions depicted in the configuration space are shown in inserts. The aspect ratio of the inserts are equal, used to indicate whether or not the motion is localised to a particular dof.

Modal interactions through resonance

The ratio between the linear natural frequencies of the 2dof system (3.1.1) is $\sqrt{3}$. Thus they are not commensurate(ie. $\frac{\omega_1}{\omega_2}$ is not a rational number), and internal resonance should not occur between the modes.

But due to the frequency-energy dependence and that the frequency of the in-phase NNM increases less rapidly than that of the out-of-phase, a 3:1 ratio between the two (mode) frequencies can still be realised. This is seen in the FEP fig. 3.1.3, where a new branch of periodic solutions emerges from the in-phase backbone, termed a tongue, and enlarged at the insert. The dashed line is the out-of-phase backbone shown at one-third of its frequency, and the point it intersect is the point of internal 3:1 resonance.

The frequency of the out-of-phase NNM increases unbounded for increasing energies, whereas the in-phase NNM asymptotically approaches $\sqrt{3}$. From this follows that there, in the formulated framework of NNMs, are a infinity of internal resonance, ie. 3:1, 4:1, 5:1, etc. Most of these are very hard to realise due lack stability on the thongs and the very large energies(ie. very large displacements) needed.

Figure 3.1.4 shows the 3:1 resonance. The motion is still periodic, but not in unison.

Mode bifurcation and stability

A third property of NNMs is that their number may exceed the number of DOFs, and thus LNMs, of the system. Due to mode bifurcations, not all NNMs can be regarded as extensions of LNMs. An example of NNM bifurcation is given by the system [39]

$$\ddot{x}_1 + k_3(x_1 - x_2)^3 + x_1 + x_1^3 = 0$$
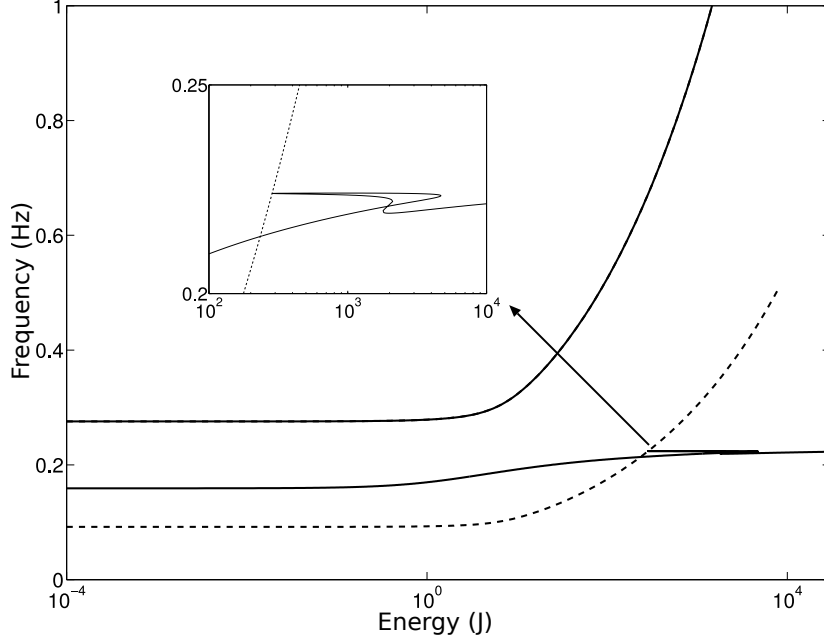$$\ddot{x}_2 - k_3(x_2 - x_2)^3 + x_2 + x_2^3 = 0 \tag{3.1.2}$$

Figure 3.1.3: FEP of the 2dof system (3.1.1). The tongue shows a 3:1 internal resonance between the in-phase and out-of-phase NNMs. - - - -: out-of-phase backbone at one-third of its frequency
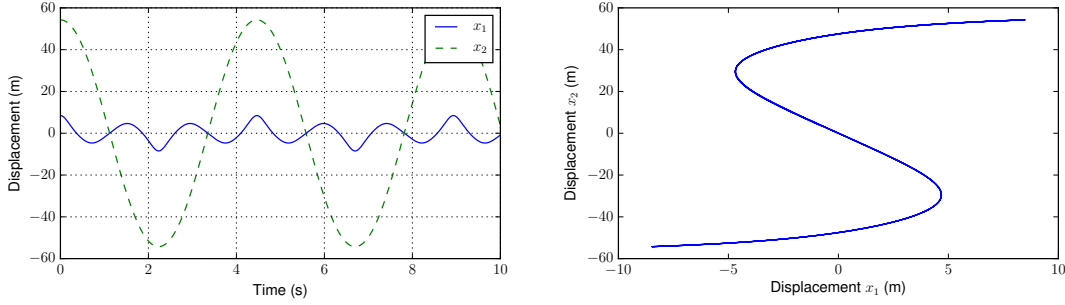

Figure 3.1.4: Internally 3:1 resonant NNMs of the 2dof system (3.1.1). $[x_1, x_2, \dot{x}_1, \dot{x}_2] = [8.476, 54.263, 0, 0]$; **(a)**: time series; **(b)**: configuration space

where k_3 is the strength of the nonlinear coupling. Note that this system is symmetric and thus only possesses *similar* NNMs having the relation $x_2 = cx_1$, where c is a real modal constant.

Insert the relation in eq. 3.1.2 to eliminate x_2

$$\ddot{x}_1 + x_1 + \left(1 + k_3(1-c)^3\right) x_1^3 = 0$$
$$\ddot{x}_1 + x_1 - \frac{1}{c}\left(c^3 + k_3(1-c)^3\right) x_1^3 = 0$$

(3.1.3)

As both equations satisfy the same solution, the modal constant satisfy

$$k_3(1+c)(c-1)^3 = c(1-c^2), \quad c \neq 0$$

(3.1.4)

From this, it follows that the system 3.1.2 always have two modes characterised by $c \pm 1$, the in- and out-of-phase motion respectively, which is a direct extension of LNM.

However there is also the solution

$$c \neq 1, \quad k = -\frac{c}{(c-1)^2} \tag{3.1.5}$$

as shown in fig 3.1.5. At $k_3 = 0.25$ the out-of-phase NNM bifurcates into two additional similar NNMs and become unstable. Unstable NNMs are not physical realisable, as small perturbations of the initial conditions that generate said NNM motion lead to the elimination of the mode oscillation.
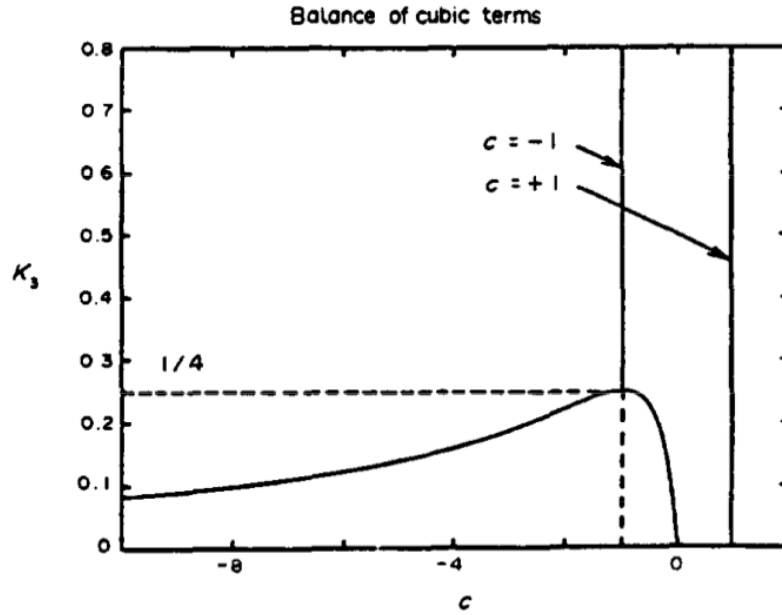

Figure 3.1.5: Pitchfork bifurcation of NMMs; the solution of eq (3.1.4). (—) stable mode, (- - -) unstable mode. Copied from [39]

Figure 3.1.6 shows the time series and corresponding configuration space for the "bifurcated" out-of-phase NNM for (3.1.2). The system still vibrates with a single harmonic in unison, as seen by the straight line in configuration space and the time series; as expected for similar systems.

3.1.2   Summary

NNMs are merely a periodic solution of the eom. Contrary to LNMs, NNMs might become unstable through bifurcations and their numbers might exceed the number of DOFs. Neither are they invariant, as NNMs shows a frequency-energy dependency.

Thus, even if they do not have the mathematical properties of LNMs, ie.NNMs are not orthogonal, cannot decouple eoms and cannot be superposed to calculate the response, they are still useful for understanding some nonlinear phenomenons of lightly damped systems (NNMs are calculated for the underlying Hamiltonian(undamped and unforced) structure)

- Modal interactions, where frequency-energy dependence result in internal resonance.

- Trace the lotus of a nonlinear system for various energies, ie. the resonance.
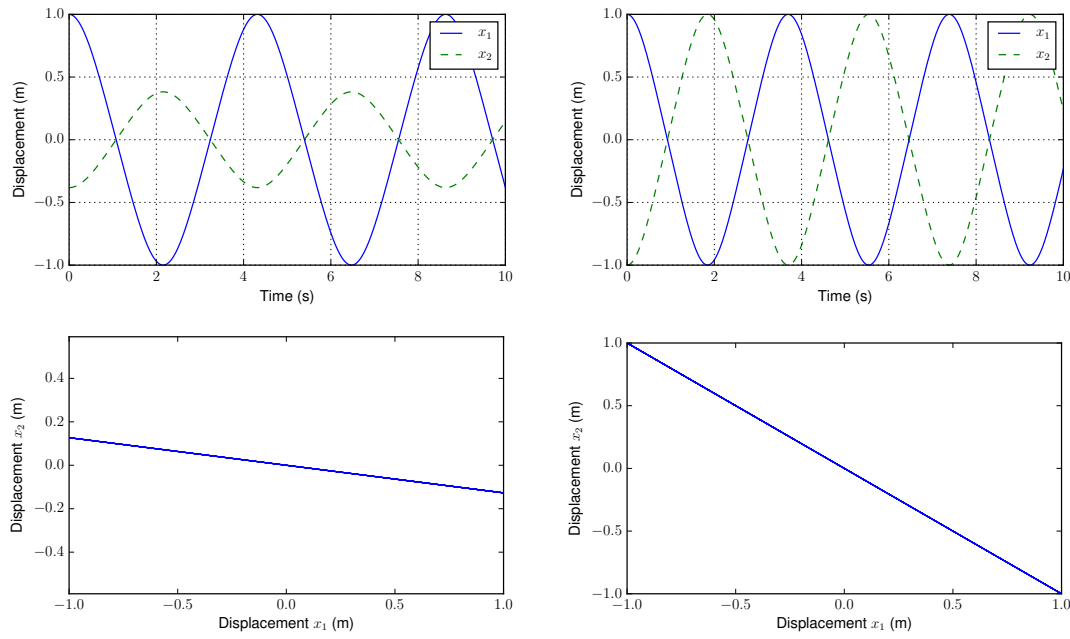
Figure 3.1.6: Time series and corresponding configuration space for the "bifurcated" out-of-phase NNM, system (3.1.2) with $k_3 = 0.2$. **(left)**: $[x_1, x_2, \dot{x}_1, \dot{x}_2] = [1, -1, 0, 0]$; **(right)**: $[x_1, x_2, \dot{x}_1, \dot{x}_2] = [1, -0.3820, 0, 0]$.

3.2 Periodic solution

Before turning to the methods themselves, a few concepts will be revisited. Computing the periodic solution of a nonlinear system means searching for a solution $\mathbf{x}$ to

$$\mathbf{M}\ddot{\mathbf{x}}(t) + \mathbf{C}\dot{\mathbf{x}}(t) + \mathbf{K}\mathbf{x}(t) + \mathbf{f}_{nl}\left(\mathbf{x}(t), \dot{\mathbf{x}}(t)\right) = \mathbf{p}(t) \qquad (3.2.1)$$

that satisfies a periodicity condition

$$\mathbf{x}(t + T) = \mathbf{x}(t) \qquad (3.2.2)$$

where T is the period. This is a boundary value problem(BVP). By periodic solution, steady state conditions are implied. Stability of the periodic solution will also be addressed.

There are at least three ways to describe such a periodic solution.

- Provide initial condition $[\mathbf{x}_0, \dot{\mathbf{x}}_0]$ and the period T. Then do time integration over T.

- Use Fourier series and the period T

- Use piecewise polynomial functions and the period T

In this section methods for finding the first and second representations of a periodic solution is described. They are denoted the shooting method and harmonic balance method respectively. The third and not covered is called Orthogonal collocation. The shooting method is used as part of calculating NNMs and harmonic balance is used for bifurcation analysis. Both methods could be used for either tasks, but as they are popular it is instructive to present both.

3.2.1 Shooting method

With the shooting method one finds, in an iterative way, the initial state $\mathbf{z} = [\mathbf{x}, \dot{\mathbf{x}}]^T$ and period T that describes a periodic motion [28].

One start by guessing on a periodic steady state(ie. initial state and period) and then *shoots* forward one period with the hope of arriving close to the guessed initial state. The difference between the initial and final states is used to correct the initial state, and the method *shoots* forward another period and continue until final and initial state match. The final state is found by time integration, see appendix C for details on the nonlinear Newmark integration. The corrections are done by Newton-Rahpson iterations.

The eom (3.2.1) is recast into state space form. Since this method is used for NNMs, they are recast in undamped and unforced form, ie. the underlaying hamiltonian structure.

$$\dot{\mathbf{z}} = \mathbf{h}_{ham}(\mathbf{z}) = \begin{bmatrix} \dot{\mathbf{x}} \\ -\mathbf{M}^{-1}(\mathbf{K}\mathbf{x} + \mathbf{f}_{nl}) \end{bmatrix} \tag{3.2.3}$$

A solution $\mathbf{z}_p(t; \mathbf{z}_0)$ is a periodic solution of the autonomous system eq. (3.2.3) if $\mathbf{z}_p(t; \mathbf{z}_0) = \mathbf{z}_p(t + T; \mathbf{z}_0)$ where T is the minimal period. Unlike forced motion, the period is not known a priori. The notation is written as $\mathbf{z}(t) = \mathbf{z}(t; \mathbf{z}_0)$ to indicate the dependence on initial conditions $\mathbf{z}(0; \mathbf{z}_0) = \mathbf{z}_0$. From above, the periodic condition is

$$\mathbf{h}(\mathbf{z}_p, T) \equiv \mathbf{z}(T; \mathbf{z}_p) - \mathbf{z}_p = \mathbf{0} \tag{3.2.4}$$

where $\mathbf{h}$ is called the shooting function.

To make the solution $\mathbf{z}(t)$ uniquely defined, the phase must be fixed. If $\mathbf{z}(t)$ is a solution to (3.2.3) then $z(t + \Delta t)$ is geometrically the same solution in state space for any Δt. Ie. the initial condition $\mathbf{z}_0$ can be arbitrarily chosen anywhere on the periodic solution. To prevent this, a phase condition $g(\mathbf{z}_0) = 0$ is set as a additional condition. Most phase conditions imposes one of the unknowns to be set to 0, e.g. the initial displacement or velocity of a DOF(often velocity). See figure 3.2.1 for a illustration of different phases for the periodic solution.

In summary, the periodic solution is found by solving

$$\mathbf{h}_{NNM} = \begin{bmatrix} \mathbf{h}(\mathbf{z}_p, T) \\ g(\mathbf{z}_p) \end{bmatrix} = 0 \tag{3.2.5}$$

The solution is found by corrections to the initial guess, done by Newton-Raphson iterations. The shooting function is expanded in a Taylor series

$$\mathbf{h} + \mathbf{h_z}\Delta\mathbf{z}_p + \mathbf{h}_T\Delta T + H.O.T. = 0 \tag{3.2.6}$$

where all terms are evaluated at (z_0, T) and $H.O.T.$ the neglected higher order terms. Thus the corrections are found by solving the linear equation

$$\begin{bmatrix} \mathbf{h_z} & \mathbf{h}_T \\ g_{\mathbf{z}} & 0 \end{bmatrix} \begin{bmatrix} \Delta\mathbf{z}_p \\ \Delta T \end{bmatrix} = - \begin{bmatrix} \mathbf{h} \\ g \end{bmatrix} \tag{3.2.7}$$
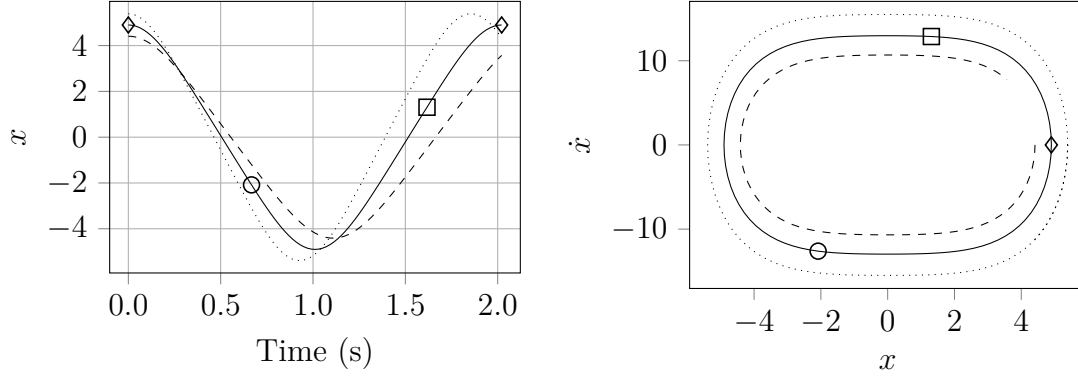
Figure 3.2.1: Solution of the duffing eq. $\ddot{x} + x + 0.5x^3 = 0$ for different initial conditions and $T = 2.0215$s. **(a)**: time series; **(b)**: phase space. Initial conditions for different line styles: ———: [4.9009, 0]; - - - -: 0.9·[4.9009, 0]; ⋯⋯: 1.1·[4.9009, 0]; Markers represent different initial conditions for the periodic solution. ⋄: [4.9009, 0]; □: [1.308, 12.8764]; ○: [-2.0825, -12.6177]

Since $\mathbf{h}_{NNM}$ have the transformation $\mathbb{R}^{2n+1} \to \mathbb{R}^{2n+1}$ the Newton system is over determined, ie. the matrix to invert is not square and have to be solved in a least square sense.

The state is updated as

$$\mathbf{z}_p^{k+1} = \mathbf{z}_p^k + \Delta\mathbf{z}_p^k, \quad T^{k+1} = T^k + \Delta T^k \tag{3.2.8}$$

where k is iteration number. The iteration is stopped when $\mathbf{h}_{nnm} = 0$ to some tolerance. Newmark-Raphson is a local algorithm, meaning that convergence is guarantied when the initial guess is close to solution, otherwise not. The initial guess is chosen as one the of linear mode shapes and corresponding period. If the extended Jacobian matrix $\mathbf{J} = [\mathbf{h_z}, \mathbf{h}_T]$ is exact, the convergence is second order.

The partial derivatives of the shooting function are found as:

$$\mathbf{h_z} = \left.\frac{\partial\mathbf{z}(t;\mathbf{z}_0)}{\partial\mathbf{z}_0}\right|_{t=T} - \mathbf{I} \tag{3.2.9}$$

$$\mathbf{h}_T = \left.\frac{\partial\mathbf{z}(t;\mathbf{z}_0)}{\partial t}\right|_{t=T} = \mathbf{h}_{ham}(\mathbf{z}(T;\mathbf{z}_0)) \tag{3.2.10}$$

where $\mathbf{h}_T$ is a $2n$ vector, $\mathbf{h}_{\mathbf{z}_0}$ is $2n \times 2n$ matrix.

Sensitivity analysis

The Jacobian matrix $\partial\mathbf{z}(t,\mathbf{z}_0)/\partial\mathbf{z}_0$ from eq. (3.2.10), which represent the variation of the solution $\mathbf{z}(t,\mathbf{z}_0)$ at time t to pertubated initial conditions $\mathbf{z}_0$, is normally calculated in two ways. Either by finite difference: successively pertubation of each of the $2n$ initial condtion and integrating over the period. This is computationally expensive and gives slower NR convergence since the Jacobi matrix is only approximate.

Instead sensitivity analysis is used. The state space formulation (3.2.3) is differentiated with respect to initial conditions $\mathbf{z}_0$

$$\frac{\partial}{\partial \mathbf{z}_0} \left[\dot{\mathbf{z}}(t, \mathbf{z}_0) \right] = \frac{\partial}{\partial \mathbf{z}_0} \left[\mathbf{h}_{ham}(\mathbf{z}) \right] \implies$$

$$\frac{\mathrm{d}}{\mathrm{d}t} \left[\frac{\partial \mathbf{z}(t, \mathbf{z}_0)}{\partial \mathbf{z}_0} \right] = \left. \frac{\partial \mathbf{h}_{ham}(\mathbf{z})}{\partial \mathbf{z}} \right|_{\mathbf{z}(t, \mathbf{z}_0)} \frac{\partial \mathbf{z}(t, \mathbf{z}_0)}{\partial \mathbf{z}_0} \tag{3.2.11}$$

with initial condition

$$\frac{\partial \mathbf{z}(0, \mathbf{z}_0)}{\partial \mathbf{z}_0} = \mathbf{I}_{2n} \tag{3.2.12}$$

since $\mathbf{z}(0; \mathbf{z}_0) = \mathbf{z}_0$.

Then eq. (3.2.11) is integrated over T to obtain the Jacobian matrix at time $t = T$. This integration is linear and carried out at the same time as the Newmark integration of the periodic solution. In practise the eom formulation eq. (3.2.1) is used for the sensitivity analysis. See appendix C.2 for a derivation. The sensitivity analysis requires the nonlinear forces to be smooth. If they are nonsmooth, finite difference have to be used.

Marginal stability

For Hamiltonian systems the periodic solutions can at most be marginally stable since the system is without damping. Thus without dissipation, nearby orbits are not attracted to the periodic solution (ie. volume is conserved in phase plane), but the orbit *is* still stable.

The stability of a periodic solution is found from the Jacobian matrix evaluated at $t = T$, called the *monodromy matrix*

$$\Phi = \left. \frac{\partial \mathbf{z}(t; \mathbf{z}_0)}{\partial \mathbf{z}_0} \right|_{t=T} \tag{3.2.13}$$

The stability is found from the eigenvalues σ_i of Φ, the Floquet multipliers. If an Floquet multiplier is larger than one (i.e., $|\sigma_i| > 1$), the orbit is unstable. Conversely, the periodic orbit is stable if $|\sigma_i| \leq 1, \forall i$

Equivalently the Floquet exponents λ could be used. If there is at least one Floquet exponents with a real part larger than 0 the solution is unstable. They are related through,

$$\sigma_i = e^{\lambda_i T} \tag{3.2.14}$$

Both variants are depicted on the complex plane and either compared to the unit circle or the imaginary axis, respectively. See section 3.4, fig 3.4.1 for a graphical representation.

It should be noted that for Hamiltonian systems, for marginally stable solutions, the Floquet multipliers will always be complex conjugate pairs *on* the unit circle, not within as it is the case for asymptotically stable solutions obtained from damped systems. Further there is always one pair of eigenvalues at $(1, 0)$, ie. where the x-axis cross the unit circle in the complex plane. For Floquet exponents this means that the a pair is always located at 0, expressed as $\max(\mathrm{Re}(\lambda)) = 0$. This is due to the monodromy matrix of a Hamiltonian system being *symplectic* [38].

Damped and forced motion

If the shooting method is used for damped and forced motion, only the state space formulation have to be changed.

The state space formulated for the full eom (3.2.1) is

$$\dot{\mathbf{z}}(t) = \mathbf{L}\mathbf{z}(t) - \mathbf{g}_{nl}(\mathbf{z}) + \mathbf{g}_{ext}(\omega, t) \tag{3.2.15}$$

where

$$
\mathbf{z} = \begin{bmatrix} \mathbf{x} \\ \dot{\mathbf{y}} \end{bmatrix}, \quad \mathbf{L} = \begin{bmatrix} \mathbf{0} & \mathbf{I}_n \\ -\mathbf{M}^{-1}\mathbf{K} & -\mathbf{M}^{-1}\mathbf{C} \end{bmatrix}
$$
$$
\mathbf{g}_{nl} = \begin{bmatrix} \mathbf{0} \\ \mathbf{M}^{-1}\mathbf{f}_{nl}(\mathbf{x}, \dot{\mathbf{x}}) \end{bmatrix}, \quad \mathbf{g}_{ext} \begin{bmatrix} \mathbf{0} \\ \mathbf{M}^{-1}\mathbf{p}_{ext}(\omega, t) \end{bmatrix} \tag{3.2.16}
$$

Calculating the periodic motion for the full EOM, instead of the unforced and undamped case, only requires changing the evaluation of the state space to the formula above. The sensitivity analysis in section C.2 is derived for the full EOM. Thus very few lines of code needs changing.

3.2.2 Harmonic balance

Where the shooting method finds a periodic solution by solving the system in time domain, HB finds the periodic solution in frequency domain. The method is described by Detroux, Renson, and Kerschen [10].

A periodic solution to the damped and forced eom eq. (3.2.1) is sought. As the displacements $\mathbf{x}$ and forces $\mathbf{f}(\mathbf{x}, \dot{\mathbf{x}}, \omega, t) = \mathbf{p}(\omega, t) - \mathbf{f}_{nl}(\mathbf{x}, \dot{\mathbf{x}})$ are assumed periodic, they are approximated by Fourier series truncated to the N_H-th harmonic

$$\mathbf{x}(t) = \frac{\mathbf{c}_0^x}{\sqrt{2}} \sum_{k=1}^{N_H} (s_k^x \sin(k\omega t) + c_k^x \cos(k\omega t)) \tag{3.2.17}$$

$$\mathbf{f}(t) = \frac{\mathbf{c}_0^f}{\sqrt{2}} \sum_{k=1}^{N_H} (s_k^f \sin(k\omega t) + c_k^f \cos(k\omega t)) \tag{3.2.18}$$

where $\mathbf{s}_k$ and $\mathbf{c}_k$ represent the vectors of the Fourier coefficients related to sine and cosine terms. The Fourier coefficients of the force $\mathbf{f}(t)$, $\mathbf{s}_k^f$ and $\mathbf{c}_k^f$ depends on the Fourier coefficients of the displacement $\mathbf{x}(t)$, $\mathbf{s}_k^x$ and $\mathbf{c}_k^x$ which are the new unknowns. Gathering the coefficients into vectors

$$\mathbf{z} = \begin{bmatrix} (\mathbf{c}_0^x)^T & (\mathbf{s}_1^x)^T & (\mathbf{c}_1^x)^T & \cdots & (\mathbf{s}_{N_H}^x)^T & (\mathbf{c}_{N_H}^x)^T \end{bmatrix}^T \tag{3.2.19}$$

$$\mathbf{b} = \begin{bmatrix} (\mathbf{c}_0^f)^T & (\mathbf{s}_1^f)^T & (\mathbf{c}_1^f)^T & \cdots & (\mathbf{s}_{N_H}^f)^T & (\mathbf{c}_{N_H}^f)^T \end{bmatrix}^T \tag{3.2.20}$$

then using a compact notion, the displacements and forces is written as

$$\mathbf{x}(t) = (\mathbf{Q}(t) \otimes \mathbf{I}_n)\mathbf{z} \tag{3.2.21}$$

$$\mathbf{f}(t) = (\mathbf{Q}(t) \otimes \mathbf{I}_n)\mathbf{b} \tag{3.2.22}$$

where $\otimes$ is the Kronecker product and $\mathbf{Q}$ a vector with harmonic terms

$$\mathbf{Q}(t) = \begin{bmatrix} \frac{1}{2} & \sin(\omega t) & \cos(\omega t) & \cdots & \sin(N_H \omega t) & \cos(N_H \omega t) \end{bmatrix} \tag{3.2.23}$$

Velocities and accelerations are found using the Fourier series as

$$\dot{\mathbf{x}} = \left(\dot{\mathbf{Q}}(t) \otimes \mathbf{I}_n \right) \mathbf{z} = \left((\mathbf{Q}(t)\boldsymbol{\nabla}) \otimes \mathbf{I}_n \right) \mathbf{z} \tag{3.2.24}$$

$$\ddot{\mathbf{x}} = \left(\ddot{\mathbf{Q}}(t) \otimes \mathbf{I}_n \right) \mathbf{z} = \left((\mathbf{Q}(t)\boldsymbol{\nabla}^2) \otimes \mathbf{I}_n \right) \mathbf{z} \tag{3.2.25}$$

$$\tag{3.2.26}$$

By substituting eqs. (3.2.17)-(3.2.18) and (3.2.24)-(3.2.25) into the eom (3.2.1) and using a galerkin procedure, one ends up with the equations of motion in frequency domain (see appendix B.1 for more details on the derivation and definition of $\boldsymbol{\nabla}$(the gradient as diagonal matrix))

$$(\boldsymbol{\nabla}^2 \otimes \mathbf{M})\mathbf{z} + (\boldsymbol{\nabla} \otimes \mathbf{C})\mathbf{z} + (\mathbf{I}_{2N_H} \otimes \mathbf{K})\mathbf{z} = (\mathbf{I}_{2N_H} \otimes \mathbf{I}_n)\mathbf{b} \tag{3.2.27}$$

or in more compact form

$$\mathbf{h}(\mathbf{z}, \omega) = \mathbf{A}(\omega)\mathbf{z} - \mathbf{b}(\mathbf{z}) = \mathbf{0} \tag{3.2.28}$$

where $\mathbf{A}$ describes the linear dynamics

$$\mathbf{A} = \boldsymbol{\nabla}^2 \otimes \mathbf{M} + \boldsymbol{\nabla} \otimes \mathbf{C} + \mathbf{I}_{2N_H} \otimes \mathbf{K} \tag{3.2.29}$$

If $\mathbf{z}$ is a solution of (3.2.28), then the time signal $\mathbf{x}$ constructed from $\mathbf{z}$ is periodic and satisfies the eom (3.2.1). As with the shooting function, eq. (3.2.28) is nonlinear (due to $\mathbf{b}$ dependence on $\mathbf{z}$) and have to be solved iterative by Newton-Rahpson iterations. It should however be noted that $\mathbf{h}(\mathbf{z}, \omega)$ is an (nonlinear) algebraic equation, ie. there is no need for time integration. The increments are found as

$$\mathbf{z}^{(k+1)} = \mathbf{z}^{(j)} - \frac{\mathbf{h}(\mathbf{z}, \omega)}{\mathbf{h_z}(\mathbf{z}, \omega)} \tag{3.2.30}$$

Expression of nonlinear terms and Jacobian matrix

Solution of eq (3.2.30) requires calculation of $\mathbf{h}$ and of the Jacobian matrix $\mathbf{h_z}$, which in turn requires calculation of $\mathbf{b}$ and its derivatives.

It is not known how the Fourier coefficients in $\mathbf{b}$ relates to the coefficients in $\mathbf{z}$, ie. it is not possible to directly calculate $\mathbf{b}(\mathbf{z})$ due to $\mathbf{f}_{nl}$ depends on $\mathbf{x}$. Instead a technique called the *alternating frequency-time domain*(AFT) method is used. Here $\mathbf{b}$ is calculated through successive Fourier transformations as shown in figure 3.2.2
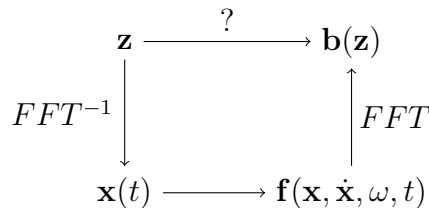
Figure 3.2.2: Graphical representation of the alternating frequency-time domain (AFT) method

$\mathbf{x}$ is calculated from the Fourier coefficients in $\mathbf{z}$, then the nonlinear (and external) forces $\mathbf{f}$ are evaluated in time domain and $\mathbf{b}$ is found as the Fourier coefficients of $\mathbf{f}$.

The Jacobian matrix is given by

$$\mathbf{h_z} = \frac{\partial \mathbf{h}}{\partial \mathbf{z}} = \mathbf{A} - \frac{\partial \mathbf{b}}{\partial \mathbf{z}} \tag{3.2.31}$$

where the hard part is to compute $\mathbf{b_z}$. The method for calculating the Jacobian matrix (explicit $\mathbf{b_z}$) follows the AFT method as well. To do that, the inverse Fourier transform is written as the linear operator $\mathbf{\Gamma}(\omega)$

$$\mathbf{\Gamma}(\omega) = \left[\mathbf{I}_n \otimes \begin{bmatrix} 1/\sqrt{2} \\ 1/\sqrt{2} \\ \vdots \\ 1/\sqrt{2} \end{bmatrix} \quad \mathbf{I}_n \otimes \begin{bmatrix} \sin(\omega t_1) \\ \sin(\omega t_2) \\ \vdots \\ \sin(\omega t_{t_N}) \end{bmatrix} \quad \mathbf{I}_n \otimes \begin{bmatrix} \cos(\omega t_1) \\ \cos(\omega t_2) \\ \vdots \\ \cos(\omega t_{t_N}) \end{bmatrix} \quad \cdots \right.$$
$$\left. \mathbf{I}_n \otimes \begin{bmatrix} \sin(N_H \omega t) \\ \sin(N_H \omega t_2) \\ \vdots \\ \sin(N_H \omega t_{t_N}) \end{bmatrix} \quad \mathbf{I}_n \otimes \begin{bmatrix} \cos(N_H \omega t) \\ \cos(N_H \omega t_2) \\ \vdots \\ \cos(N_H \omega t_{t_N}) \end{bmatrix} \right] \tag{3.2.32}$$

which is used on the concatenated time series

$$\begin{aligned} \tilde{\mathbf{x}} &= \begin{bmatrix} x_1(t_1) & \cdots & x_1(t_N) & \cdots & x_n(t_1) & \cdots & x_n(t_N) \end{bmatrix}^T \\ \tilde{\mathbf{f}} &= \begin{bmatrix} f_1(t_1) & \cdots & f_1(t_N) & \cdots & f_n(t_1) & \cdots & f_n(t_N) \end{bmatrix}^T \end{aligned} \tag{3.2.33}$$

Thus the inverse and direct Fourier transform are written

$$\tilde{\mathbf{x}} = \mathbf{\Gamma}(\omega)\mathbf{z}, \quad \mathbf{z} = (\mathbf{\Gamma}(\omega))^+ \tilde{\mathbf{x}} \tag{3.2.34}$$

where $()^+$ is the Moore-Penrose pseduinverse and used as Γ is not square. In implementation the solution is found by a least square solver.

The Fourier coefficients of the external and nonlinear forces are then

$$\mathbf{b}(\mathbf{z}) = (\mathbf{\Gamma}(\omega))^+ \tilde{\mathbf{f}} \tag{3.2.35}$$

and the Jacobian is computed as

$$\mathbf{h_z} = \mathbf{A} - \frac{\partial \mathbf{b}}{\partial \mathbf{z}} = \mathbf{A} - \frac{\partial \mathbf{b}}{\partial \tilde{\mathbf{f}}} \frac{\partial \tilde{\mathbf{f}}}{\partial \tilde{\mathbf{x}}} \frac{\partial \tilde{\mathbf{x}}}{\partial \mathbf{z}} = \mathbf{A} - \mathbf{\Gamma}^+ \frac{\partial \tilde{\mathbf{f}}}{\partial \tilde{\mathbf{x}}} \mathbf{\Gamma} \tag{3.2.36}$$

It should be noted that the concatenated time series vectors $\tilde{\mathbf{x}}$ and $\tilde{\mathbf{f}}$ are newer used. They are only used in the derivation for the expression for the Jacobian. Only the Fourier operator $\mathbf{\Gamma}$ and extracted Fourier coefficients $\mathbf{x}$ are used.

Stability

Unlike the shooting method (or general time domain methods), the monodromy matrix is not readily available as a byproduct since there is no time integration. Instead for frequency methods, *Hills method* is used to approximate the Floquet exponents by solving a quadratic eigenvalue problem whose components are obtained as byproduct of the HB method.

Perturbing a periodic solution by an exponential decay

$$\mathbf{p}(t) = \mathbf{x}(t) + e^{\lambda t}\mathbf{s}(t) \tag{3.2.37}$$

and inserting this into the eom eq. (3.2.1) it is shown in appendix A.1.1 that the quadratic eigenvalue problem is found as

$$\boldsymbol{\Delta}_2\boldsymbol{\lambda}^2 + \boldsymbol{\Delta}_1\boldsymbol{\lambda} + \mathbf{h_z} = \mathbf{0} \tag{3.2.38}$$

where $\boldsymbol{\Delta}$ are matrices describing the linear dynamics similar to $\mathbf{A}$ in eq. (A.1.10) and λ are Hills coefficients.

The quadratic eigenvalue problem is rewritten to a linear eigenvalue problem of double size

$$\mathbf{B}_1 - \gamma\mathbf{B}_2 = \mathbf{0} \tag{3.2.39}$$

where

$$\mathbf{B}_1 = \begin{bmatrix} \boldsymbol{\Delta} & \mathbf{h_z} \\ -\mathbf{I} & \mathbf{0} \end{bmatrix}, \quad \mathbf{B}_2 = -\begin{bmatrix} \boldsymbol{\Delta}_2 & \mathbf{0} \\ \mathbf{0} & \mathbf{I} \end{bmatrix} \tag{3.2.40}$$

The coefficients $\boldsymbol{\lambda}$ are found as the eigenvalues of the $(2N_H + 1)2n$ square matrix

$$\mathbf{B} = \mathbf{B}_2^{-1}\mathbf{B}_1 = \begin{bmatrix} -\boldsymbol{\Delta}_2^{-1}\boldsymbol{\Delta}_1 & -\boldsymbol{\Delta}_2^{-1}\mathbf{h_z} \\ \mathbf{I} & \mathbf{0} \end{bmatrix} \tag{3.2.41}$$

or from the generalised eigenvalueproblem eq. (3.2.39)

Only $2n$ eigenvalues approximate the Floquet exponents $\tilde{\boldsymbol{\lambda}}$, the rest are spurious. The ones needed are the $2n$ values with smallest imaginary magnitude.

The diagonal matrix

$$\tilde{\mathbf{B}} = \begin{bmatrix} \tilde{\lambda}_1 & & \\ & \ddots & \\ & & \tilde{\lambda}_{2n} \end{bmatrix} \tag{3.2.42}$$

gathers the Floquet exponents identified from the $(2N_H + 1)2n$ Hill's coefficients. Besides stability, they are used for detecting bifurcations in section 3.5.

Example

Figure 3.2.3 shows the periodic of the coupled duffing Duffing system. Although the excitation is pure sine, the response contains multiple harmonics due to the nonlinearity. As the fifth harmonic only participates marginally, it can be assumed that even higher harmonics are not important for describing the periodic motion. The number

of harmonic participating, and their weights, depends on the forcing frequency and the level of nonlinearity(ie. including the forcing level).

The normalised harmonic components are found as

$$\sigma_i = \frac{\phi_i}{\sum_{k=0}^{N_H} \phi_i}, \quad (i = 0, \cdots, N_H)$$
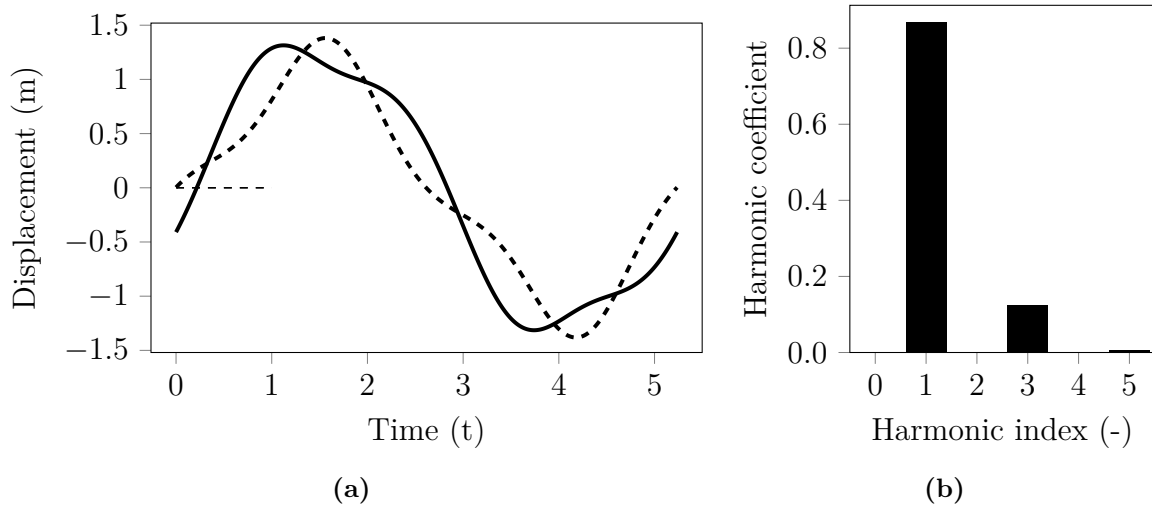$$\phi_0 = \frac{c_0^x}{\sqrt{2}}, \quad \phi_i = \sqrt{(s_i^x) + (c_i^x)^2} \qquad (3.2.43)$$

Figure 3.2.3: Periodic solution of the coupled Duffing system (1.5.1) for $f = 2$N, $\omega = 1.2$rad/s and $N_H = 5$. **(a):** Time series. ——: x_1, - - - -: x_2; **(b):** Normalized harmonic components of x_1.

3.2.3 Summary

Periodic solutions of nonlinear structures can be computed with time-domain(shooting method) and frequency-domain(harmonic balance) methods. The main difference is in the implementation complexity, compution complexity and accuracy. Both methods can be used together with continuation and have ways to compute stability analysis without much extra cost.

Summarising the shooting method

Pro | Cons

- Accurate
- (all) Higher harmonics represented

- Many time integrations
- Slow for larger systems

Summarising the harmonic balance method

Pro

- Fast

- Harmonic coefficients available
- Can be used for filtering, ie. by defining the number of harmonics in

the solution.   Cons

- Less accurate

- High number of harmonic might be necessary. Need to check the contribution from last harmonics to ensure enough is included.

Stability of a periodic solution can be assessed through their Floquet multipliers or exponents. When the Shooting method is used, they are found from the monodromy matrix. When HB is used, they are found from Hills matrix.

3.3   Continuation

When the periodic solution is found, finding the successively periodic solutions for slightly changed parameter values is done by continuation.

A general continuation is formulated as $F(x) = 0$, $F : \mathbb{R}^{m+1} \to \mathbb{R}^m$ where is F the algebraic problem for which a solution is sought. For HB, F correspond to $\mathbf{h} \in \mathbb{R}^{(2N_H+1)n}$ which depends on $\mathbf{z} \in \mathbb{R}^{(2N_H+1)n}$ and $\omega \in \mathbb{R}^1$; following the continuation structure. However, as already mentioned, for the shooting method: $\mathbf{h}_{NMM} \in \mathbb{R}^{2n+1}$ which depends on $\mathbf{z} \in \mathbb{R}^{2n}$ and $T \in \mathbb{R}^1$; thus not following the structure. The difference is that with HB, continuation can be done by solving a linear system using a direct solver, whereas the system is over determined for the shooting method and a least square solver is needed. It is possible to recast $\mathbf{h}_{NNM}$ into a square problem by adding a artificial parameter into the Hamiltonian, which during the continuation anyways turns out to be zero[9]. The reason for doing this is that direct solution is computional faster than iterative solvers. Note that ω and T are used interchangeable in this section, ie. by $\mathbf{h}_\omega$ is understood $\mathbf{h}_T$ for the shooting method etc..

The most simple continuation method, where ω is used as independent parameter and uniformly increased at each step, fails at turning points. Instead most continuation methods uses a length-wise curve parameter and a predictor-corrector model. Starting from a known solution $\mathbf{y}_j = [\mathbf{z}_{p,(j)}, \omega_{(j)}]^T$ the next periodic solution $\mathbf{y}_{j+1}$ is found by the three steps

- Tangent prediction, $\mathbf{y}_{(j+1)}^{(1)} = \mathbf{y}_{(j)} + s\mathbf{t}_{(i)}$, where s is the step size and $\mathbf{t}$ the tangent of $\mathbf{y}$, ie. the tangent of $\mathbf{z}_p$ and ω.

- Newton-like corrections - The type determines the continuation method.

- Adaptive step control. Here a simple model using the convergence of the Newton iterations is used: $s = \frac{it_{opt}}{it_{NR}}s$, ie. the step is updated based on a defined optimal number of iterations versus the actual used number of iteration

The two methods used in this project are the pseudo-archlength- and the Moore-Penrose continuation. The main difference is computional complexity. With pseudo-archlength, each time a new point is found on the curve, the tangent vector have

to be computed anew. With the Moore-penrose corrector, the tangent vector is also corrected and the explicit calculation of the tangent at each new point is saved.

The aim is to show that is no harder to use the Moore-penrose corrector. Formal descriptions are found in [11]

3.3.1 Procedure

The tangent at a solution point $\mathbf{y}_i$ is

$$\begin{bmatrix} \mathbf{J}(\mathbf{y}_{(i)}) \\ \mathbf{t}_{(i-1)}^T \end{bmatrix} \mathbf{t}_i = \begin{bmatrix} \mathbf{0} \\ 1 \end{bmatrix} \tag{3.3.1}$$

where

$$\mathbf{J}(\mathbf{y}_{(i)}) = \begin{bmatrix} \mathbf{h}_\mathbf{z}(\mathbf{y}_{(i)}) & \mathbf{h}_\omega(\mathbf{y}_{(i)}) \end{bmatrix} \tag{3.3.2}$$

The last row in eq. (3.3.1) prevents the continuation from turning back, ie. $\mathbf{t}_{(i-1)}^T \mathbf{t}_{(i)} = 1$ and the "angle of the dot product" cannot change sign. For the first tangent calculation the condition is replaced by a row of ones, which impose the length of the tangent to 1; in later predictions $\mathbf{t}_{(i+1)}$ must be normalized. The prediction is then

$$\mathbf{y}_{(i+1)}^{(1)} = \mathbf{y}_{(i+1)} + s\mathbf{t}_i \tag{3.3.3}$$

The correction types Pseudo-archlength and Moore-penrose are used with the shooting method and harmonic balance, respectively. Convergence is achieved when

$$\frac{\|\mathbf{h}\|}{\|\mathbf{z}\|} < tol \tag{3.3.4}$$

Shooting methods

For the pseudo-archlength corrections, a solution is sought in the perpendicular direction of the prediction. The corrections are given by

$$\mathbf{y}^{(j+1)} = \mathbf{y}^{(j)} + \Delta\mathbf{y} = \mathbf{y}^{(j)} - \mathbf{G}_\mathbf{y}^{-1}\mathbf{G} \tag{3.3.5}$$

where the prediction subscripts have been omitted. We have

$$\mathbf{G}(\mathbf{y}) = \begin{bmatrix} \mathbf{h}_{NNM}(\mathbf{y}) \\ \mathbf{0} \end{bmatrix}, \quad \mathbf{G}_\mathbf{y}(\mathbf{y}) = \begin{bmatrix} \mathbf{J}(\mathbf{y}) \\ \mathbf{t}^T \end{bmatrix} \tag{3.3.6}$$

where correction superscripts have been omitted. After convergence to a solution, the tangent is calculated and the algorithm continues.

The phase condition $g(\mathbf{z})$, as seen in eq. (3.2.7), should formally be included in eqs. (3.3.1)-(3.3.6), ie. in the predictions one adds the equation $\begin{bmatrix} g_\mathbf{z} & 0 \end{bmatrix} \mathbf{t}_i = 0$ and in the corrections $\begin{bmatrix} g_\mathbf{z} & 0 \end{bmatrix} \mathbf{t}_i = -g(\mathbf{z})$. But instead of adding conditions, it is used that NNMs for all practical circumstances are symmetric, the loss of symmetry requires a symmetry breaking bifurcation [35], ie. the initial velocity is zero for all dofs. Thus the velocities can be removed from the unknowns and the system to solve then have $2n + 1$ equations with $n + 1$ unknowns.

Harmonic balance

For the Moore-penrose corrections, the nearest solution to the prediction is sought. This is done by updating the tangent direction at each corrector iteration.

Using a optimisation variable $\mathbf{v}$, initialised as the prediction tangent $\mathbf{v}^{(1)} = \mathbf{t}_{(i)}$, the Moore-penrose corrections are given by

$$\begin{aligned}
\mathbf{y}^{(j+1)} &= \mathbf{y}^{(j)} + \Delta\mathbf{y} = \mathbf{y}^{(j)} - \mathbf{G}_{\mathbf{y}}^{-1}\mathbf{G} \\
\mathbf{v}^{(j+1)} &= \mathbf{v}^{(j)} + \Delta\mathbf{y} = \mathbf{v}^{(j)} - \mathbf{G}_{\mathbf{y}}^{-1}\mathbf{R}
\end{aligned} \tag{3.3.7}$$

where the prediction subscripts have been omitted. We have

$$\mathbf{G}(\mathbf{y}, \mathbf{v}) = \begin{bmatrix} \mathbf{h}(\mathbf{y}) \\ 0 \end{bmatrix}, \quad \mathbf{G}_{\mathbf{y}}(\mathbf{y}, \mathbf{v}) = \begin{bmatrix} \mathbf{J}(\mathbf{y}) \\ \mathbf{v}^T \end{bmatrix}$$

$$\mathbf{R}(\mathbf{y}, \mathbf{v}) = \begin{bmatrix} \mathbf{J}(\mathbf{y})\mathbf{v} \\ 0 \end{bmatrix} \tag{3.3.8}$$

where correction superscripts have been omitted.

When convergence is reached the tangent is calculated as the normalized correction of $\mathbf{v}$, $\mathbf{t}_{(j+1)} = \frac{\mathbf{v}}{\|\mathbf{v}\|}$.

During the corrections eq. (3.3.7-3.3.8) $\mathbf{h}_{\mathbf{z}}$ is calculated, making stability analysis with Hills method cheap after each solution is obtained.

As a final note, $\mathbf{h}_{\omega}$ in the jacobian eq. (3.3.2) is given by

$$\mathbf{h}_{\omega} = \frac{\partial \mathbf{A}}{\partial \omega}\mathbf{z} \tag{3.3.9}$$

3.3.2   Example

NNM

Figure 3.3.1 shows the two NNMs, the in-phase and out-of-phase, for the coupled duffing system (1.5.1) in a frequency-energy plot(FEP). The evolution of natural frequencies are seen wrt. to the total energy of the system. At low energy the NNM frequencies are close to the linear frequencies, but as energy increases, the natural frequency increases due to the cubic nonlinear hardening. As the energy increases, the two NNMs coincide and it is not possible to obtain commensurate ratio between the two natural frequencies. Thus there is no internal resonance.

The insert shows the configuration space, and it seen that both branches of NNMs have straight modal lines, which is due to the symmetry of the system: due to the symmetry there are only similar NNMs.

HB

Figure 3.3.2 shows the NRFC for the coupled duffing using five harmonic terms, which is enough to capture the harmonic components as seen in figure 3.2.3. If a lower number of harmonic were included - only one and three terms would be relevant since even harmonics are zero; it would required an even nonlinearity to generate even harmonics - the superharmonic resonances at lower frequencies will not be captured. See appendix B.1 where NRFCs are shown for different HB and continuation parameters.
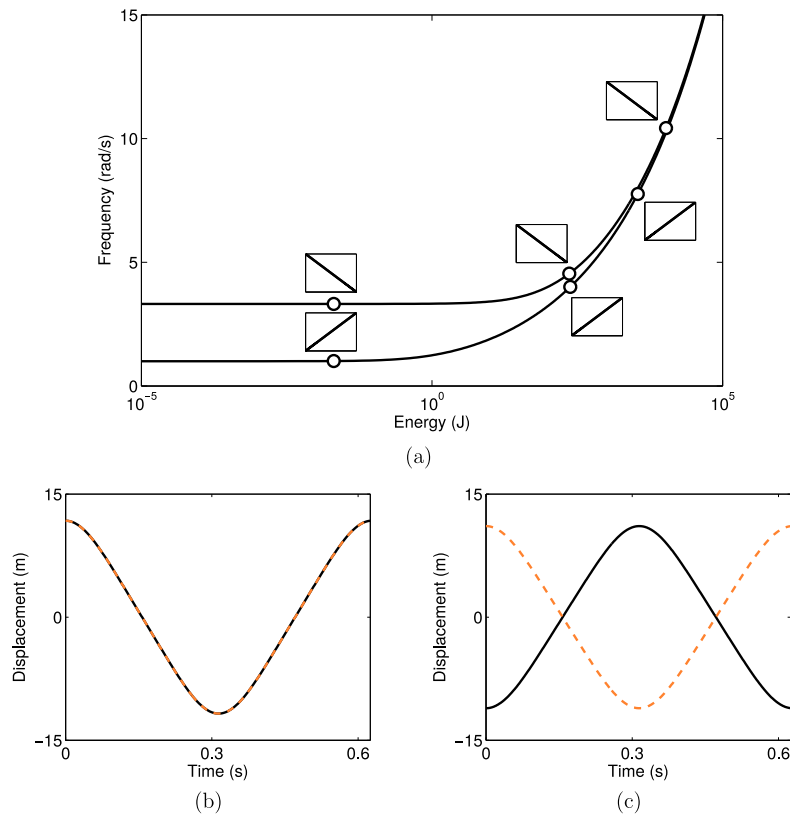
Figure 3.3.1: NNMs for the coupled duffing system (1.5.1). **(a)**: Frequency-energy plot(FEP). NNM motion(configuration space, ie. x_1 vs. x_1) at given frequencies are shown in inserts; **(b)**: in-phase NNM at $\omega = 10$rad/s; **(c)**: out-of-phase NNM at $\omega = 10$rad/s; ——: x_1; - - - -: x_2.

3.3.3 Summary

Figure 3.3.3 show an algorithm for the continuation procedure, regardless of the the correction method. There is not much difference if implementation complexity of the two corrections, but the Moore-penrose corrections saves on computional complexity. The Pseudo-arclength method can be seen as a Moore-Penrose method for which the correction direction is not updated.

3.4 Bifurcations

When stability of a periodic solution changes, it occurs at *bifurcation points* in parameter space. At bifurcation points, the solution changes qualitatively, but knowledge of the bifurcation type allows to predict the behaviour. The type of bifurcation is related to how the Floquet multipliers changes at said point, and the mechanism for loss of stability for the three most common types are shown in figure 3.4.1.

Bifurcations exist for multiple dimensions, but only codimension-1 bifurcations are treated as only one parameter varies along the branch (ie. the forcing frequency ω). Bifurcations are a feature of nonlinear systems. Further description is found in Juel
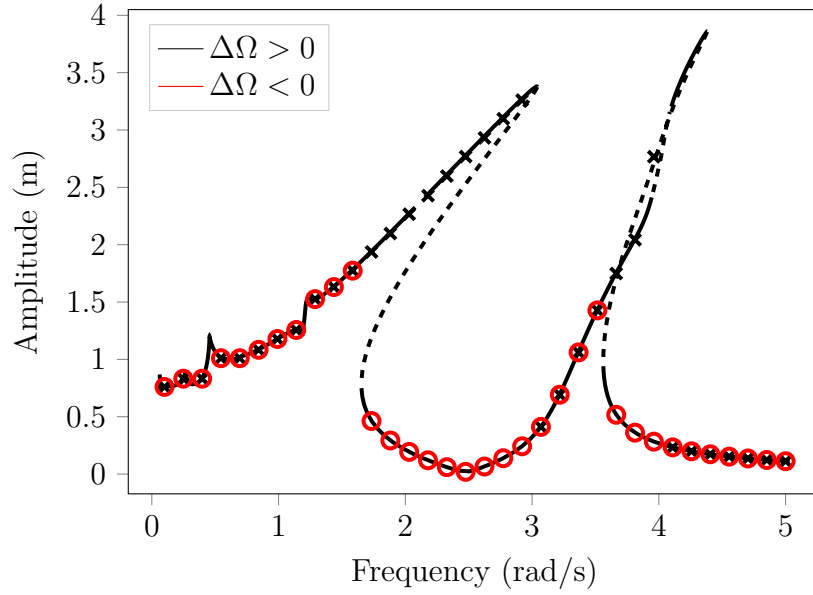
Figure 3.3.2: NRFC of the coupled duffing system (1.5.1) for x_1 with $f = 2$N. Unstable motion are indicated by $---$. $N_H = 5, N = 512$. Markers indicate amplitudes for a stepped sine. $\times$: increasing; $\circ$: decreasing.

Thomsen [17] or dedicated bifurcation textbooks like Kuznetsov [23]. Floquet multipliers σ_i and Floquet exponents λ_i are related as (as restated from eq. (3.2.14))

$$\sigma_i = e^{\lambda_i T} \tag{3.4.1}$$

3.4.1 Fold and branch bifurcation Point

At fold point bifurcation point the state undergoes amplitude jumps and at branch point bifurcation, branching, see below. These two types are detected when a Floquet multiplier leaves the unit circle along the real axis through $+1$ or, equivalently, when a Floquet exponent crosses the imaginary axis through 0, see figs 3.4.1(a,b)

At this point, the Jacobian matrix $\mathbf{h_z}$ is singular: if $\mathbf{h_z}$ is singular then the monodromy matrix $\mathbf{\Phi}$ of the Shooting method or $\tilde{\mathbf{B}}$ of HB, eq (3.2.41), is also singular and at least one Floquet exponent is 0 (or a Floquet multiplier crosses the unit circle through $+1$)

- *Fold bifurcation* (also called Saddle node, Limit point or Turning point):
  The branch comes from one side and turns back, ie. the parameter(ω) increases and then decreases or decreases and then increases. Thus fold bifurcation indicates that there exist two solutions in its vicinity. It determines the upper or lower region of a bistable region and is often present in the vicinity of resonance peaks. This is the cause of amplitude jumps seen as response to stepped- or swept-sine excitation.

- *Branch bifurcation(BP)*:
  Two branches are connected. The two branches either meet and exchange stabil-
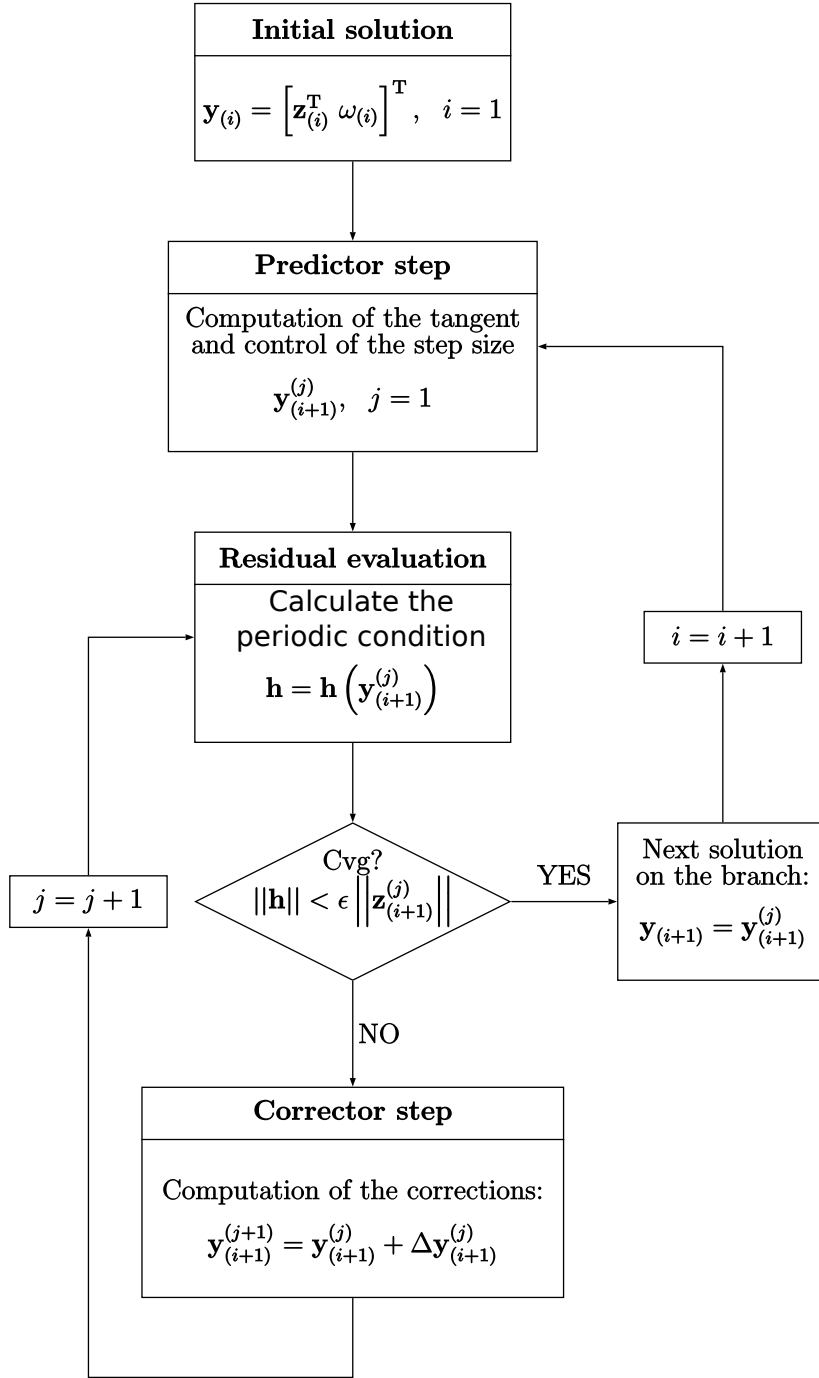
Figure 3.3.3: Algorithm for Predictor-Corrector continuation of a periodic solution. For Moore-penrose the successive tangents are simply calculated as a normalization.

ity (transcritical bifurcation), or one branch loses stability and a stable branch emanates from the point (pitchfork bifurcation).

Fold bifurcations satisfies

$$\mathbf{h}_\omega \notin \text{range}(\mathbf{h_z}) \tag{3.4.2}$$

whereas for BP

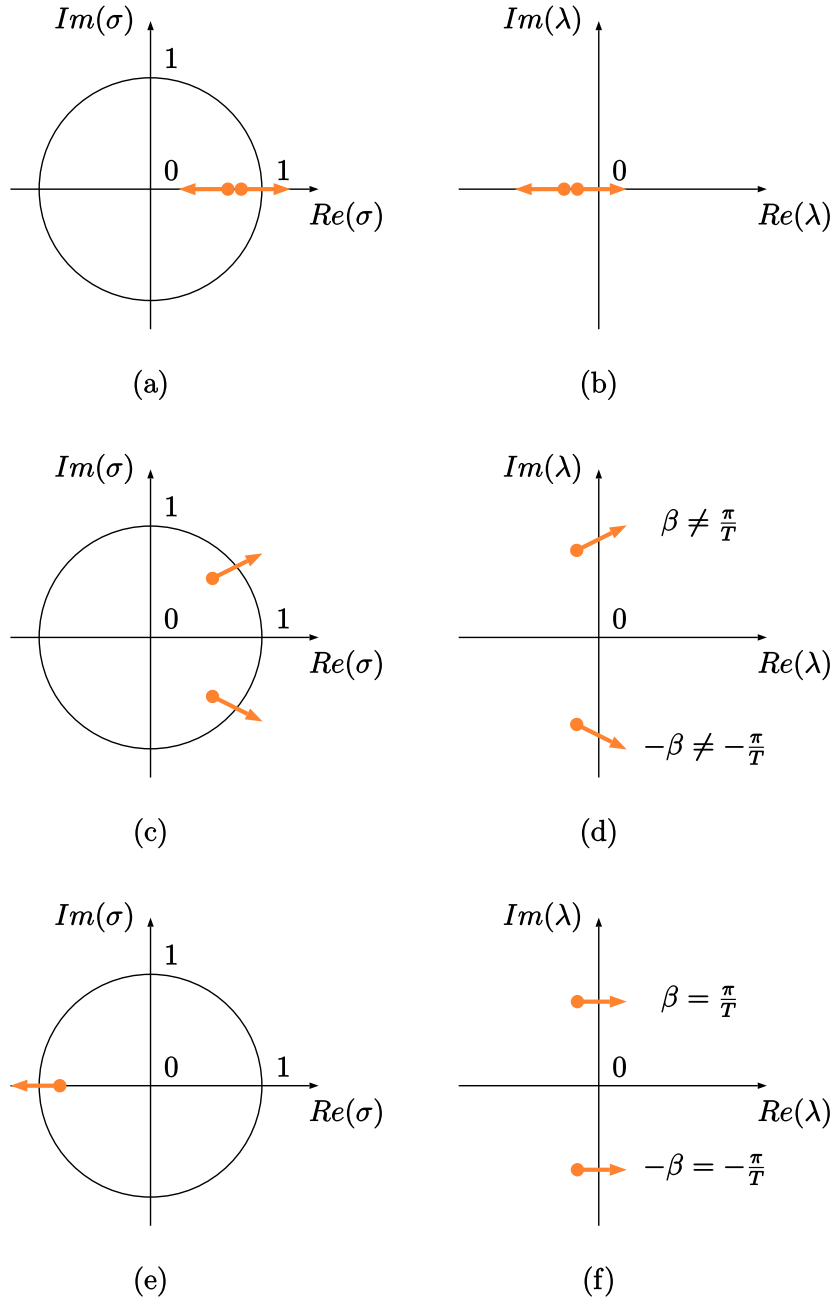$$\mathbf{h}_\omega \in \text{range}(\mathbf{h_z}) \tag{3.4.3}$$

Figure 3.4.1: Mechanisms for the loss of stability of a periodic solution, illustrated with Floquet multipliers (left column) and Floquet exponents (right column). **First row**: singular point; **Second row**: Neimark-Sacker bifurcation; **third row**: period doubling bifurcation. Reproduced from [9]

It follows that fold and BPs can be found, and distinguished, by calculating the rank of the extended Jacobian $\mathbf{J} = [\mathbf{h_z}|\mathbf{h}_\omega]$ and $\mathbf{h_z}$. If the rank of $\mathbf{J}$ is equal to $\mathbf{h_z}$(and $\mathbf{h_z}$ is singular) then it is a BP, otherwise fold.

If a BP is found, some branch switching mechanism should be used in the continuation in order to switch branch. If no switching mechanism is used, the continuation most likely continues on the same branch through the BP. The new branch is found by calculating the two tangent directions at the BP; thus some adoption of the predictor method is needed.

3.4.2   Neimark-Sacker bifurcation

A Neimark-Sacker(NS) bifurcation (also called Hopf- or torus bifurcation) is detected when a pair of Floquet multipliers leaves the unit circle as complex conjugates or, equivalently, when a pair of Floquet exponent crosses the imaginary axis as complex conjugates through any value but $\pm\frac{i\pi}{T}$, where T is the period of oscillation, see figs 3.4.1(c,d).

At NS a new type of oscillations emerges. These are called quasiperiodic oscillations(QP) and despite the name they are not periodic. QPs contain the forcing frequency ω (forcing), and at least another frequency ω_2(envelope). The two frequencies are incommensurate, ie. $\frac{\omega}{\omega_2}$ is irrational. QP should not be confused with linear beating, where the forcing frequency is close to the eigenfrequency ω_0, ie. $|\omega_0 - \omega|$ is small.

The imaginary part of the Floquet exponents that crosses the imaginary axis, β, approximates the envelope pulsation ω_2 of the QP in the vicinity of the bifurcation, see fig. 3.4.1(d)

3.4.3   Period doubling bifurcation

A period doubling(PD) (also called flip bifurcation) is detected when a pair of Floquet multipliers leaves the unit circle along the real axis through -1 or, equivalently, when a pair of Floquet exponent crosses the imaginary axis as complex conjugates through $\pm\frac{i\pi}{T}$, see figs. 3.4.1(e,f).

At PD a new branch of solution appears. The new branch have stable periodic solutions with a doubled period. When they appear in cascade, PDs can lead to chaos.

3.5   Detecting bifurcations

To detect bifurcations during the continuation procedure, *test functions* ϕ are monitored. When they change sign, a bifurcation is detected. Each type of bifurcation have their own test function

3.5.1   Fold and branch bifurcation Point

As stated, fold and BP are characterised by rank deficiency of the Jacobian matrix $\mathbf{h_z}$. Thus a test function could be

$$\phi_{F,BP} = \det \mathbf{h_z} \tag{3.5.1}$$

a computationally cheaper detection could be based on the monodromy or Hills matrix, since this is already available

$$\phi_{F,BP} = \det \tilde{\mathbf{B}} \tag{3.5.2}$$

To distinguish between fold and BP, a dedicated test function is

$$\phi_{BP} = \det \begin{pmatrix} \mathbf{h_z} & \mathbf{h}_\omega \\ & \mathbf{t}^T \end{pmatrix} \tag{3.5.3}$$

For detection fold bifurcation alone, a computationally cheaper way is to use the geometric folding of the branch, ie. detect when the ω component of the tangent prediction $\mathbf{t}$ changes sign,

$$\phi_F = t_\omega \tag{3.5.4}$$

3.5.2 Neimark-Sacker and period doubling bifurcation

NS and PD bifurcations, where a pair of Floquet exponents crosses the imaginary axis as complex conjugates, can be detected using the *bialternate product of a matrix* [23]. The bialternate product $\mathbf{P}_\odot$ of a $m \times m$ matrix $\mathbf{P}$ is

$$\mathbf{P}_\odot = 2\mathbf{P} \odot I_m \tag{3.5.5}$$

with dimensions $m(m-1)/2$, is singular when two of its eigenvalues, $\mu 1$ and $\mu 2$, verify:

$$\mu_1 + \mu_2 = 0 \tag{3.5.6}$$

which is true for two purely imaginary- or real conjugate numbers. Thus the test function is

$$\phi_{NS,PD} = \det \left(\tilde{\mathbf{B}}_\odot \right) \tag{3.5.7}$$

When the test function is zero, the Floquet exponents are checked. Two real conjugates are associated with a neutral saddle point, which is not considered a bifurcation and is ignored. As a note: since $\tilde{\mathbf{B}}$ is diagonal, the bialternate product is also diagonal.

3.5.3 Calculating determinant efficiently

Calculating the determinants needed for BP, NS and PD detection for large scale structures might not be numerical stable. Instead the *bordering technique* might be used, where the calculation of the determinant of $\mathbf{G}$ is replaced with calculation of a scalar function g which vanishes at the same time as the determinant [23]

$$\begin{bmatrix} \mathbf{G} & \mathbf{p} \\ \mathbf{q}^* & 0 \end{bmatrix} \begin{bmatrix} \mathbf{w} \\ q \end{bmatrix} = \begin{bmatrix} \mathbf{0} \\ 1 \end{bmatrix} \tag{3.5.8}$$

where vectors $\mathbf{p}$ and $\mathbf{q}$ can be arbitrarily chosen as long as they ensure nonsingularity of the system. This means they must be adapted or recalculated along the branch to ensure good conditioning of the bordered matrix.

g is related to $\mathbf{G}$ by Cramer's rule

$$g = \frac{\det \begin{pmatrix} \mathbf{G} & 0 \\ \mathbf{q}^* & 1 \end{pmatrix}}{\det \begin{pmatrix} \mathbf{G} & \mathbf{p} \\ \mathbf{q}^* & 0 \end{pmatrix}} = \frac{\det(\mathbf{G})}{\det \begin{pmatrix} \mathbf{G} & \mathbf{p} \\ \mathbf{q}^* & 0 \end{pmatrix}} \tag{3.5.9}$$

3.5.4 Localisation

When a bifurcation is detected using the test functions, the precise frequency where it happens should be localised. To do this, a augmented system is formed by adding the scalar test function ϕ to eom eq. (3.2.28).

$$\mathbf{h}_{aug}(bmz, \omega) = \begin{bmatrix} \mathbf{h}(\mathbf{z}, \omega) \\ \phi(\mathbf{z}, \phi) \end{bmatrix} = 0 \tag{3.5.10}$$

The bordered technique (3.5.8) is used to define the test function ϕ, ie. $\phi = g$ with $\mathbf{G}$ defined as: For fold and BPs, $\mathbf{G} = \mathbf{h_z}$. For NS and PD, $\mathbf{G} = \tilde{\mathbf{B}}_\odot$.

Thus for localising the bifurcation, the augmented system:

$$\mathbf{h}_{aug} = \begin{bmatrix} \mathbf{h}(\mathbf{z}, \omega) \\ g(\mathbf{z}, \phi) \end{bmatrix} = 0 \tag{3.5.11}$$

$$\mathbf{J}_{aug} = \begin{bmatrix} \mathbf{h_z} & \mathbf{h}_\omega \\ g_\mathbf{z} & g_\omega \end{bmatrix} \tag{3.5.12}$$

is solved using Newton-Raphson iterations. The derivatives of the test function is needed. Using the bordered system, the derivatives are

$$g_\alpha = -\mathbf{v} * \mathbf{G}_\alpha \mathbf{w} \tag{3.5.13}$$

where α denotes one of the components of $\mathbf{z}$ or *omega*. *bmv* and $\mathbf{w}$ is found by solving the bordered system and its transpose, restated here:

$$\begin{bmatrix} \mathbf{G} & \mathbf{p} \\ \mathbf{q}* & 0 \end{bmatrix} \begin{bmatrix} \mathbf{w} \\ q \end{bmatrix} = \begin{bmatrix} \mathbf{0} \\ 1 \end{bmatrix}, \quad \begin{bmatrix} \mathbf{G} & \mathbf{p} \\ \mathbf{q}* & 0 \end{bmatrix} * \begin{bmatrix} \mathbf{v} \\ q \end{bmatrix} = \begin{bmatrix} \mathbf{0} \\ 1 \end{bmatrix} \tag{3.5.14}$$

Thus only G_α needs to be calculated.

For fold and BPs,

$$G_\alpha = \mathbf{h}_{\mathbf{z}\alpha} \tag{3.5.15}$$

where $\mathbf{h}_{\mathbf{z}\alpha}$ is the derivative of the Jacobian $\mathbf{h}_z$ wrt. α, calculated by finite difference. When $\alpha = z_1, ..., z_{(2N_H+1)n}$, $\mathbf{h_{zz}}$ is the Hessian matrix.

For NS and PD, properties of the bialternate product gives:

$$\mathbf{G}_\alpha = \frac{\partial}{\partial \alpha} \left(\tilde{\mathbf{B}}_\odot \right) = \left(\frac{\partial}{\partial \alpha} \tilde{\mathbf{B}}_\odot \right) = \begin{bmatrix} \frac{\partial \tilde{\lambda}_1}{\partial \alpha} & & & \\ & \frac{\partial \tilde{\lambda}_2}{\partial \alpha} & & \\ & & \ddots & \\ & & & \frac{\partial \tilde{\lambda}_{2n}}{\partial \alpha} \end{bmatrix}_\odot \tag{3.5.16}$$

Instead of calculating the derivatives of the Floquet exponents by finite difference, which would require calculating the eigenvalues of $\mathbf{B}$ for each perturbation of the components of $\mathbf{z}$ and ω, $(2N_H + 1)n + 1$ evaluations, the properties of eigenvalues derivatives is used [1]

$$\frac{\partial \tilde{\lambda}_i}{\partial \alpha} = \left(\mathbf{\Lambda}^{-1} \frac{\partial \mathbf{B}}{\partial \alpha} \mathbf{\Lambda} \right)_{\xi_i, \xi_i} \tag{3.5.17}$$

where $\mathbf{\Lambda}$ is the matrix of right eigenvectors of $\mathbf{B}$ and ξ_i is a indexation vector containing the index of the $2n$ Floquet exponents $\tilde{\mathbf{\lambda}}$ among the eigenvalues $\mathbf{B}$(ie. $\tilde{\lambda}_i = \lambda_{\xi_i}$). An analytic expression for $\frac{\partial \mathbf{B}}{\partial \alpha}$ can then be found from (3.2.41).

Eq (3.5.17) is valid as long as there is no repeated eigenvalues, which is verified for most situations except when a pair of complex conjugates turn into a pair of real eigenvalues. Since this transition occurs quickly, it is reasonable to assume (3.5.17) is valid. For scenarios with repeated eigenvalues, other expressions can be found in [1].

Remark that $\mathbf{h}_{\mathbf{z}\alpha}$ is a zero matrix for all components in $\mathbf{z}$ related to linear dof/Fourier coefficients. Thus it is not necessary to evaluate all $(2N_H + 1)n + 1$ terms g_α, but only the $(2N_H + 1)n_{red} + 1$ where n_{red} is related to nonlinear dofs.

3.5.5 Example

The bifurcations for the coupled duffing system (1.5.1) is shown in figure 3.5.1. Fold, BP and NS bifurcations are found along the branch. As expected fold bifurcations are found close to the two resonance peaks. In fig. 3.5.1(b) a branch of periodic solutions emerges from a BP bifurcation. In fig 3.5.1(c) QP oscillations appears after a NS bifurcation.

The evaluation of test functions for BP bifurcations along the branch is shown in fig. 3.5.2. In fig 3.5.2(c) it seen that the test function based on the determinant become very large close to singular points whereas the bordering technique produce numerical stable values.

3.5.6 Summary

Bifurcation analysis can help understand nonlinear phenomena such as amplitude jumps, quasiperiodic oscillations and period doubling. They are found during continuation by using test functions; a summary is shown in fig 3.5.3 for Hills method.
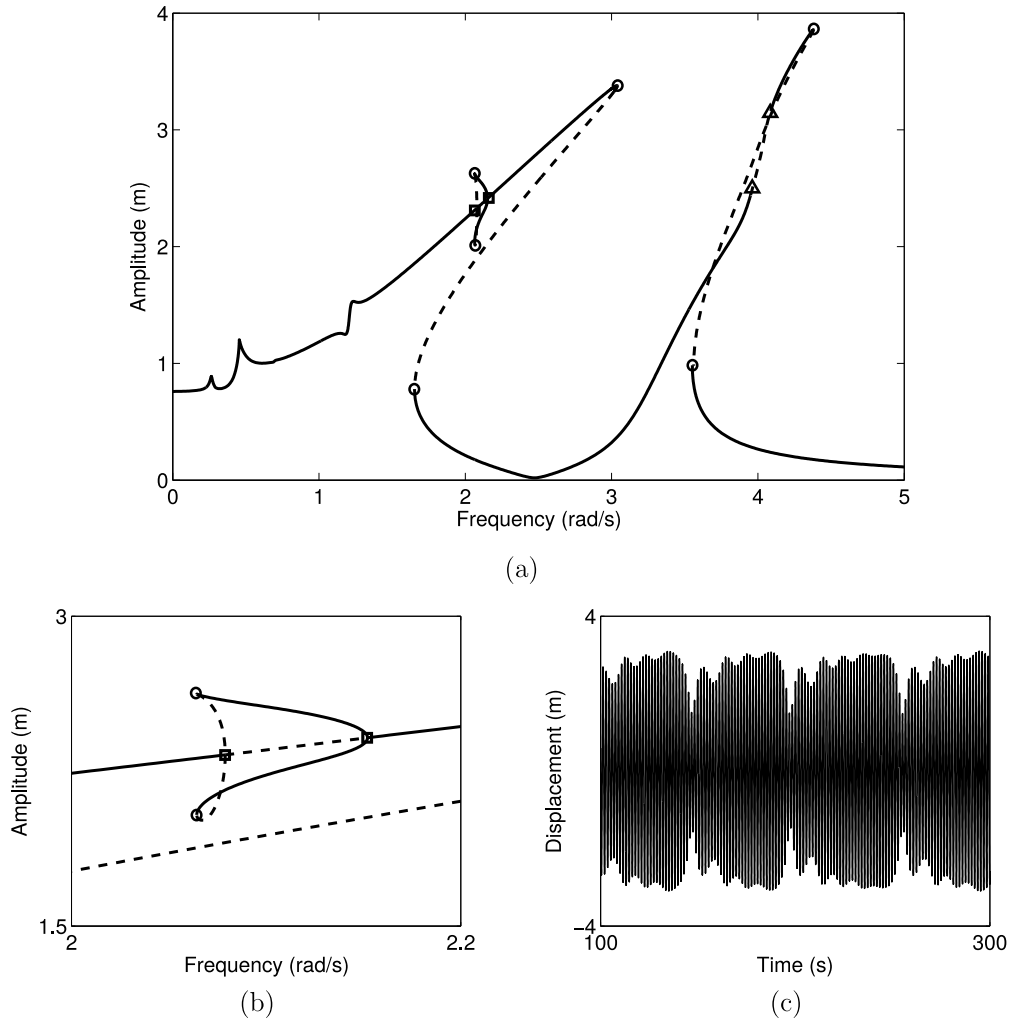
Figure 3.5.1: Bifurcation analysis of the coupled Duffing system at x_1 for $f = 2$N. **(a)** Stable and unstable solutions are represented with solid and dashed lines. Fold, BP and NS bifurcations are represented with ○, □ and △ markers, respectively. **(b)** Close-up of the NRFC in the vicinity of the BPs and the emerging branch. **(c)** QP oscillations for a forcing frequency of $\omega = 4$ rad/s.
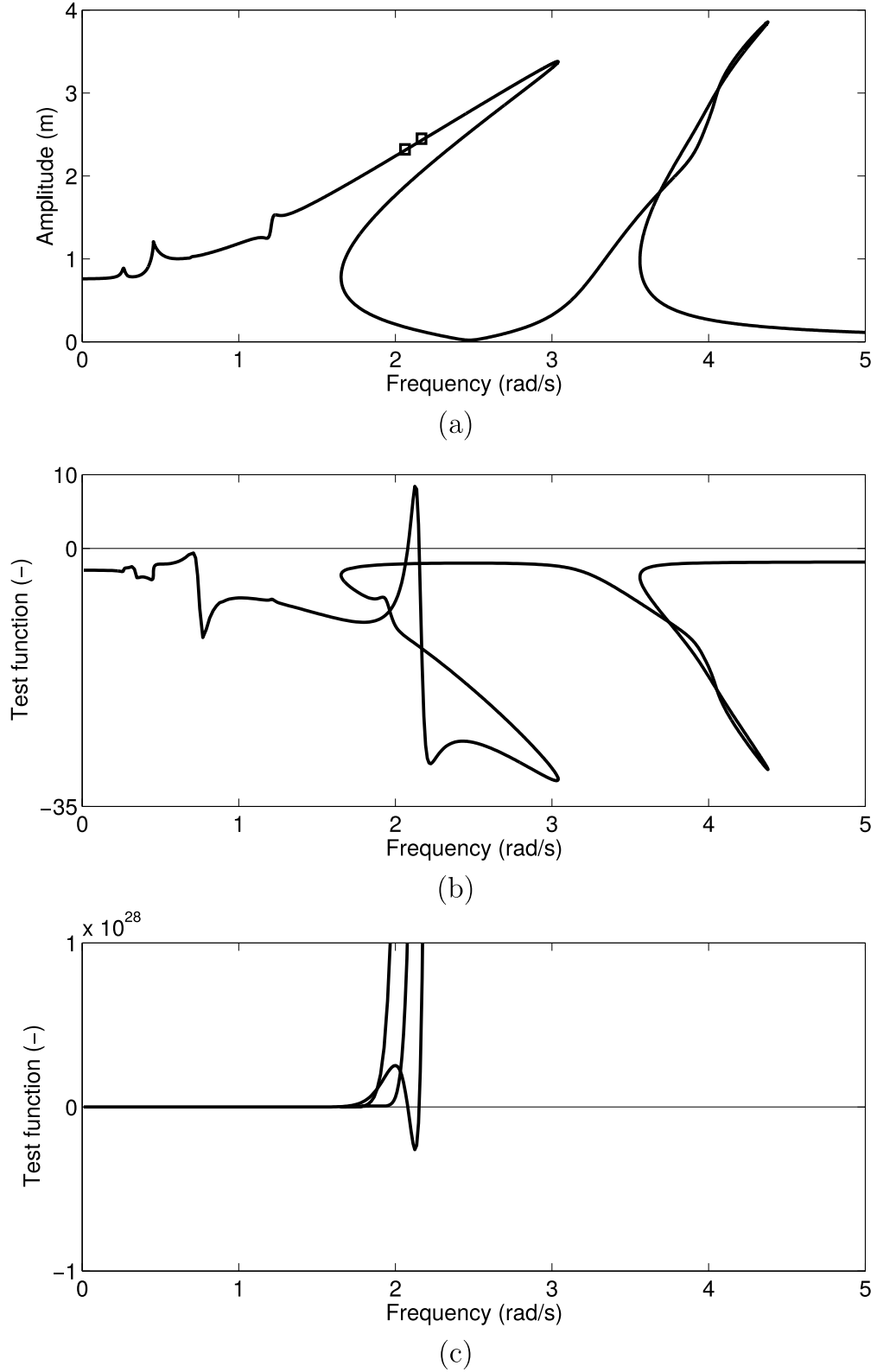
Figure 3.5.2: Test functions for BP detection. **(a)** NRFC and BP bifurcations marked by □; **(b)** test function based on the bordering technique; **(c)** test function based on the determinant. It is noted that the determinant gets higher than 10^{28}. The machine precision for a double precision 64 bit number is $\epsilon = 2^{-52} \sim 10^{-16}$, which means that the maximum spacing between two (normalised) numbers can be at max $2\epsilon |x|$ in order to be represented correct.

1. Detection of *fold bifurcation*:

$$\phi_F = t_w$$

2. Detection of *bifurcation point* (BP):

$$\phi_{BP} = g_{bp}$$

   from the bordering system in eq. 3.5.8 with

   $$\mathbf{G}_{BP} \begin{bmatrix} \mathbf{h_z} & \mathbf{h}_\omega \\ & \mathbf{t}^T \end{bmatrix}$$

3. Detection of *Neimark-Sacker* (NS) and *period doubling* (PD) bifurcations:

   $$\phi_{NS,PD} = g_{NS,PD}$$

   from the bordering system in eq. 3.5.8 with $\mathbf{G}_{NS,PD} = \tilde{\mathbf{B}}_\odot$. When $\phi_{NS,PD} = 0$, matrix $\tilde{\mathbf{B}}$ has μ_1 and μ_2 among its eigenvalues, with

   $$\mu_1 + \mu_2 = 0$$

   - If $\mu_{1,2} = \pm i\beta$ with $\beta \neq \pi/T$, a NS bifurcation is detected.
   - If $\mu_{1,2} = \pm i\beta$ with $\beta = \pi/T$, a PD bifurcation is detected.
   - If $\mu_{1,2} = \pm\beta$ a neutral saddle point is detected.

Figure 3.5.3: Test functions for detection of codimensional-1 bifurcation of NFRCs

Chapter 4

Implementation

The methods presented in the previous chapters are implemented as a library in python and available online [27]. The code depends on the standard python libraries numpy, scipy and matplotlib and can run on all operating systems. Care have been taking in order to ensure correctness of the implementations; as much as it have been possible examples from papers and data given from University of Liege(ULg) have been recalculated to ensure that the same results were obtained. All code are written for this thesis and implement most notably:

- FEM code: generate FE matrices $\mathbf{M}, \mathbf{K}$ from a *gmsh*-mesh file. Different types of elements are available. Boundary conditions are enforced on system matrices.

- Nonlinear newmark integration with sensitivity analysis

- Morlet wavelet/wavelet transform

- Restoring force surface

- Integration, filtering and periodicity calculation of signals

- NNM continuation and stability

- HB continuation, stability and bifurcation

- FNSI, linear and nonlinear parameter estimation. Stabilisation diagram for determining model order

- FRF calculation from periodic signals with multiple periods or from nonperiodic signals using spectral densities. Standard deviation of FRF between periods is calculated.

- Modal properties including MAC calculation.

- Sine sweep(linear and logarithmic) and random periodic excitation.

- Polynomial and piecewise cubic splines available for estimation.

- Additional types of nonlinearities available for simulation with Newmark, HB and NNM: Piecewise linear and hyperbolic tangent(tanh), the latter only for damping.

As an example of the library approach, the following two examples shows how FNSI
identification and HB continuation are done. Most methods returns a class storing all
information, making multiple runs with different settings easy. To keep the examples
short, they are run with default settings.

```
# Paw, 2017
from numpy import np
from vib.signal import Signal
from vib.fnsi import FNSI
from vib.nlforce import NL_force, NL_polynomial
from vib.common import modal_properties

# load time signal
# nsper is the number of signals per period, iu the dof(s) where the force(s) works
mat = np.load(filename + '.npz')
u, ydd, fs, nsper, iu = mat['u'], mat['ydd'], mat['fs'], mat['nsper'], mat['iu']

# create class, integrate and select period(s) (fnsi works on displacements)
signal = Signal(u, fs, ddy=ddy)
signal.get_displ(lowcut, highcut)
signal.cut(nsper, per=[7,8])

# setup nonlinear type and where it works (-1: attached to ground)
inl = np.array([[0,-1], [1,-1]])
enl = np.array([3,3])
nl_pol = NL_polynomial(inl, enl)
nl = NL_force().add(nl_pol)
fmin, fmax = 0, 10
ims, nmodel = 22, 4
fnsi = FNSI(signal, nl, fmin, fmax)
fnsi.calc_EY()
fnsi.svd_comp(ims)
fnsi.id(nmodel)
# Get identified nl parameters and linear frf.
knl, H, He = fnsi.nl_coeff(iu)
# get linear modal parameters
modal = modal_properties(fnsi.A, fnsi.C)
# Done.
```

and for HB:

```
# Paw, 2017
import numpy as np
from vib.hb.hb import HB
from vib.hb.hbcommon import hb_signal
from vib.nlforce import NL_force, NL_polynomial

# setup system
M = np.array([[m1,0],[0,m2]])
C = np.array([[c1,0],[0,c2]])
K = np.array([[k1+k2, -k2],[-k2, k2+k3]])
inl = np.array([[0,-1], [1,-1]])
enl = np.array([3,3])
knl = np.array([mu1, mu2])
nl_pol = NL_polynomial(inl, enl, knl)
nl = NL_force()
nl.add(nl_pol)
# starting frequency, force amplitude and force dof
f0, famp, fdof = 1, 3, 0

# create HB class, periodic solution and continuation incl stability and
# bifurcation.
hb = HB(M,C,K, nl)
omega, z, stab, lamb = hb.periodic(f0, famp, fdof)
hb.continuation()

# Run for another forcing level
hb2 = HB(M,C,K, nl)
hb2.periodic(f0, 2*famp, fdof)
```

```
hb2.continuation(bifurcation=False)
# Done
```

All the examples from the previous chapters are included in the examples directory in the source code, and should run on any python3 installation.

The desired functionality is loaded from the vibration library in the top of each example. For instance `from vib.signal import Signal` includes a class(methods) for calculating periodicity, filtering and integrating the acceleration signal. The signal class is the passed to the FNSI process, loaded by `from vib.fnsi import FNSI`.

It is noted that the functionality of this library correspond to the Ni2D software by Nolinsys, a company founded by researches at Liege University, and should run at the same speed. The python library includes *all* methods included by Ni2D. The notable difference is that Ni2D have a graphical interface and requires, besides a license to Ni2D, a license to matlab. The python library does however have a interactive graphical interface for selecting RFS and inspecting the evolution of {stability changes(ie. Floquet exponents), harmonic components and periodic solution}(not shown in this report); both are inspired by Ni2D. Ni2D cannot use splines for estimation.

Chapter 5

Application

This chapter present two more involved cases of identification. The first case is identification of the COST beam, introduced as a standard test case for polynomial nonlinearities, ie. two polynomial nonlinearities at the same DOF. The second case demonstrate the usage of cubic spines to identify a system with two different clearances. The clearance distances are also found.

5.1 COST beam

The European action COST F3 nonlinear beam [13] was introduced in 2003 as a benchmark system for nonlinear vibrations. The experimental setup is shown in fig. 5.1.1 and consists of a clamped beam with a thin beam part at the end of the main beam.
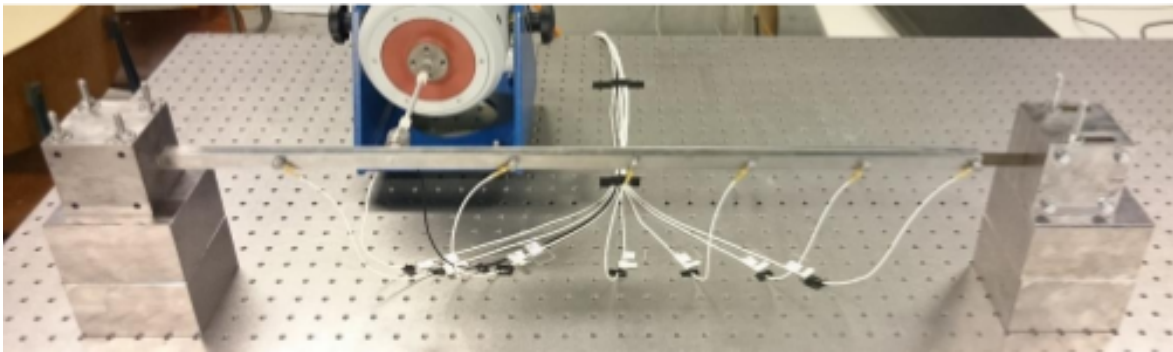

Figure 5.1.1: Experimental setup for the COST beam. Both vertical and horizontal setups were tested at University Liege(ULg). Horizontal setups avoids gravitational effects which cannot be ignored due to static deflection of the thin beam.

Accelerations are measured evenly along the beam at seven locations and excited at node two. From Lenaerts, Kerschen, and Golinval [24] is it known that the system exhibit a (geometric) cubic nonlinearity located at the tip of the main beam. Using data given at the Nolinsys course, the beam will be identified as an example of a multiple inputs, multiple outputs(MIMO) system. After successful identification a FE model is built using the identified parameters and used for further examination.
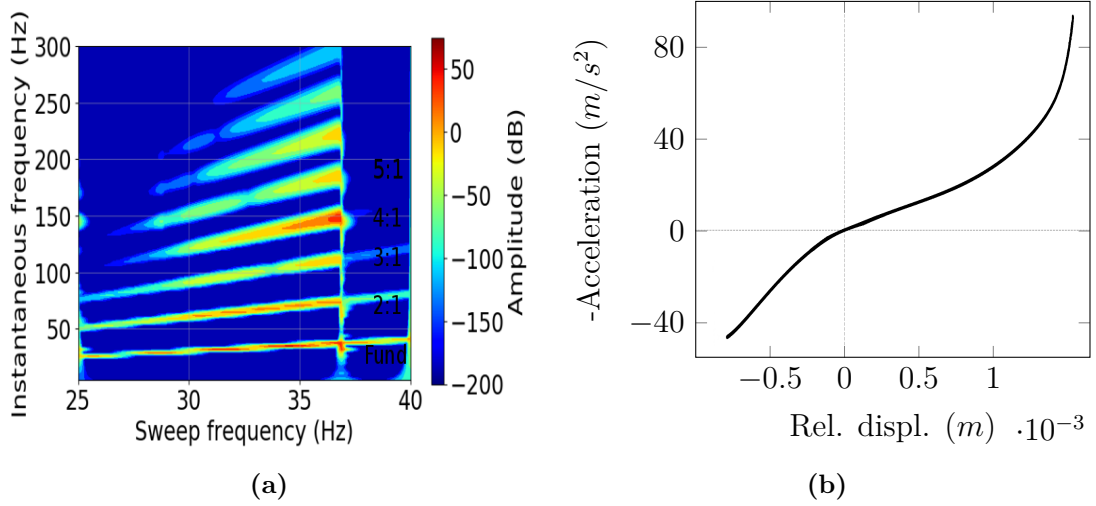
Figure 5.1.2: Characterisation using a forward sine sweep. Sweep rate: 10Hz/min. Shown for the tip of the main beam. **(a)**: Wavelet transform; **(b)**: Restoring force surface showing the restoring force.

The cubic nonlinearity is described to be due to *large deformation of the tip of the thin beam.* This is a bit vague description and could include both large rotations and midplane stretching. As both ends are clamped, the nonlinearity probably stems from midplane stretching of the thin beam. In [17] it is shown how both midplane stretching and large rotations of a beam leads to a duffing equation with a cubic hardening.

Due to the thin beam, the effect of gravity is not negligible. In a vertical setup the static deflection at the beam tip imposes a non-negligible prestress in the thin beam, giving a nonsymmetric restoring force. This is identified as a quadratic nonlinearity and the effect is simply removed by using a horizontal setup.

5.1.1   Identification

The time series were obtained from University Liege(ULg), where the beam was built as part of the COST F3 project. Unfortunately, despite several request, only noise-free simulated data were given and not the original experimental data.

For characterisation the beam is excited with a sine sweep. The wavelet transform and RFS is seen in fig. 5.1.2. From the WT, the fundamental forcing frequency is seen along with even(2:1,4:1,...) and uneven(3:1,5:1,...) higher harmonics. These higher harmonics are symptoms of quadratic and cubic nonlinearities. As the FRF shows the total restoring force, it is hard to identify the correct nonlinear function. However the asymmetry indicate an even nonlinearity and the general shape resembles a cubic polynomial.

For estimation the beam is excited with a periodic broadband input with flat amplitude spectrum, i.e. a multisine at low and high level. At low and high level, the beam behaves linear and nonlinear respectively. To avoid leakage in the identification due to transient behavior, the periods used are selected from a plot of the periodicity. From fig. 5.1.3 is seen that transients are apparent in the first two periods and not apparent in periods 4-7, which are used for the identification.
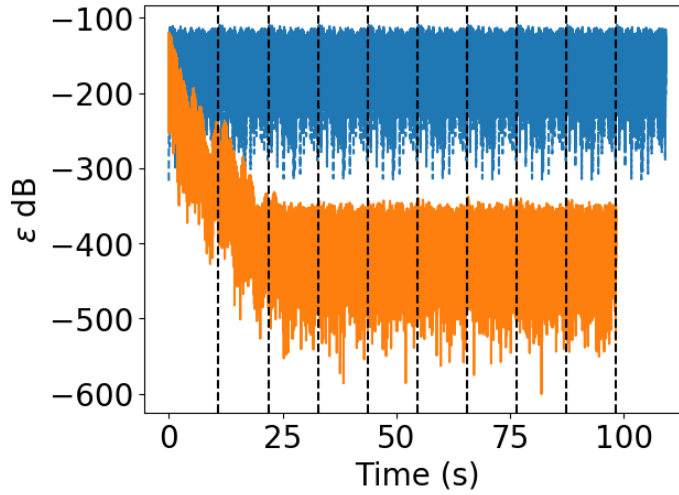
Figure 5.1.3: Periodicity of recorded signal at high level wrt. the last period. Measured at the nonlinear dof. Low level excitation is not shown, as it is not used for NL estimation.

Figure 5.1.4 shows the stabilisation diagram used for determine model order. Fig. 5.1.4(a) is used for linear identification and is fully stabilised at order 6. Fig. 5.1.4(b) shows the nonlinear system identified with linear analysis, ie. without specifying nonlinear basis functions. The first mode does not stabilise, which normally indicates that the supplied basis functions are inadequate to represent the nonlinearity. Fig. 5.1.4(c) shows the stabilisation after using a quadratic and cubic basis function. The first mode stabilises at model order 6, ie. the identification is most likely trustworthy and the nonlinearities are described by these functions.

The identified linear parameters are shown in table 5.1.1. At high excitation using linear analysis, the natural frequency increases for the first mode which is expected from a hardening nonlinearity. Using the two basis functions for nonlinear analysis, the parameters are estimated to be same as obtained at low level, ie. correct.

	Mode	Frequency (Hz)	Damping ration (%)	Deviation from linear freq. (%)
Low	1	31.3	1.27	
	2	143.6	0.29	
	3	397.8	0.14	
High	1	33.1	1.08	5.7
	2	144.1	0.29	0.3
	3	398.0	0.14	0.05
High	1	31.3	1.27	10^{-3}
	2	143.6	0.29	10^{-5}
	3	397.8	0.14	10^{-6}

Table 5.1.1: Estimated linear natural frequencies and damping ratios for the COST beam. **(upper)**: Low level, linear identification; **(middle)**: High level, linear identification; **(lower)**: High level, nonlinear identification.

The estimated nonlinear coefficients are shown in figure 5.1.5. The deviation of the real part is just within 1% and the imaginary part are around three orders of magnitude smaller, indicating a good estimation.
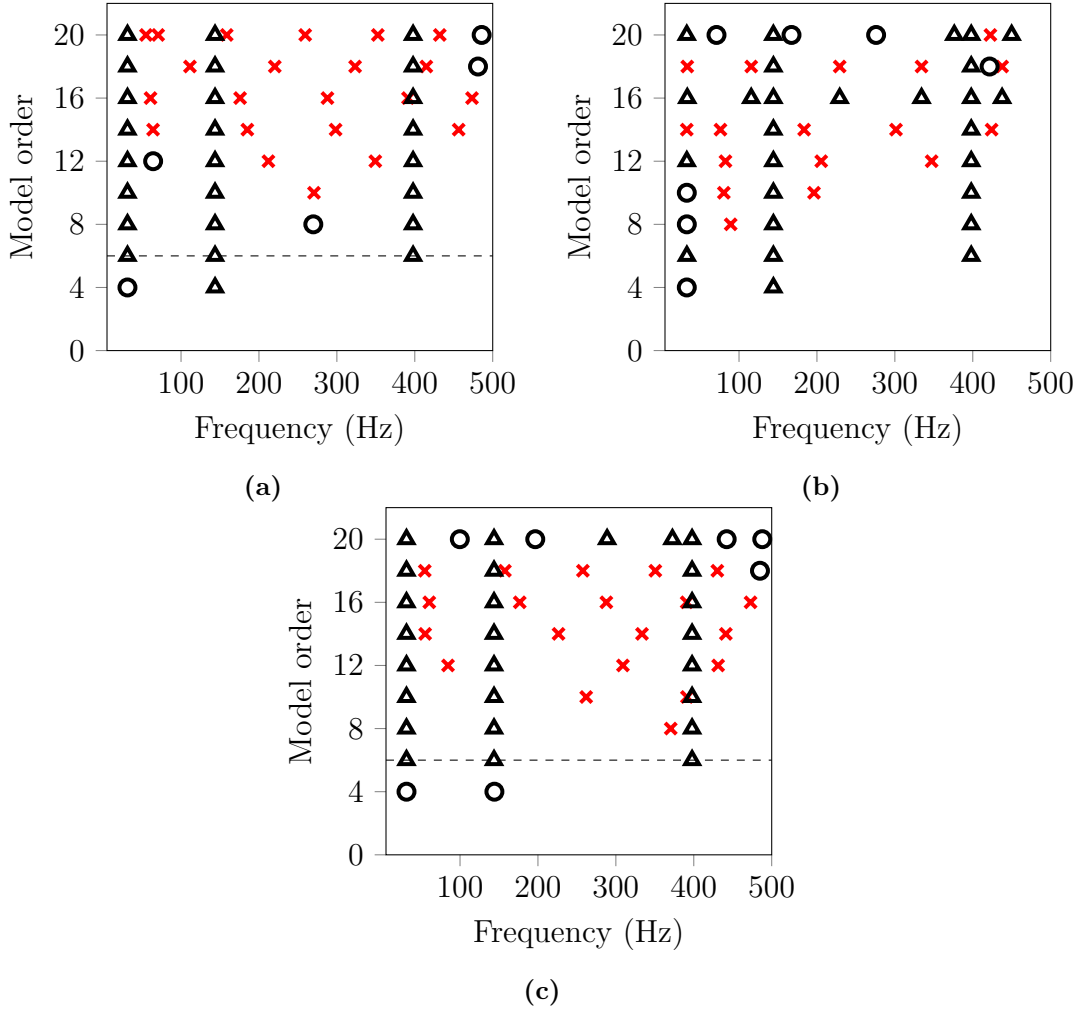
Figure 5.1.4: Estimation of model order. ×: new frequency(pole); ∘: extra stabilisation in MACX; △: full stabilisation. **(a)**: Low level, linear identification; **(b)**: High level, linear identification - no stabilisation of first mode; **(c)**: High level, nonlinear identification - stabilisation of first mode;

Finally fig. 5.1.6 shows the FRF. Nonlinear distortion is seen from the signal at high level excitation. The FRF(blue) from low level excitation and identified by FNSI with basis functions(green) match.

5.1.2 Design

The test setup is modelled as a FE model shown in fig 5.1.7, using 14 and 3 two-dimensional Bernoulli-Euler beam elements for the main and thin beam respectively. The connection between the two beams is modelled by an additional linear rotational stiffness, as suggested in [24], resulting in a model with 35 dofs.

The geometric properties are also given in [24] and listed together with the mechanical properties in tables 5.1.2.
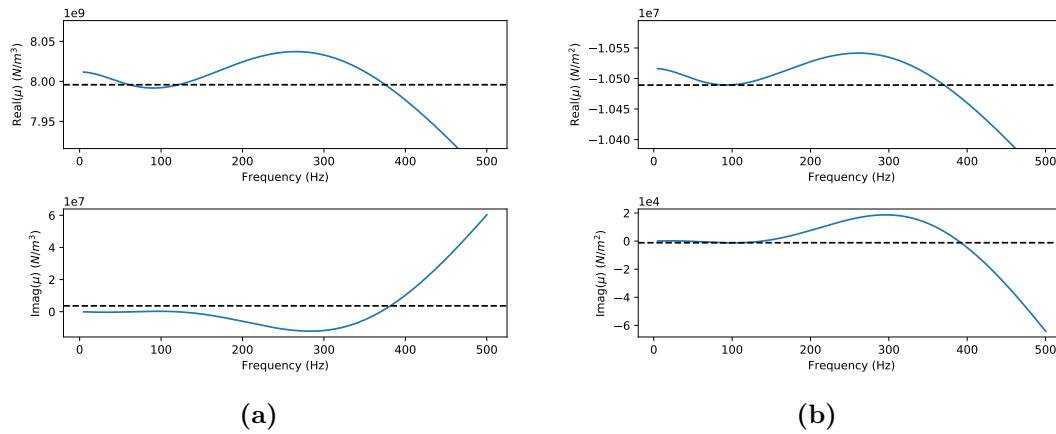
Figure 5.1.5: Real and imaginary part of estimated nonlinear coefficients μ_1 and μ_2. The variation of $\text{Re}(\mu)$ is seen to be within a 1 interval. The imaginary part is about three orders of magnitude smaller. Both indicates a good quality of the estimation. The spectral averages of the real part and logarithmic ratio between the real and imaginary part $\left(\log_{10}\left(\frac{\text{Re}(\mu)}{\text{Im}(\mu)}\right)\right)$ are: **(a)**: $\mu_1 = 8.0 \times 10^9 m/n^3$, ratio = 3.34; **(b)**: $\mu_2 = -1.05 \times 10^7 m/n^2$, ratio = 3.96.
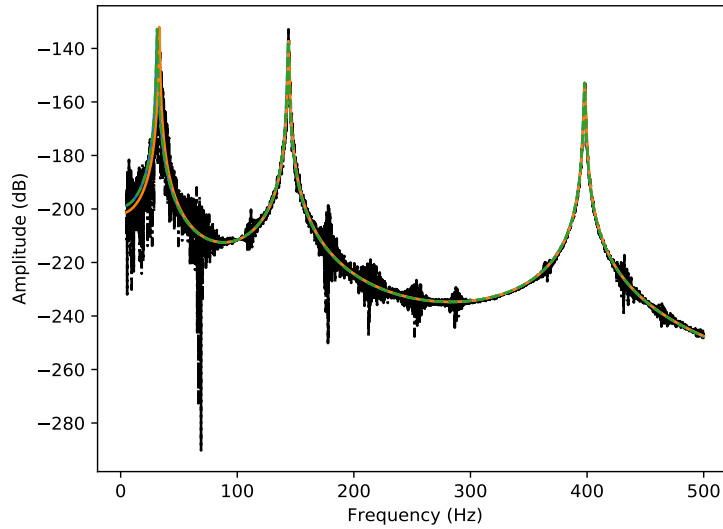

Figure 5.1.6: FRF. Nonparametric(NP) is FRF directly from signal, parametric is identified FRF. ——: NP from high level excitation; ——: NP from low level excitation. ——: Linear parametric from high level excitation. - - - -: nonlinear parametric from high level excitation.
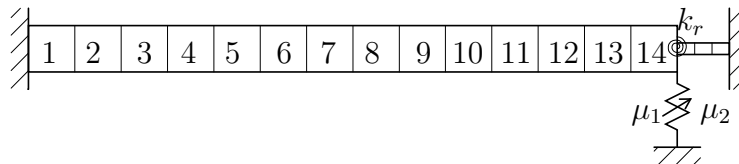

Figure 5.1.7: FE model of the COST beam.

	Length(m)	Width (m)	Thickness (m)
Main beam	0.7	0.014	0.014
Thin beam	0.04	0.014	0.0005

Young's modulus(N/m^2)	Density(kg/m^3)	μ_1 (N/m^3)	μ_2 (N/m^2)	Damping
2.05×10^{11}	7800	8×10^9	-1.05×10^7	$\mathbf{C} = 3 \times 10^{-7}\mathbf{K} + 5\mathbf{M}$

Table 5.1.2: Geometric and mechanical properties for the nonlinear beam

The damping is proportional damping, giving a modal damping ration of 1.27% for the first linear mode which is high for a steel beam. But large displacements tends to be higher damped, thus the damping is not expected to be same for the linear and nonlinear case.

Figure 5.1.11 shows a comparison between a linear forward and backward sine sweep and the NFRC computed by HB. The response is asymmetric due to the presence of the quadratic nonlinearity. The jump down occurs because of the hardening(cubic) behavior.
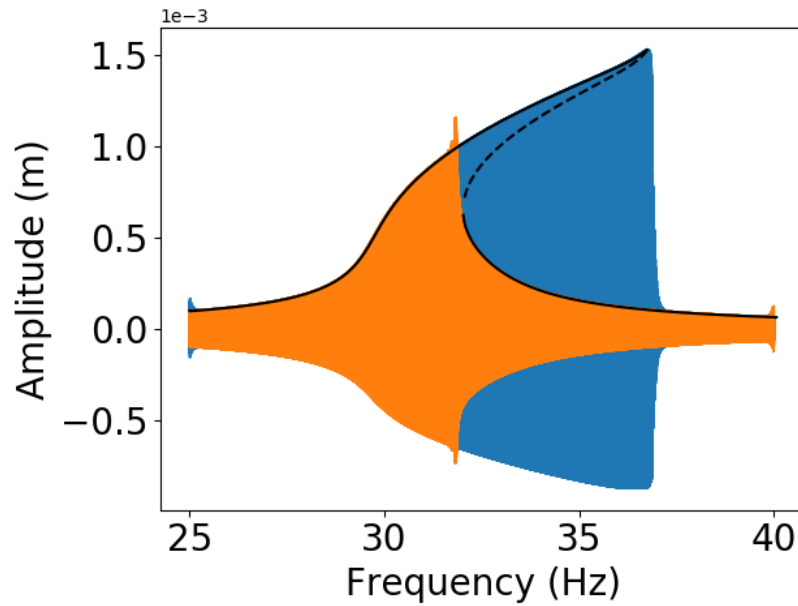

Figure 5.1.8: Comparison between forward and backward sine sweep(colours) with HB(black line). Sweep parameters: Amplitude: 3N, sweep rate: 10Hz/min. Stability is indicated for HB. Shown for the tip of the main beam, ie. the nonlinear connection.

Figure 5.1.9 shows the evolution of the harmonic components along the curve. As expected from the asymmetry, there is strong participation of the constant term, followed by the 2nd harmonic. Both due to the quadratic nonlinearity.

The NNMs of the underlying conservative system is shown in fig 5.1.10. The NNM frequency increases with increasing energy, which is due to the hardening behavior of the nonlinear stiffness. The inserts shows the modal shapes of the main beam for different energy levels. The modal shapes are synchronous. The FEPs shows one branch emerging from each NNM backbone. These are called tongues and are said to reveal internal resonance. The tongue for the first NNM, fig. 5.1.10(a), shows a 9:1 internal resonance between the first and third NNM. Their linear frequencies are incommensurate as seen in table 5.1.1, but the frequency for the first NNM increases more rapidly than for the third NNM, resulting in a 9:1 ratio between the frequencies is realised. This might be of more theoretical interest, as a high energy level indicate very large displacements.

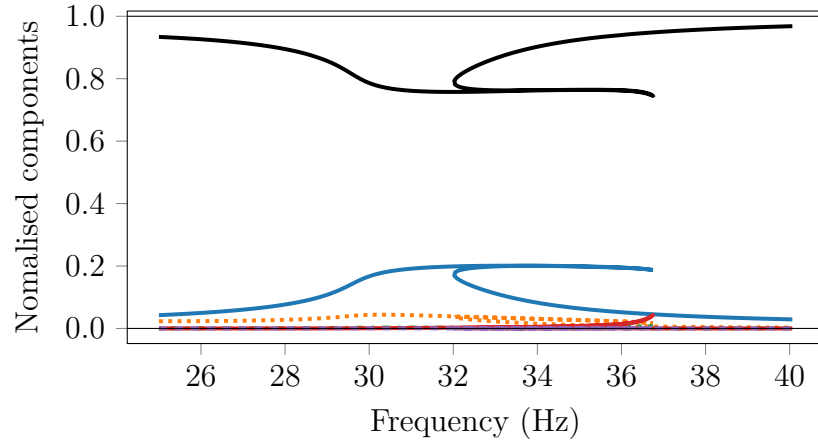Finally, the NNM backbone traces the lotus as seen in fig. 5.1.11.

Figure 5.1.9: Evolution of HB components. ——: Constant; ——: 1st; ⋯⋯⋯: 2nd; —·—: 3th; ——: 4th; - - - -: 5th;
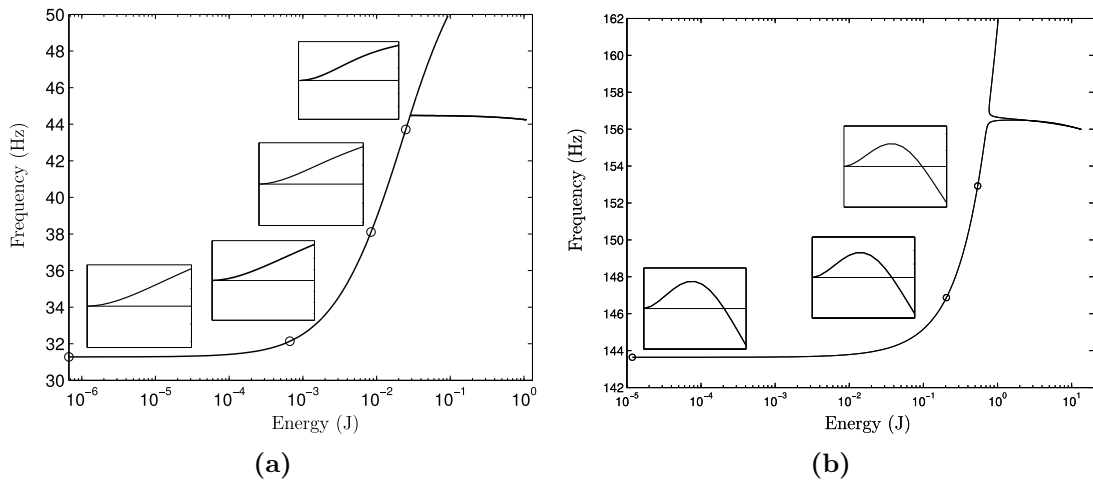

Figure 5.1.10: Frequency-energy plot(FEP) of the **(a)** first- and **(b)** second NNM. Inserts show the NNM shapes (displacements of the main beam) for different energy levels.
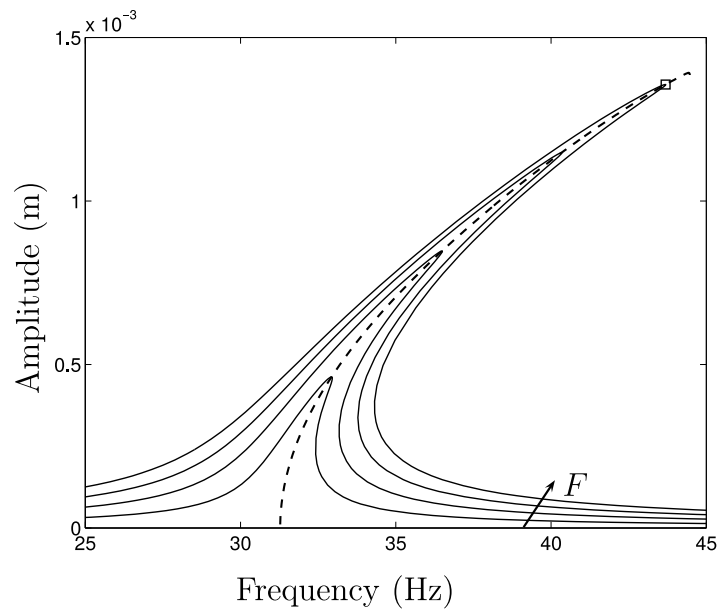
Figure 5.1.11: NFRC for forcing amplitudes (1,2,3,4)N from HB. The dashed line is the backbone of the first NNM and tracks the lotus; □ denote $F = 4N$.

5.2 System with clearences

A single DOF model with two clearances is simulated to obtain data for characterisation with WT and RFS and estimation with FNSI. The model is only briefly introduced below and the section is not intended to be a complete or thorough derivation; as the interesting part is not the model, but applications of the methods treated in this thesis. Only changes in stiffness during impact is considered, ie. impact damping as given by some impact models is ignored

5.2.1 Model

The model is a clamped-free beam with a pair of elastic stops at the free end with optionally asymmetrical clearance distances $a_\pm$, see fig 5.2.1.
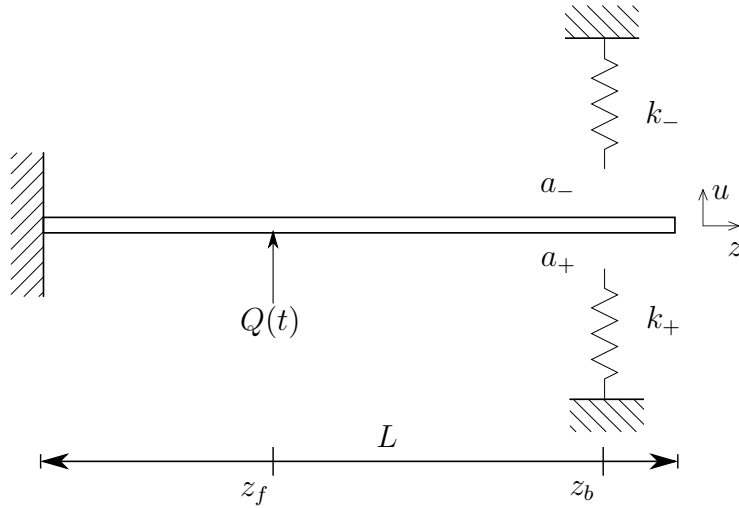

Figure 5.2.1: Beam with elastic stops

The bending vibrations of the beam are given by

$$\rho A \frac{\partial^2 u(z,t)}{\partial t^2} + \frac{\partial^2}{\partial z^2}\left(EI \frac{\partial^2 u(z,t)}{\partial z^2}\right) + f_{res}(u(z_b,t))\delta(z - z_b) + P_0 \sin(\Omega t)\delta(z - z_f) = 0$$

(5.2.1)

where $EI, \rho, A, \delta(z), Q_0, u(z,t)$ denotes the bending stiffness, mass density, cross section area, Dirac delta function, forcing amplitude and relative transverse displacement, respectively, for the assumed uniform beam. The forces are assumed point loads, where the external force act in z_f and the vibro-impact force at the impact location z_b is given by

$$f_{res}(u) = \begin{cases} k_+(u - a_+) & u \geq a_+ \\ 0 & a_+ > u > a_- \\ k_-(u - a_+) & u \leq -a_- \end{cases}$$

(5.2.2)

where $a_\pm$ are the clearance distances and $k_\pm$ the associated stiffness's. Thus the stops behaves as one-sided springs.

The left end is clamped, giving the boundary conditions

$$u(0,t) = 0, \quad u_z(0,t) = 0 \tag{5.2.3}$$

and at the right end, between stops, the beam moves freely giving a moment- and transverse stress free condition

$$a_+ > u > a_- : \quad u_{zz}(L,t) = 0, \quad u_{zzz}(L,t) = 0 \tag{5.2.4}$$

When the elastic stops are hit, the stress $\sigma = EIu_{zzz}$ is no longer zero

$$a_+ < u, u < a_- : \quad \sigma(z_b, t) = -f_{res}(u) \tag{5.2.5}$$

Notice that the stress is opposite in direction to the displacement. For $k_\pm \to \infty$, the stops are rigid and velocity changes sign instantly at each impact, known as the Signorini nonpenetration condition.

An approximate solution to (5.2.1) is given by the modal expansion

$$u_n(z,t) = \sum_{i=1}^{n} \phi_i(z) q_i(t) \tag{5.2.6}$$

where ϕ_i is the mode shape satisfying the stated essential boundary conditions and related to the i'th natural frequency ω_i; together they define the i'th mode for linear system of eq. (5.2.1), ie. with $f_{res}(u) = 0$.

The modal components $q_i(t)$ satifies the coupled nonlinear differential equation

$$\ddot{q}_i(t) + 2\xi\omega_i\dot{q}_i(t) + \omega_i^2 q_i(t) + \frac{\phi_i(z_b)}{\rho AL} f_{res}(u_n(z_b,t)) + \frac{\phi_i(z_f)}{\rho AL} Q_0 \sin(\Omega t) = 0, \quad i = 1, ..., n \tag{5.2.7}$$

where viscous damping have been added to account for dissipative effects. This is not easily solved. The preprint by Rebouças [37] list different techniques for solving vibro-impact models as well as an example of a thorough derivation of the nondimensionalized EOMs(though for a parametrically excited vibro-impact).

Numerical solution

When eq. (5.2.6) is driven around its first resonance, the higher order modes $(i \geq 2)$ are expected to have low influence as they are increasingly damped. Thus a single-mode expansion can be used, as long as the driving frequency is kept well below the second resonance.

Solving the system using Newmarks method, requires the derivatives of the restoring force to be continuous. [20] list different smoothening functions and the smoothening effect on the nonlinear response. However I prefer using local regularisation with Hermite polynomials in the interval $[a - \Delta, a + \Delta]$, where 2Δ is the size of the regularisation interval. Figure 5.2.2 shows an example of a regularised tri-linear restoring force; the purely linear behaviour of the restoring force outside the regularisation interval is kept, which is why this approach is favoured. [20] ensures continuity by changing the piecewise linear functions to trigonometric functions.
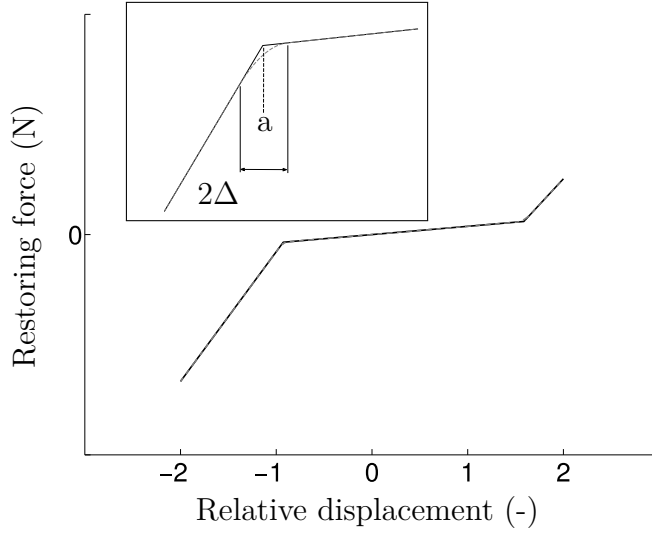
Figure 5.2.2: Example of piecewise-linear restoring force. The insert image shows a closeup of the effect of the regularization Δ.

A regularised trilinear model for stiffness' k_-, k, k_+ and clearances a_-, a_+ is given by,

$$f_{nl}(x) = \begin{cases} ka_+ + k_+(x - a_+) & x \geq a_+ + \Delta_+ \\ p_+(t(x)) & a_+ + \Delta_+ > x > a_+ - \Delta_+ \\ kx & a_+ - \Delta_+ \geq x \geq -(a_- - \Delta_-) \\ p_-(t(x)) & -(a_- + \Delta_-) > x > -(a_- + \Delta_-) \\ ka_- + k_-(x - a_-) & x \leq -(a_- + \Delta_-) \end{cases} \quad (5.2.8)$$

where x is the relative distance between the two DOFs defining the nonlinear connections, ie. the displacement for the single mode expansion.

The Hermite polynomials $p_\pm$ are defined as

$$p_\pm(t) = h_{00}(t)p_k + h_{10}(t)(x_{k+1} - x_k)m_k + h_{01}(t)p_{k+1} + h_{11}(t)(x_{k+1} - x_k)m_{k+1} \quad (5.2.9)$$

where p_k and p_{k+1} are the values of the restoring force at points $x_k = a_\pm - \Delta$ and $x_{k+1} = a_\pm + \Delta$, respectively. m_k and m_{k+1} are the values of the restoring force derivative at the same x_k and x_{k+1} points; they correspond to the stiffness coefficients k and $k_\pm$. The normalised displacement t (termed the *local scaled abscissa*) and h_{ij} functions are

$$t(x) = \frac{x - x_k}{x_{k+1} - x_k}$$
$$h_{00}(t) = 2t^3 - 3t^2 + 1, \quad h_{10}(t) = t^3 - 2t^2 + t$$
$$h_{01} = -2t^3 + 3t^2, \quad h_{11} = t^3 - t^2$$
$$\quad (5.2.10)$$

It should be noted that numerically solving systems with a large difference in stiffness(*stiff* systems) might not be easy. When the beam hit the stops, some spurious high frequencies might appear in the numerical solution. These spurious frequencies may disappear by choosing a smaller time-step and if not, the solutions becomes unstable. In that case a time integration method with numerical damping should be

used. A possibility is to use a Newmark scheme with $\gamma > \frac{1}{2}$ in order to introduce some numerical damping. Unfortunately this scheme is only of first order convergence and the effect of the damping can affect amplitude of the solution. Preferable another scheme should be used, see appendix C.3.1 for at bit more on the Newmark method and references to alternatives.

As a single mode model is used, an easier approach is to use a stiff first order ODE solver, eg. a *Radau*-type. Then either event-detection for impacts or the reformulation of the piecewise function (5.2.2) into

$$f_{res}(u) = u + (1 - \alpha)\frac{|u - a| - |u + a|}{2} \tag{5.2.11}$$

which is valid for symmetric stops $a = a_+ = a_-$ could be used. $||$ is the absolute value and $\alpha \leq 1$ is the slope in-between the stops, ie. 0. The slope of (5.2.11) is one after impact. To get stiffer impacts f_{res} is simply multiplied by a desired factor. The latter reformulation should be preferred as long as the time steps are not too large, which could correspond to a large penetration of the stop [1].

5.2.2 Identification

The one-mode approximation

$$\ddot{x} + 2\xi\omega\dot{x} + \omega^2 x + 3f_{res}(x) = q\sin(\omega_t t) \tag{5.2.12}$$

with symmetrical stops $a = 0.1745$, $\omega^2 = 1$, $\xi = 0.025$, $q = 0.03$ and f_{res} given by (5.2.11) is used. The factor 3 controls the impact stiffness.

Characterisation

The system (5.2.12) is excited by a linear sine sweep from $\omega_t = [0.001, 2]$rad/s with a sweep rate of 0.01Hz/min.

Figure shows the time series for a forward sweep and the NFRC calculated by HB. For HB the general model for f_{res} (5.2.8) is used, as the derivative of the restoring force is needed. A stiffening effect is seen, which is explained by the constraining effects of the stops. When the energy is increased, the stiffer stops prevents the amplitude from increasing proportionally and the system responds by increased frequency.

Figure 5.2.4(a) shows the wavelet transform, where uneven higher harmonics are seen. The magnitude and number of the higher harmonics are controlled by the impact duration, ie. a short impact, or rapid change in velocity, results in more harmonics as the impact resembles a narrower impulse with a broader frequency content.

Figure 5.2.4(b) shows the restoring force and is clearly piecewise linear. The vertical dashed lines indicate the stops and the clearance distance can be determined quite accurate from the plot.

---

[1]For solving ODEs [5] is recommended. The system is automatically compiled into c-code, along with any event-detection. As a result, simulation is ten-fold faster than what can be achieved by matlab.
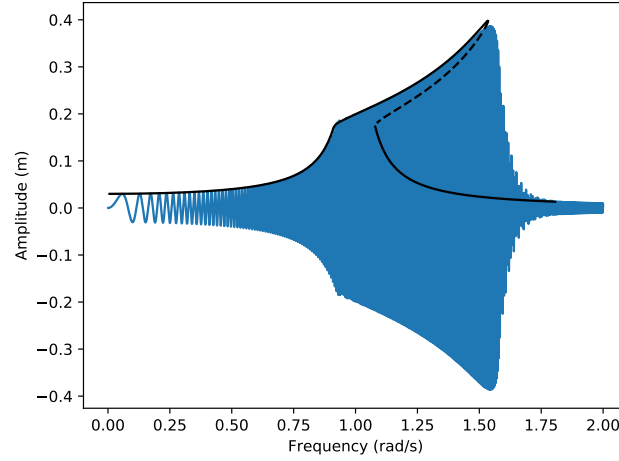
Figure 5.2.3: Forward sweep and HB for system (5.2.12). Sweep rate: 0.01Hz/min and $q = 0.03$. Dashed line indicates a unstable periodic solution.

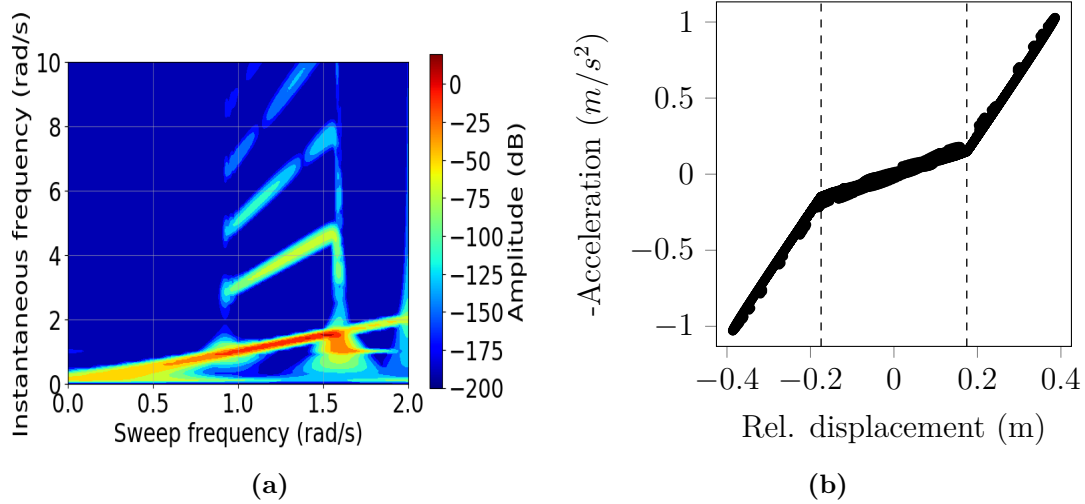(a)   (b)

Figure 5.2.4: Characterisation of system (5.2.12) using a forward sine sweep. **(a)**: Wavelet transform; **(b)**: Restoring force surface slice showing the restoring force. Dashed lines shows the location of the stops.

Estimation

The estimation of the of the system (5.2.12) is done by FNSI using cubic splines as basis functions.

Spline formulation   To resemble a linear piecewise function, a polynomial of sufficiently high order can be used. But as stated, high order polynomials shows oscillations around origin. Instead piecewise cubic polynomials (splines) are used, as introduced in [31]. Spline formulations are found in the handbook [4].

To find the cubic spline representation of the nonlinear force $f(x)$, let x be divided into R segments of arbitrary length defined by their abscissas x_k for $k = 1, ..., R + 1$. Each abscissa is associated with a ordinate f_k; together they define a knot (x_k, f_k).

Thus for the displacement x between knots k and $k + 1$, the corresponding spline approximation of f is given by

$$f(x) = (2t^3 - 3t^2 + 1)x_k + (-2t^3 + 3t^2)x_{k+1} + \\ (t^3 - 2t^2 + t)(x_{k+1} - x_k)x'_k + (t^3 - t^2)(x_{k+1} - x_k)x'_{k+1} \tag{5.2.13}$$

where t is the normalised displacement. To calculate the first order derivatives $x'_k = \frac{\partial x_k}{\partial x}$, $R+1$ constraints are needed. Forcing the cubic splines and the first two derivatives to be continuous across each interior knot gives $R - 1$ constraints:

$$\frac{x'_{k-}}{x_k - x_{k-1}} + 2 \left(\frac{1}{x_k - x_{k-1}} + \frac{1}{x_{k+1} - x_k} \right) x'_k + \frac{x'_{k+1}}{x_{k+1} - x_k} = \\ 3 \left(\frac{x_k - x_{k-1}}{(x_k - x_{k-1})^2} + \frac{x_{k+1} - x_k}{(x_{k+1} - x_k)^2} \right) \tag{5.2.14}$$

As the nonlinear force is required to be nonlinearizable, ie. is zero and have zero slope at equilibrium, this is also enforced for the segment containing the equilibrium point, giving the last two constraints. This is generally called the boundary condition for generic spline interpolation.

$$(t_0^3 - 2t_0^2 + t_0)(x_{k+1} - x_k)x'_k + (t_0^3 - t_0^2)(x_{k+1} - x_k)x'_{k+1} = \\ -(2t_0^3 - 3t_0^2 + 1)x_k - (-2t_0^3 + 3t_0^2)x_{k+1} \tag{5.2.15}$$

$$(3t_0^2 - 4t_0 + 1)(x_{k+1} - x_k)x'_k + (3t_0^2 - 2t_0)(x_{k+1} - x_k)x'_{k+1} = \\ 6(t_0 - t_0^2)(x_k + x_{k+1}) \tag{5.2.16}$$

where $t_0 = \frac{-x_k}{x_{k+1} - x_k}$.

Thus to summarise: Given the displacements $\mathbf{x}$ and knot placements x_k, the linear constraint equations (5.2.14)-(5.2.16) are solved(as a tridiagonal system) and used to find the basis function from eq. (5.2.13). The number of knots and their abscissas(x_k) should ideally be chosen by minimising the difference in some metric between the predictions of the nonlinear model and measured data. In reality it is still done by trial and error. In the current implementation the abscissas are distributed so the segments are divided into equal lengths.
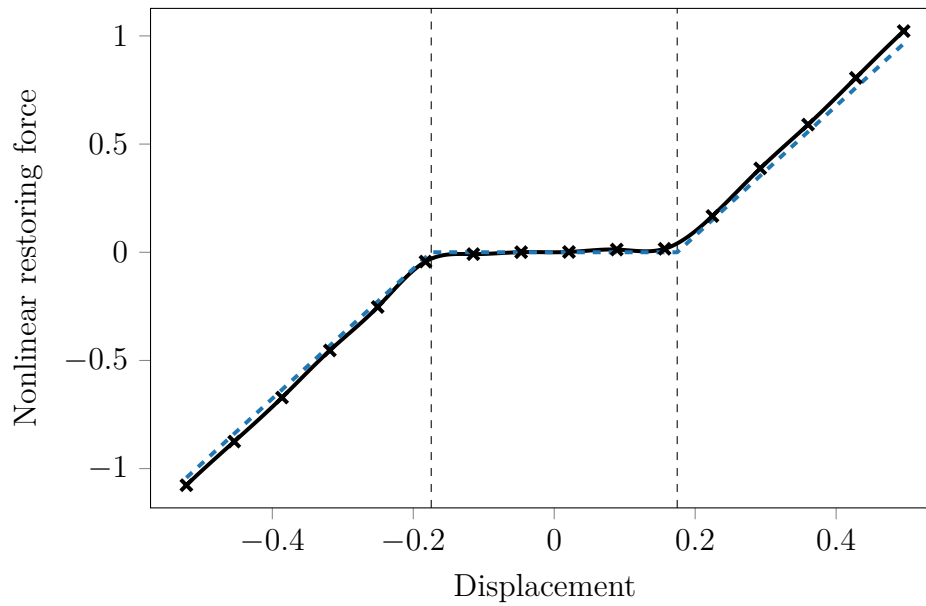
Figure 5.2.5: Nonlinear restoring force for the system (5.2.12). ———: Restoring force from splines estimation. Markers show knot locations; ----: Analytical restoring force

Results Using a low and high level multisine excitation's with RMS values of 0.005 and 0.2, the identified linear parameters are seen in table 5.2.1. At low level, where the stops are not activated, the expected linear parameters are obtained to high precision. At high level, without nonlinear basis functions, an increased natural frequency is obtained. Using the cubic splines, the correct linear frequency is obtained whereas the damping is estimated too low.

	Mode	Frequency (rad/s)	Damping ration (%)	Deviation from linear freq. (%)
Low	1	1	2.5	
High, lin	1	1.15	1.0	14.8
High, nonlin	1	0.995	1.6	0.5

Table 5.2.1: Estimated linear natural frequencies and damping ratios for the system (5.2.12) . **(upper)**: Low level, linear identification; **(middle)**: High level, linear identification; **(lower)**: High level, nonlinear identification.

Comparing the estimated nonlinear restoring force by the cubic splines to the exact in fig. 5.2.5, it is seen FNSI is able to capture the discontinuity using splines. 15 spline segments are specified for estimation, giving 16 basis functions(one for each knot ordinate). The high number of splines is chosen to show that FNSI is able to estimate many parameters. It have not been investigated why the damping estimation is wrong or if tweaking the number of splines would result in a better estimate.

Is is however expected that FNSI gives better estimates for natural frequencies than damping, as discussed in sec. 2.4.6.

Chapter 6

Conclusion

The focus of this report have been two-part. In the first part, methods for vibration-based identification of localised nonlinearities have been explored and validated. No assumption of the type of (localised) nonlinearity have been made, thus the models works equally well for boundary, geometric, etc. types of nonlinearities. Only stiffness have been treated; in theory the methods works just as well for damping, but in practice damping is much harder due to the much smaller magnitude and successful identification is still hard to obtain [29]. Another subject that have been neglected, is identification using noisy signals. The current FNSI implementation(in the vibration library) comes with noise-weighting functions implemented as described by [29](and working accordingly to the description), but have not been tested en real noisy data.

In the second part, methods for investigating the behaviour of identified nonlinear systems are treated. On the successful identification in part one, a model is built and used for determine stability, bifurcations and internal resonances. Where the methods in the first part requires some understanding and knowledge about nonlinear system in order to obtain a good identification, the methods here are easier to use and do not require as much knowledge (that said, implementation wise they cannot be said to be easier).

One substantial lack in connecting the two parts, is the need to create a model after identification is done. Current research are focused on eliminating this step, and use the state space system identified by FNSI directly by the numerical methods of the second part. Numerically this is easy when both the FNSI and HB methods are implemented, but as shown in [14], the FNSI method introduce spurious numerical artefacts, and as long as these artefacts are present, the state space formulation cannot be used directly. Preventing artefacts in the FNSI method will be a big step forward in the seamless integration of the two methodologies. Figure 6.0.1 shows the methodology.
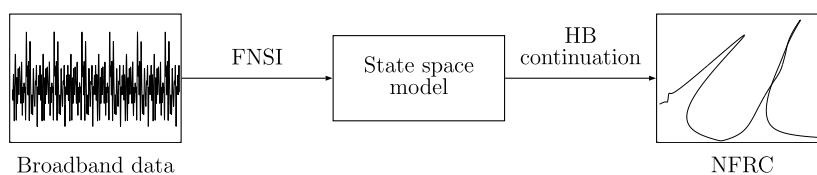

Figure 6.0.1: FNSI-HB continuation procedure

This also concludes that focus have been on the methods, and efficient implementation, and not application of them. The real limitations are not known and using them on real life structures could be a complete project of it own. For instance it have been assumed that a polynomial type of nonlinearity have a integer order. This might not be case in real applications. FNSI can(or might) help determine the polynomial order, but this have not been investigated.

Lacking in this thesis is the ability to track identified bifurcations. This might be a potential feature in aiding designs: find the system parameters where a bifurcation disappear. This could be exemplified as finding parameters that prevents flutter. Bifurcation tracking is described in [8].

As for the future of nonlinear system identification, progress have been made within localised lumped nonlinearities - FNSI is just one of multiple methods - but methods for distributed nonlinearities are still complicated and does not convoy any physical interpretation due their flexible nature (ie. black box models, where any combination of mathematical functions are mixed to model the system.)

References

[1]   N. P. van der Aa, H. G. ter Morsche, and R. R.M. Mattheij. "Computation of eigenvalue and eigenvector derivatives for a general complex-valued eigensystem". eng. In: *Electronic Journal of Linear Algebra* 16.1 (2007). ISSN: 10813810, 15379582. DOI: `10.13001/1081-3810.1203`.

[2]   Randall J Allemang. "The modal assurance criterion–twenty years of use and abuse". In: *Sound and vibration* 37.8 (2003), pp. 14–23.

[3]   Klaus-Jürgen Bathe and Gunwoo Noh. "Insight into an implicit time integration scheme for structural dynamics". eng. In: *Computers and Structures* 98-99 (2012), pp. 1–6. ISSN: 18792243, 00457949. DOI: `10.1016/j.compstruc.2012.01.009`.

[4]   Carl. de Boor. *A practical guide to splines.* eng. Vol. 27. Springer, 2001, 346 s. ISBN: 9780387953663.

[5]   et al. Clewley RH. *PyDSTool, a software environment for dynamical systems modeling.* 2007. URL: `http://pydstool.sourceforge.net`.

[6]   Robert D et al. Cook. *Concepts and applications of finite element analysis.* John Wiley & Sons, 2007.

[7]   RR Craig and MCC Bampton. "Coupling of substructures for dynamic analyses". eng. In: *Aiaa Journal* 6.7 (1968), pp. 1313–&. ISSN: 1533385x, 00011452. DOI: `10.2514/3.4741`.

[8]   T. Detroux et al. "The harmonic balance method for bifurcation analysis of large-scale nonlinear mechanical systems". eng. In: *Computer Methods in Applied Mechanics and Engineering* 296 (2015), pp. 18–38. ISSN: 18792138, 00457825. DOI: `10.1016/j.cma.2015.07.017`.

[9]   Thibaut Detroux. "Performace and robustness of nonlinear systems using bifurcation analysis". PhD thesis. Aerospace and Mechanical Engineering Department, Mar. 2016.

[10] Thibaut Detroux, Ludovic Renson, and Gaëtan Kerschen. "The Harmonic Balance Method for Advanced Analysis and Design of Nonlinear Mechanical Systems". eng. In: *springer* (2016). DOI: `10.1.1.839.5497`.

[11] A. Dhooge, W. Govaerts, and Yu. A. Kuznetsov. "MATCONT: A MATLAB Package for Numerical Bifurcation Analysis of ODEs". In: *ACM Trans. Math. Softw.* 29.2 (June 2003), pp. 141–164. ISSN: 0098-3500. DOI: `10.1145/779359.779362`.

[12] D.J. Ewins. *Modal testing: Theory, Practice and Application.* eng. Research Studies Press, 2000, 562 s.

[13] J.-C. GOLINVAL and M. LINK. "COST Action F3 Structural Dynamics (19972001)An European Co-Operation In The Field Of Science And Technology". In: *Mechanical Systems and Signal Processing* 17.1 (2003), pp. 3–7. ISSN: 0888-3270. DOI: http://dx.doi.org/10.1006/mssp.2002.1533.

[14] Etienne Gourc et al. "Obtaining Nonlinear Frequency Responses from Broadband Testing". eng. In: *Conference Proceedings of the Society for Experimental Mechanics Series* 1 (2016), pp. 219–227. ISSN: 21915652, 21915644. DOI: 10.1007/978-3-319-29739-2_20.

[15] Aurélien Grolet and Fabrice Thouverez. "On a new harmonic selection technique for harmonic balance method". In: *Mechanical Systems and Signal Processing* 30.Supplement C (2012), pp. 43–60. ISSN: 0888-3270. DOI: https://doi.org/10.1016/j.ymssp.2012.01.024.

[16] Michael Blom Hermansen. "Vibration-based identification of beam boundary models". MA thesis. Technical university of Denmark, 2017.

[17] Jon Juel Thomsen. *Vibrations and stability : advanced theory, analysis, and tools.* Springer, 2003, 404 s. ISBN: 9783540401407.

[18] G Kerschen et al. "Past, present and future of nonlinear system identification in structural dynamics". eng. In: *Mechanical Systems and Signal Processing* 20.3 (2006), pp. 505–592. ISSN: 10961216, 08883270. DOI: 10.1016/j.ymssp.2005.04.008.

[19] G. Kerschen et al. "Nonlinear normal modes, Part I: A useful framework for the structural dynamicist". eng. In: *Mechanical Systems and Signal Processing* 23.1 (2009), pp. 170–194. ISSN: 10961216, 08883270. DOI: 10.1016/j.ymssp.2008.04.002.

[20] T. C. Kim, T. E. Rook, and R. Singh. "Effect of smoothening functions on the frequency response of an oscillator with clearance non-linearity". In: *Journal of Sound Vibration* 263 (June 2003), pp. 665–678. DOI: 10.1016/S0022-460X(02)01469-4.

[21] Knud Abildgaard Kragh. "Detection, Localization, and Characterization of Structural Nonlinearities from Dynamic Measurements". MA thesis. DTU Mechanical Engineering, 2010.

[22] Steen Krenk. *Non-linear modeling and analysis of solids and structures.* Cambridge University Press, 2009.

[23] Yuri A Kuznetsov. *Elements of applied bifurcation theory.* Vol. 112. Springer Science & Business Media, 2013.

[24] V Lenaerts, G Kerschen, and JC Golinval. "Identification of a continuous structure with a geometrical non-linearity. Part II: Proper orthogonal decomposition". eng. In: *Journal of Sound and Vibration* 262.4 (2003), pp. 907–919. ISSN: 10958568, 0022460x. DOI: 10.1016/S0022-460X(02)01132-X.

[25] S. Marchesiello and L. Garibaldi. "A time domain approach for identifying nonlinear vibrating structures by subspace methods". eng. In: *Mechanical Systems and Signal Processing* 22.1 (2008), pp. 81–101. ISSN: 10961216, 08883270. DOI: 10.1016/j.ymssp.2007.04.002.

[26]   S. F. Masri and T. K. Caughey. "A nonparametric identification technique for nonlinear dynamic problems". eng. In: *Transactions of the Asme. Journal of Applied Mechanics* 46.2 (1979), pp. 433–47, 433–447. ISSN: 15289036, 00218936. DOI: 10.1115/1.3424568.

[27]   Paw Møller. *Vibration code, python.* Oct. 2017. URL: https://github.com/pawsen/vib.

[28]   Ali H Nayfeh and Balakumar Balachandran. *Applied nonlinear dynamics: analytical, computational and experimental methods.* John Wiley & Sons, 2008.

[29]   J. P. Noel and G. Kerschen. "Frequency-domain subspace identification for nonlinear mechanical systems". eng. In: *Mechanical Systems and Signal Processing* 40.2 (2013), pp. 701–717. ISSN: 10961216, 08883270. DOI: 10.1016/j.ymssp.2013.06.034.

[30]   J. P. Noel, S. Marchesiello, and G. Kerschen. "Subspace-based identification of a nonlinear spacecraft in the time and frequency domains". eng. In: *Mechanical Systems and Signal Processing* 43.1-2 (2014), pp. 217–236. ISSN: 10961216, 08883270. DOI: 10.1016/j.ymssp.2013.10.016.

[31]   J. P. Noel et al. "Grey-box identification of a non-linear solar array structure using cubic splines". eng. In: *International Journal of Non-linear Mechanics* 67 (2014), pp. 106–119. ISSN: 18785638, 00207462. DOI: 10.1016/j.ijnonlinmec.2014.08.012.

[32]   J. P. Noël and G. Kerschen. "Nonlinear system identification in structural dynamics: 10 more years of progress". eng. In: *Mechanical Systems and Signal Processing* 83 (2016), pp. 2–35. ISSN: 10961216, 08883270. DOI: 10.1016/j.ymssp.2016.07.020.

[33]   Jean-Philippe Noël, Stefano Marchesiello, and Gaëtan Kerschen. "Time-and frequency-domain subspace identification of a nonlinear spacecraft". In: *Proceedings of the ISMA International Conference on Noise and Vibration Engineering 2012.* 2012.

[34]   P. van Overschee and B. de Moor. *Subspace identification for linear systems. Theory, implementation, applications.* eng. Kluwer, 1996, 254 s. ISBN: 0792397177.

[35]   M. Peeters et al. "Nonlinear normal modes, Part II: Toward a practical computation using numerical continuation techniques". eng. In: *Mechanical Systems and Signal Processing* 23.1 (2009), pp. 195–216. ISSN: 10961216, 08883270. DOI: 10.1016/j.ymssp.2008.04.003.

[36]   Rosenberg. "On nonlinear vibrations of systems with many degrees of freedom". und. In: *Advances in Applied Mechanics* (1966), pp. 155–242, 155–242.

[37]   Geraldo F. de S. Rebouças, Ilmer F. Santos, and Jon Juel Thomsen. "Validation of Vibro-Impact Force Models by Numerical Simulation, Perturbation Methods and Experiments". Sept. 7, 2017.

[38]   Bonnie A. Steves et al. *Chaotic Worlds: From Order to Disorder in Gravitational N-Body Dynamical Systems, CHAOTIC WORLDS.* eng. Vol. 227. Springer Netherlands, 2006, xi, 342 s. : ISBN: 1402047061, 1402047045, 128071641x, 1402047053, 9786610716418, 9781402047046.

[39] A. F. Vakakis and R. H. Rand. "Normal modes and global dynamics of a two-degree-of-freedom non-linear system. I. Low energies". eng. In: *International Journal of Non-linear Mechanics* 27.5 (1992), pp. 861–74, 861–874. ISSN: 18785638, 00207462. DOI: 10.1016/0020-7462(92)90040-E.

[40] Alexander F Vakakis et al. *Nonlinear targeted energy transfer in mechanical and structural systems*. eng. Vol. 156. Springer Science & Business Media, 2008, pp. 1–1033. ISBN: 9781402091254. DOI: http://dx.doi.org/10.1007/978-1-4020-9130-8.

[41] K. Worden. "Data processing and experiment design for the restoring force surface method, part I: integration and differentiation of measured time data". eng. In: *Mechanical Systems and Signal Processing* 4.4 (1990), pp. 295–319. ISSN: 10961216, 08883270. DOI: 10.1016/0888-3270(90)90010-I.

[42] Keith Worden and Geoffrey R Tomlinson. *Nonlinearity in structural dynamics: detection, identification and modelling*. CRC Press, 2000.

Appendix A

Periodic solution

A.1 HB

The derivation of the equations of motion in frequency domain continues from where it was left in section 3.2.2.

The operators $\boldsymbol{\nabla}$ and $\boldsymbol{\nabla}^2$ used in expressing velocities and accelerations are given as

$$
\boldsymbol{\nabla} = \begin{bmatrix} \mathbf{0} & & & & \\ & \ddots & & & \\ & & \boldsymbol{\nabla}_k & & \\ & & & \ddots & \\ & & & & \boldsymbol{\nabla}_{N_H} \end{bmatrix}, \quad
\boldsymbol{\nabla}^2 = \begin{bmatrix} \mathbf{0} & & & & \\ & \ddots & & & \\ & & \boldsymbol{\nabla}_k^2 & & \\ & & & \ddots & \\ & & & & \boldsymbol{\nabla}_{N_H}^2 \end{bmatrix} \tag{A.1.1}
$$

with

$$
\boldsymbol{\nabla}_k = \begin{bmatrix} 0 & -k\omega \\ k\omega & 0 \end{bmatrix}, \quad
\boldsymbol{\nabla}_k^2 = \begin{bmatrix} -(k\omega)^2 & 0 \\ 0 & -(k\omega)^2 \end{bmatrix} \tag{A.1.2}
$$

Substitute eqs. (3.2.17)-(3.2.18) and (3.2.24)-(3.2.25) into the EOM (3.2.1) to get

$$
\mathbf{M}((Q(t)\boldsymbol{\nabla}^2) \otimes \mathbb{I}_n)\mathbf{z} + \mathbf{C}((Q(t)\boldsymbol{\nabla}) \otimes \mathbb{I}_n)\mathbf{z} + \mathbf{K}((Q(t) \otimes \mathbb{I}_n)\mathbf{z} = (\mathbf{Q}(t) \otimes I_n)\mathbf{b} \tag{A.1.3}
$$

Using the mixed-product product of the Kronecker product $(\mathbf{A} \otimes \mathbf{B}) = (\mathbf{C} \otimes \mathbf{D}) = (\mathbf{AC}) \otimes (\mathbf{BD})$ gives

$$
\begin{aligned}
\mathbf{M}((Q(t)\boldsymbol{\nabla}^2) \otimes \mathbb{I}_n) &= (1 \otimes \mathbf{M})((\mathbf{Q}(t)\boldsymbol{\nabla}^2) \otimes I_n) = (\mathbf{Q}(t)\boldsymbol{\nabla}^2) \otimes \mathbf{M} \\
\mathbf{C}((Q(t)\boldsymbol{\nabla}) \otimes \mathbb{I}_n) &= (1 \otimes \mathbf{C})((\mathbf{Q}(t)\boldsymbol{\nabla}) \otimes I_n) = (\mathbf{Q}(t)\boldsymbol{\nabla}) \otimes \mathbf{C} \\
\mathbf{K}(Q(t) \otimes \mathbb{I}_n) &= (1 \otimes \mathbf{K})(\mathbf{Q}(t) \otimes I_n) = \mathbf{Q}(t) \otimes \mathbf{K}
\end{aligned} \tag{A.1.4}
$$

Substituting these into eq. (A.1.3) gives

$$
((\mathbf{Q}(t)\boldsymbol{\nabla}^2) \otimes \mathbf{M})\mathbf{z} + ((\mathbf{Q}(t)\boldsymbol{\nabla}) \otimes \mathbf{C})\mathbf{z} + (\mathbf{Q}(t) \otimes \mathbf{K})\mathbf{z} = (\mathbf{Q}(t) \otimes I_n)\mathbf{b} \tag{A.1.5}
$$

In order to remove the time dependency and to obtain an expression relating the different Fourier coefficients, a Galerkin procedure projects eq. (A.1.5) on the orthogonal trigonometric basis $\mathbf{Q}(t)$

$$
\left(\left(\frac{2}{T}\int_0^T \mathbf{Q}^T(t)\mathbf{Q}(t)\,\mathrm{d}t\boldsymbol{\nabla}^2\right)\otimes\mathbf{M}\right)\mathbf{z}+\left(\left(\frac{2}{T}\int_0^T \mathbf{Q}^T(t)\mathbf{Q}(t)\,\mathrm{d}t\boldsymbol{\nabla}\right)\otimes\mathbf{C}\right)\mathbf{z}
$$
$$
\left(\left(\frac{2}{T}\int_0^T \mathbf{Q}^T(t)\mathbf{Q}(t)\,\mathrm{d}t\right)\otimes\mathbf{K}\right)\mathbf{z}=\left(\left(\frac{2}{T}\int_0^T \mathbf{Q}^T(t)\mathbf{Q}(t)\,\mathrm{d}t\right)\otimes I_n\right)\mathbf{b}
\tag{A.1.6}
$$

where $T=2\pi/\omega$ is the period of the external force.

Using that

$$
\frac{2}{T}\int_0^T \mathbf{Q}^T(t)\mathbf{Q}(t)\,\mathrm{d}t = I_{2N_H+1}
\tag{A.1.7}
$$

the equations of motion expressed in frequency domain are

$$
(\boldsymbol{\nabla}^2\otimes\mathbf{M})\mathbf{z}+(\boldsymbol{\nabla}\otimes\mathbf{C})\mathbf{z}+(\mathbb{I}_{2N_H}\otimes\mathbf{K})\mathbf{z}=(\mathbb{I}_{2N_H}\otimes\mathbb{I}_n)\mathbf{b}
\tag{A.1.8}
$$

or in more compact form

$$
\mathbf{H}(\mathbf{z},\omega)=\mathbf{A}(\omega)\mathbf{z}-\mathbf{b}(\mathbf{z})=\mathbf{0}
\tag{A.1.9}
$$

where $\mathbf{A}$ describes the linear dynamics

$$
\mathbf{A}=\boldsymbol{\nabla}^2\otimes\mathbf{M}+\boldsymbol{\nabla}\otimes\mathbf{C}+\mathbb{I}_{2N_H}\otimes\mathbf{K}
$$
$$
=\begin{bmatrix}
\mathbf{K} & & & & & \\
& \mathbf{K}-\omega^2\mathbf{M} & -\omega\mathbf{C} & & & \\
& \omega\mathbf{C} & \mathbf{K}-\omega^2\mathbf{M} & & & \\
& & & \ddots & & \\
& & & & \mathbf{K}-(N_H\omega)^2\mathbf{M} & -N_H\omega\mathbf{C} \\
& & & & N_H\omega\mathbf{C} & \mathbf{K}-(N_H\omega)^2\mathbf{M}
\end{bmatrix}
\tag{A.1.10}
$$

A.1.1   Stability

To find the stability of a periodic solution, a method known as *Hills method* is used to estimate the Floquet exponents.

A periodic solution $\mathbf{x}(t)$ satisfying the eom eq. (3.2.1) is perturbed by an exponential decay

$$
\mathbf{p}(t)=\mathbf{x}(t)+e^{\lambda t}\mathbf{s}(t)
\tag{A.1.11}
$$

inserting this into the eom eq. (3.2.1),

$$
\mathbf{M}\ddot{\mathbf{x}}+\mathbf{C}\dot{\mathbf{x}}+\mathbf{K}\mathbf{x}+(\lambda^2\mathbf{M}\mathbf{s}+\lambda(2\mathbf{M}\dot{\mathbf{s}})+\mathbf{M}\ddot{\mathbf{s}}+\mathbf{C}\dot{\mathbf{s}}+\mathbf{K}\mathbf{s})e^{\lambda t}=\mathbf{f}(\mathbf{p},\dot{\mathbf{p}},\omega,t)
\tag{A.1.12}
$$

Following the outline of section 3.2.2, the solution and perturbation are approximated by Fourier series truncated to N_H-th order, i.e. $\mathbf{x}(t)=(\mathbf{Q}(t)\otimes I_n)\mathbf{z}$ and $\mathbf{s}(t)=(\mathbf{Q}(t)\otimes I_n)\mathbf{u}$, where $\mathbf{z}$ and $\mathbf{u}$ contains the Fourier coefficients of $\mathbf{x}$ and $\mathbf{s}$, respectively. Following section B.1, a Galerkin is used to obtain

$$\mathbf{Az} + (\boldsymbol{\Delta}_2\lambda^2 + \boldsymbol{\Delta}_1\lambda + \mathbf{A})e^{\lambda t}\mathbf{u} = \mathbf{b}(\mathbf{z} + e^{\lambda t}\mathbf{u}) \tag{A.1.13}$$

where $\boldsymbol{\Delta}$ are matrices describing the linear dynamics similar to $\mathbf{A}$ in eq. (A.1.10) and λ are Hills coefficients.

$$\boldsymbol{\Delta}_1 = \boldsymbol{\nabla} \otimes 2\mathbf{M} + \mathbb{I}_{2N_H+1} \otimes \mathbf{C}$$

$$= \begin{bmatrix} \mathbf{C} & & & & & \\ & \mathbf{C} & -\omega\mathbf{M} & & & \\ & 2\omega\mathbf{M} & \mathbf{C} & & & \\ & & & \ddots & & \\ & & & & \mathbf{C} & -2N_H\omega\mathbf{M} \\ & & & & 2N_H\omega\mathbf{M} & \mathbf{C} \end{bmatrix} \tag{A.1.14}$$

$$\boldsymbol{\Delta}_2 = \mathbb{I}_{2N_H+1} \otimes \mathbf{M}$$

The right-hand side of eq. (A.1.13) is evaluated through a Taylor series expansion around the solution $\mathbf{z}$

$$\mathbf{b}(\mathbf{z} + e^{\lambda t}\mathbf{u}) = \mathbf{b}(\mathbf{z}) + \left.\frac{\partial \mathbf{b}}{\partial \mathbf{z}}\right|_z (e^{\lambda t}\mathbf{u}) \tag{A.1.15}$$

Since $\mathbf{Az} - \mathbf{b}(\mathbf{z}) = \mathbf{0}$ by definition and given that

$$\mathbf{A} - \left.\frac{\partial \mathbf{b}}{\partial \mathbf{z}}\right|_z = \mathbf{h_z} \tag{A.1.16}$$

eq. (A.1.13) is rewritten into the quadratic eigenvalue problem

$$\left(\boldsymbol{\Delta}_2\lambda^2 + \boldsymbol{\Delta}_1\lambda + \mathbf{H_z}\right)e^{\lambda t}\mathbf{u} = \mathbf{0} \tag{A.1.17}$$

A.1.2   NNM

Following the method above, NNMs can be computed using HB in the following way:

$$\mathbf{h}_{ham}(\mathbf{z}, \omega) = (\boldsymbol{\nabla}^2 \otimes \mathbf{M})\mathbf{z} + (I_{2N_H+1} \otimes \mathbf{K})\mathbf{z} + \mathbf{b}_{nl} = \mathbf{0} \tag{A.1.18}$$

where $\mathbf{b}_{nl}$ is the vector of the Fourier coefficients of the nonlinear forces, defined as

$$\mathbf{f}_{nl}(\mathbf{x}) = (\mathbf{Q}(t) \otimes I_n)\mathbf{b}_{nl} \tag{A.1.19}$$

The phase condition for frequency-domain methods are often to set a Fourier coefficient of a DOF to zero. Doing this, the equation for a NNM motion is

$$\mathbf{h}_{NNM} = \begin{bmatrix} \mathbf{h}_{ham}(\mathbf{z}, \omega) \\ z_i \end{bmatrix} = \mathbf{0} \tag{A.1.20}$$

where z_i is a component of $\mathbf{z}$.

Appendix B

Continuation

B.1 Harmonic balance

Figure B.1.1 shows the influence of the included number of harmonics N_H, The time discretisation N and the optimal number of iterations I_{opt}. Fig. B.1.1a shows super-harmonic resonances at low frequencies are not captured for $N_H = 3$ and $N_H = 1$. This is expected as they possesses multiple frequency content, but shows that care should be taken when the number of harmonics is selected. Especially for more complicated and rich vibrations that this simple example. For systems with few DOFs, it is not a problem to include a high number of harmonics - remember that system matrices $\mathbf{A}$ in the HB method, eq (A.1.10), is of size $(2N_H + 1)n \times (2N_H + 1)n$ and the sparse Fourier operator $\mathbf{\Gamma}$ of size $nH \times (2N_H + 1)n$ where n is number of DOFs. But for large systems it will become a problem. To solve this, there excits ways to automatically adopt the number of harmonics for each DOF [15].

Fig. B.1.1b shows that the solution is inaccurate around the peak for lower N. This is due to aliasing effects.-- Det slap du nu lidt for nemt om ved –

Fig. B.1.1c shows that the peak is "cut short" or truncated for higher values of I_{opt}. Setting a high value of I_{opt} allows for taking larger steps, since more Newton iterations are allowed to correct the guess. Thus resolution is decreased. Of course one can use a `max_step` parameter to prevent too large steps.
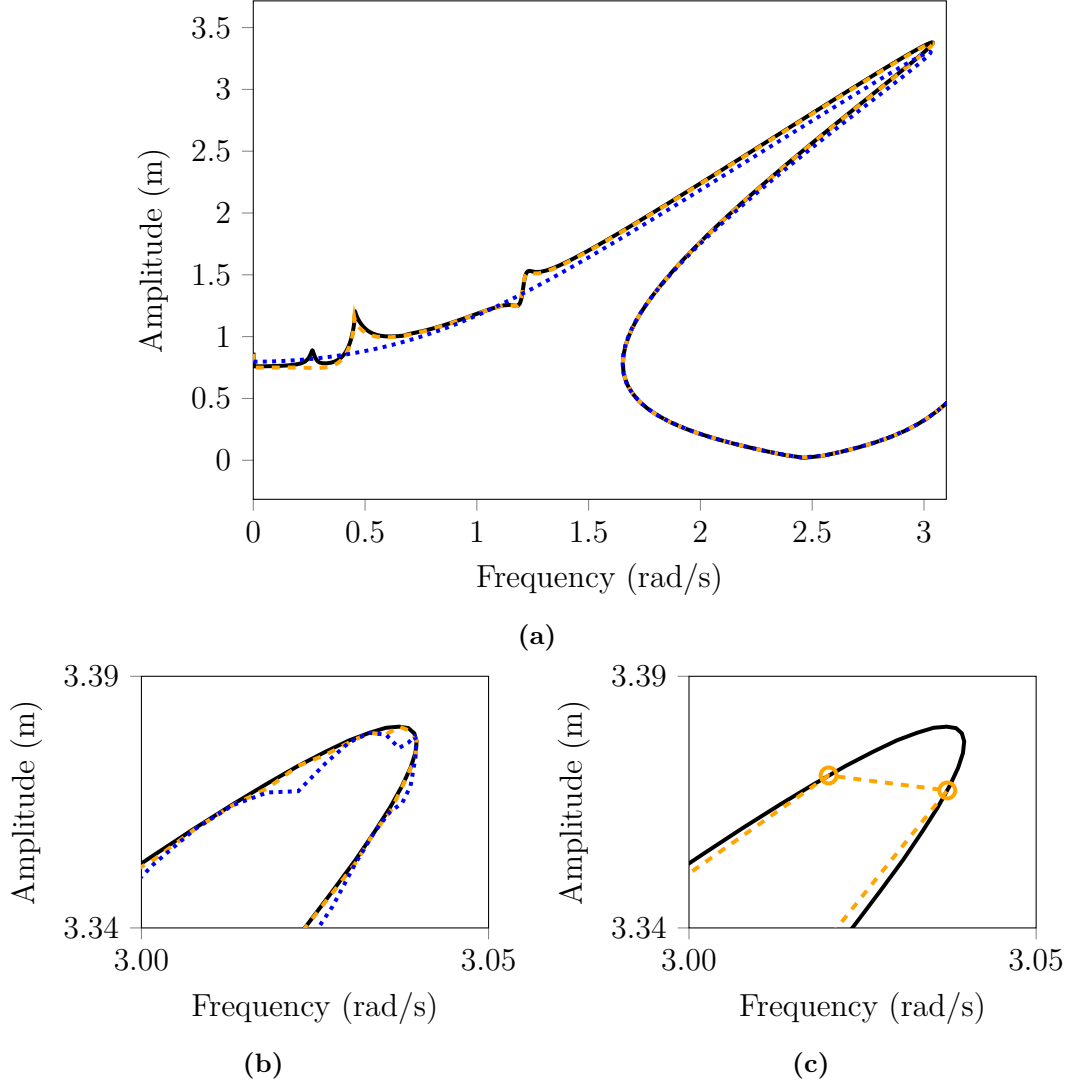
(a)

(b)

(c)

Figure B.1.1: NRFC of the coupled duffing system for x_1 with $f = 2$N. Influence of HB and continuation parameters, compared to $N_H = 5, N = 512, I_{opt} = 3$ (——). Stability is not shown. **(a)** (- - - -) $N_H = 3$; (·········) $N_H = 1$; **(b)** (- - - -) $N = 128$; (·········) $N = 64$; **(c)** (- - - -) $I_{opt} = 5$;

Appendix C

Newmark integration

Newmarks time integration is used for solving the initial value problem defined by the EOM,

$$\mathbf{M}\ddot{\mathbf{x}}(t) + \mathbf{C}_v\dot{\mathbf{x}}(t) + \mathbf{K}\mathbf{x}(t) + \mathbf{f}_{nl}\left(\mathbf{x}(t), \dot{\mathbf{x}}(t)\right) = \mathbf{p}(t)$$
$$\mathbf{z}_0 = \begin{bmatrix} \mathbf{x}(0) \\ \dot{\mathbf{x}}(0) \end{bmatrix} = \begin{bmatrix} \mathbf{x}_0 \\ \dot{\mathbf{x}}_0 \end{bmatrix}$$

(C.0.1)

where $\mathbf{z}_0$ are the initial conditions. $\mathbf{z}$ is the state vector.

The associated sensitivity problem, ie. how sensitive the current motion is to the initial conditions, is given by

$$\mathbf{M}\frac{\partial\ddot{\mathbf{x}}(t)}{\partial\mathbf{z}_0} + \mathbf{C}_v\frac{\partial\dot{\mathbf{x}}(t)}{\partial\mathbf{z}_0} + \mathbf{K}\frac{\partial\mathbf{x}(t)}{\partial\mathbf{z}_0} + \frac{\partial\mathbf{f}_{nl}}{\partial\mathbf{x}}\bigg|_{\mathbf{x}(t)}\frac{\partial\mathbf{x}(t)}{\partial\mathbf{z}_0} + \frac{\partial\mathbf{f}_{nl}}{\partial\dot{\mathbf{x}}}\bigg|_{\dot{\mathbf{x}}(t)}\frac{\partial\dot{\mathbf{x}}(t)}{\partial\mathbf{z}_0} = \mathbf{0}$$
$$\begin{bmatrix} \frac{\partial\mathbf{x}(0)}{\partial\mathbf{z}_0} \\ \frac{\partial\dot{\mathbf{x}}(0)}{\partial\mathbf{z}_0} \end{bmatrix} = \mathbf{I}$$

(C.0.2)

where $\frac{\partial\ddot{\mathbf{x}}(t)}{\partial\mathbf{z}_0}$ is implied to mean $\frac{\mathrm{d}^2}{\mathrm{d}t^2}\left[\frac{\partial\mathbf{x}(t)}{\partial\mathbf{z}_0}\right]$

C.1 Solving EOM

The solution of the EOM is done by an implicit nonlinear Newmark scheme. Description of the method can be found in Krenk [22].

Here follows a more throughout derivation. The algorithm itself, for fixed time step, is shown in pseudo-code in Algorithm 1.

The residual of the EOM eq. (C.0.1) is

$$\mathbf{r}(\mathbf{x}) = \mathbf{M}\ddot{\mathbf{x}}(t) + \mathbf{C}\dot{\mathbf{x}}(t) + \mathbf{K}\mathbf{x}(t) + \mathbf{f}_{nl}\left(\mathbf{x}(t), \dot{\mathbf{x}}(t)\right) - \mathbf{p}(t) = 0 \qquad (\text{C.1.1})$$

From time t to $t + h$, a Taylor series expansion of the velocity and displacement with respect to h gives

$$\dot{\mathbf{x}}_{t+h} = \dot{\mathbf{x}}_t + (1 - \gamma)h\ddot{\mathbf{x}}_t + \gamma h\ddot{\mathbf{x}}_{t+h}$$
$$\mathbf{x}_{t+h} = \mathbf{x}_t + \dot{\mathbf{x}}_t + (\frac{1}{2} - \beta)h^2\ddot{\mathbf{x}}_t + \beta h^2\ddot{\mathbf{x}}_{t+h}$$

(C.1.2)

where γ and β are weighting constants. Often $\gamma = \frac{1}{2}, \beta = \frac{1}{4}$ is chosen, which is the Average Acceleration method. This gives a scheme that is unconditionally stable and converges as $\mathcal{O}(h^2)$

This can be rewritten as

$$
\begin{aligned}
\dot{\mathbf{x}}_{t+h} &= \dot{\mathbf{x}}^*_{t+h} + \gamma h \ddot{\mathbf{x}}_{t+h} \\
\mathbf{x}_{t+h} &= \mathbf{x}^*_{t+h} + \beta h^2 \ddot{\mathbf{x}}_{t+h}
\end{aligned}
\tag{C.1.3}
$$

$$
\begin{aligned}
\dot{\mathbf{x}}^*_{t+h} &= \dot{\mathbf{x}}_t + (1 - \gamma)h \ddot{\mathbf{x}}_t \\
\mathbf{x}^*_{t+h} &= \mathbf{x}_t + \dot{\mathbf{x}}_t + (\frac{1}{2} - \beta)h^2 \ddot{\mathbf{x}}_t
\end{aligned}
\tag{C.1.4}
$$

where $(^*)$ denotes prediction. The prediction depends on the previous time step t and implies the prediction $\ddot{\mathbf{x}}^*_{t+h} = 0$.

Rewriting eq. (C.1.3) again

$$
\begin{aligned}
\ddot{\mathbf{x}}_{t+h} &= \frac{1}{\beta h^2}(\mathbf{x}_{t+h} - \mathbf{x}^*_{t+h}) \\
\dot{\mathbf{x}}_{t+h} &= \dot{\mathbf{x}}^*_{t+h} \frac{\gamma}{\beta h}(\mathbf{x}_{t+h} - \mathbf{x}^*_{t+h})
\end{aligned}
\tag{C.1.5}
$$

Substituting this into the residual eq. (C.1.1), the equation is only expressed in terms of $\mathbf{x}_{t+h}$. Due to the nonlinear stiffness and dissipation, the residual equation have to be solved iteratively by Newton-Raphson iterations.

$$
\mathbf{r}(\mathbf{x}^k_{t+h}) + \mathbf{S}(\mathbf{x}^k_{t+h})\mathbf{\Delta x} = 0
\tag{C.1.6}
$$

The iteration matrix $\mathbf{S}$, also called the tangent stiffness, is given by

$$
\mathbf{S}(\mathbf{x}^k_{t+h}) = \left[\frac{d\mathbf{r}}{d\mathbf{x}}\right]_{\mathbf{x}^k_{t+h}} = \frac{1}{\beta h^2}\mathbf{M} + \frac{\gamma}{\beta h}\mathbf{C} + \mathbf{K} + \frac{\partial \mathbf{f}_{nl}}{\partial \mathbf{x}} + \frac{\gamma}{\beta h}\frac{\partial \mathbf{f}_{nl}}{\partial \dot{\mathbf{x}}}
\tag{C.1.7}
$$

Thus the correction is found by solving eq. (C.1.6)

$$
\Delta \mathbf{x}^k_{t+h} = -\mathbf{S}(\mathbf{x}^k_{t+h})^{-1}\mathbf{r}(\mathbf{x}^k_{t+h})
\tag{C.1.8}
$$

and updating the state variables

$$
\begin{aligned}
\mathbf{x}^{k+1}_{t+h} &= \mathbf{x}^k_{t+h} + \Delta \mathbf{x}^k_{t+h} \\
\dot{\mathbf{x}}^{k+1}_{t+h} &= \dot{\mathbf{x}}^k_{t+h} + \frac{\gamma}{\beta h}\Delta \mathbf{x}^k_{t+h} \\
\ddot{\mathbf{x}}^{k+1}_{t+h} &= \ddot{\mathbf{x}}^k_{t+h} + \frac{1}{\beta h^2}\Delta \mathbf{x}^k_{t+h}
\end{aligned}
\tag{C.1.9}
$$

The Newton iterations are carried out until some norm of residual value is below a given tolerance. Cook [6] have different examples of norms that can be used.

C.2 Sensitivity Equations

At the end of each time step, the sensitivity matrix $\left[\frac{\partial \mathbf{x}}{\partial \mathbf{z}_0}\right]$ is found by solving eq. (C.0.2). Using Newmarks scheme given by eq. (C.1.5), at time step $t + h$ one have

$$\left[\frac{\partial \ddot{\mathbf{x}}}{\partial \mathbf{z}_0}\right]_{t+h} = \frac{1}{\beta h^2}\left(\left[\frac{\partial \mathbf{x}}{\partial \mathbf{z}_0}\right]_{t+h} - \left[\frac{\partial \mathbf{x}}{\partial \mathbf{z}_0}\right]_{t+h}^*\right) \tag{C.2.1}$$

$$\left[\frac{\partial \dot{\mathbf{x}}}{\partial \mathbf{z}_0}\right]_{t+h} = \left[\frac{\partial \dot{\mathbf{x}}}{\partial \mathbf{z}_0}\right]_{t+h}^* + \frac{\gamma}{\beta h^2}\left(\left[\frac{\partial \mathbf{x}}{\partial \mathbf{z}_0}\right]_{t+h} - \left[\frac{\partial \mathbf{x}}{\partial \mathbf{z}_0}\right]_{t+h}^*\right) \tag{C.2.2}$$

the predictions are given as (* denote prediction)

$$\left[\frac{\partial \dot{\mathbf{x}}}{\partial \mathbf{z}_0}\right]_{t+h}^* = \left[\frac{\partial \dot{\mathbf{x}}}{\partial \mathbf{z}_0}\right]_t + (1-\gamma)h\left[\frac{\partial \ddot{\mathbf{x}}}{\partial \mathbf{z}_0}\right]_t \tag{C.2.3}$$

$$\left[\frac{\partial \mathbf{x}}{\partial \mathbf{z}_0}\right]_{t+h}^* = \left[\frac{\partial \mathbf{x}}{\partial \mathbf{z}_0}\right]_t^* h\left[\frac{\partial \dot{\mathbf{x}}}{\partial \mathbf{z}_0}\right]_t + h^2(\frac{1}{2} - \beta)\left[\frac{\partial \ddot{\mathbf{x}}}{\partial \mathbf{z}_0}\right]_t \tag{C.2.4}$$

By rearranging and substitution eqs. (C.2.1) and (C.2.2) into the linear sensitivity eq. (C.0.2), the sensitivity acceleration matrix at time $t + h$ is found as

$$\frac{1}{\beta h^2}\left[\frac{1}{\beta h^2}\mathbf{M} + \frac{\gamma}{\beta h}\mathbf{C} + \mathbf{K} + \frac{\partial \mathbf{f}_{nl}}{\partial \mathbf{x}} + \frac{\gamma}{\beta h}\frac{\partial \mathbf{f}_{nl}}{\partial \dot{\mathbf{x}}}\right]\left[\frac{\partial \ddot{\mathbf{x}}}{\partial \mathbf{z}_0}\right]_{t+h} =$$

$$-\left(\mathbf{K} + \frac{\partial f_{nl}}{\partial \mathbf{x}}\right)\left[\frac{\partial \mathbf{x}}{\partial \mathbf{z}_0}\right]_{t+h}^* - \left(\mathbf{C} + \frac{\partial f_{nl}}{\partial \dot{\mathbf{x}}}\right)\left[\frac{\partial \dot{\mathbf{x}}}{\partial \mathbf{z}_0}\right]_{t+h}^* \tag{C.2.5}$$

from where the sensitivity matrix is found by (C.2.1).

Thus by marching in time, the current motion and its sensitivity with respect to initial conditions are found.

C.3 Algorithm

C.3.1 Summary

The Newmark-beta method used for implicit time integration was developed in 1959. Today it is one of the most widely used solvers for dynamics systems, and for most problems it performs reasonable well. For problems with very stiff and very flexible parts, i.e. where eigenvalues are very separated, it performs poorly due to lack of high frequency numerical damping. Interested readers are referred to [3], which also suggest one alternative (it should be noted that what Bathe calls the Newmark trapezoidal rule is mostly known as the Newmark average acceleration method).

Algorithm 1: Nonlinear Newmark algorithm

---

1 Initial conditions, $\mathbf{x}_0, \dot{\mathbf{x}}_0$.

$A_1 = (1 - \gamma)h, \quad B_1 = (\frac{1}{2} - \beta)h^2, \quad A_2 = \frac{1}{\beta h^2}, \quad B_2 = \frac{\gamma}{\beta h}$

$\mathbf{S}_{lin} = \mathbf{K} + \frac{\gamma}{\beta h}\mathbf{C} + \frac{\beta}{h^2}\mathbf{M}$

$\ddot{\mathbf{x}}_0 = \mathbf{M}^{-1}(\mathbf{p}_0 - \mathbf{C}\dot{\mathbf{x}}_0 - \mathbf{K}\mathbf{x}_0 - \mathbf{f}_{nl}(\mathbf{u}_0, \dot{\mathbf{u}}_0))$

if *sensitivity* **then**

    $\mathbf{V} = [\mathbf{I}, \mathbf{0}; \mathbf{0}, \mathbf{0}], \dot{\mathbf{V}} = [\mathbf{0}, \mathbf{0}; \mathbf{0}, \mathbf{I}]$

    $\ddot{\mathbf{V}} = -\mathbf{M}^{-1}\left((\mathbf{C} + \mathbf{f}_{nl,\dot{\mathbf{x}}})\dot{\mathbf{V}} + (\mathbf{K} + \mathbf{f}_{nl,\mathbf{x}})\mathbf{V}\right)$

2 for $n \leftarrow 0$ **to** nt **do**

3   Prediction step (time integration):

    $\dot{\mathbf{x}}_{n+1} = \dot{\mathbf{x}}_n + A_1\ddot{\mathbf{x}}_n$

    $\mathbf{x}_{n+1} = \mathbf{x}_n + h\dot{\mathbf{x}}_n + B_1\ddot{\mathbf{x}}_n$

    $\ddot{\mathbf{x}}_{n+1} = 0$

4   Residual calculation:

    $\mathbf{r} = \mathbf{M}\ddot{\mathbf{x}}_{n+1} + \mathbf{f}_{nl} + \mathbf{f}_l - \mathbf{p}_{n+1}$

5   **while** *norm(**r**) > tol* **do**

        NR iteration (increment correction)

        $\mathbf{S}_{eff} = \mathbf{f}_{nl,\mathbf{x}} + B_2\mathbf{f}_{nl,\dot{\mathbf{x}}} + \mathbf{S}_{lin}$

        $\Delta\mathbf{x} = -\mathbf{S}_{eff}^{-1}\mathbf{r}$

        $\ddot{\mathbf{x}}_{n+1} + = A_2\Delta\mathbf{x}$

        $\dot{\mathbf{x}}_{n+1} + = B_2\Delta\mathbf{x}$

        $\mathbf{x}_{n+1} + = \Delta\mathbf{x}$

6 $\mathbf{r} = \mathbf{M}\ddot{\mathbf{x}}_{n+1} + \mathbf{f}_{nl} + \mathbf{f}_l - \mathbf{p}_{n+1}$

7   **if** *sensitivity* **then**

8   prediction

        $\mathbf{V} = \mathbf{V} + h\dot{\mathbf{V}} + B_1\ddot{\mathbf{V}}$

        $\dot{\mathbf{V}} = \dot{\mathbf{V}} + A_1\ddot{\mathbf{V}}$

        correction

        $\mathbf{S} = \mathbf{S}_{lin} + \mathbf{f}_{nl,\mathbf{x}} + B_2\mathbf{f}_{nl,\dot{\mathbf{x}}}$

        $\mathbf{S} = \beta h^2\mathbf{S}$

        $\ddot{\mathbf{V}} = -\mathbf{S}^{-1}\left[(\mathbf{C} + \mathbf{f}_{nl,\dot{\mathbf{x}}})\dot{\mathbf{V}} + (\mathbf{K} + \mathbf{f}_{nl,\mathbf{x}})\mathbf{V}\right]$

        $\mathbf{V} = \mathbf{V} + \beta h^2\ddot{\mathbf{V}}$

        $\dot{\mathbf{V}} = \dot{\mathbf{V}} + \gamma h\ddot{\mathbf{V}}$